# ANALYSIS OF RING FOCUS REFLECTORS

A THESIS SUBMITTED TO
THE GRADUATE SCHOOL OF NATURAL AND APPLIED SCIENCES
OF
MIDDLE EAST TECHNICAL UNIVERSITY

BY

HALIL ÖZDEMIR

IN PARTIAL FULFILLMENT OF THE REQUIREMENTS
FOR
THE DEGREE OF MASTER OF SCIENCE
IN
ELECTRICAL AND ELECTRONIC ENGINEERING

SEPTEMBER 2019

Approval of the thesis:

# ANALYSIS OF RING FOCUS REFLECTORS

submitted by **HALIL ÖZDEMIR** in partial fulfillment of the requirements for the degree of **Master of Science in Electrical and Electronic Engineering Department, Middle East Technical University** by,

Prof. Dr. Halil Kalıpçılar
Dean, Graduate School of **Natural and Applied Sciences**

Prof. Dr. İlkay Ulusoy
Head of Department, **Electrical and Electronic Eng.**

Prof. Dr. Sencer Koç
Supervisor, **Electrical and Electronic Eng., METU**

**Examining Committee Members:**

Prof. Dr. Özlem Aydın Çivi
Electrical and Electronic Eng., METU

Prof. Dr. Sencer Koç
Electrical and Electronic Eng., METU

Prof. Dr. Gülbin Dural
Electrical and Electronic Eng., METU

Assoc. Prof. Dr. Lale Alatan
Electrical and Electronic Eng., METU

Prof. Dr. Vakur Behçet Ertürk
Electrical and Electronic Eng., Bilkent University

Date: 11.09.2019

**I hereby declare that all information in this document has been obtained and presented in accordance with academic rules and ethical conduct. I also declare that, as required by these rules and conduct, I have fully cited and referenced all material and results that are not original to this work.**

Name, Surname: Halil Özdemir

Signature:

# ABSTRACT

## ANALYSIS OF RING FOCUS REFLECTORS

Özdemir, Halil
Master of Science, Electrical and Electronic Engineering
Supervisor: Prof. Dr. Sencer Koç

September 2019, 110 pages

Ring focus dual reflectors are the most modern forms of dual reflectors. They have distinctive geometries which eliminate the aperture blocking that results from the mechanical structure of sub-reflector. This characteristic of ring focus dual reflectors provides a more controllable reflector pattern as compared with classical dual reflectors. Also, the shape of the reflector pattern is different from the classical dual reflectors because of the fact that ring focus dual reflector geometries are different from the geometries of classical dual reflectors. The main aim of this thesis is investigation of the advantages and disadvantages which are coming with the usage of ring focus dual reflectors. In accordance with this aim, the analytical methods which provide the calculation of reflector patterns are examined and they are applied to classical and ring focus dual reflectors. The novelties that ring focus dual reflectors bring about are presented in the thesis and compatibility of the obtained results with the real world are discussed.

Keywords: Ring Focus (Displaced-Axis) Reflector, Current-Distribution Method, Aperture-Field Method

# ÖZ

## HALKA ODAKLI YANSITICILARIN ANALİZİ

Özdemir, Halil
Yüksek Lisans, Elektrik ve Elektronik Mühendisliği
Tez Danışmanı: Prof. Dr. Sencer Koç

Eylül 2019, 110 sayfa

Halka odaklı çift yansıtıcılar çift yansıtıcıların en modern şeklidirler. Kendilerine özgü geometrileri, alt yansıtıcının mekanik yapısından kaynaklanan açıklık engellemesini ortadan kaldırmaktadır. Halka odaklı çift yansıtıcıların bu özelliği klasik çift yansıtıcılara göre daha kontrol edilebilir bir yansıtıcı örüntüsünün ortaya çıkmasına sebep olmaktadır. Ayrıca, halka odaklı çift yansıtıcıların geometrileri klasik çift yansıtıcılardan farklı olduğu için yansıtıcı örüntüleri de klasik çift yansıtıcılardan farklı olmaktadır. Bu tezin temel amacı halka odaklı çift yansıtıcıların ortaya çıkarttıkları avantaj ve dezavantajların araştırılmasıdır. Bu amaç doğrultusunda yansıtıcı örüntülerinin hesaplanmasını sağlayan yöntemler incelenecek ve klasik ve halka odaklı çift yansıtıcılara uygulanacaktır. Halka odaklı çift yansıtıcıların getirdiği yenilikler tez içerisinde sunulacak ve ortaya çıkan sonuçların gerçek dünya ile uyumluluğu incelenecektir.

Anahtar Kelimeler: Halka Odaklı (Yer Değiştirmiş Eksenli) Yansıtıcı, Akım Dağılımı Yöntemi, Açıklık Alanı Yöntemi

To my lovely family…

## ACKNOWLEDGMENTS

I would like to thank to my supervisor Prof. Dr. Sencer Koç for his contributions to my thesis and for teaching me how to be a good person and scientist.

I also would like to thank the committee members those examined and contributed to this thesis: Prof. Dr. Özlem Aydın Çivi, Prof. Dr. Gülbin Dural, Assoc. Prof. Dr. Lale Alatan and Prof. Dr. Vakur Behçet Ertürk.

I am thankful to my employer TÜBİTAK BİLGEM İLTAREN and P110 Hardware Design Team for always supporting me throughout my master degree.

The last and greatest thanks are to my lovely family for always being with me.

# TABLE OF CONTENTS

CHAPTERS

APPENDICES

# LIST OF TABLES

TABLES

# LIST OF FIGURES

FIGURES

# LIST OF ABBREVIATIONS

| ABBREVIATIONS | |
|---|---|
| DORF | Double Offset Ring Focus |
| GO | Geometrical Optics |
| GTD | Geometrical Theory of Diffraction |
| PO | Physical Optics |
| SORF | Single Offset Ring Focus |

# CHAPTER 1

# INTRODUCTION

Reflector antennas are widely used in microwave applications that require high gain and narrow beamwidth. They have always been a popular subject in the microwave frequencies; therefore, there are many types of reflector antennas in the literature. The most common types of reflector antennas today are the antennas which have a parabolic reflector as the main reflector. The main reason of this choice is that parabolic reflectors are more efficient than other types of reflectors (plane reflector, corner reflector etc.). The primary goal of a parabolic reflector as the main reflector of a reflector antenna is that it converts the incoming rays to parallel rays leaving the reflector antenna. In addition to main reflector, modern reflector antennas usually have a minor reflector which is called as sub-reflector. These sub-reflectors provide good advantages to reflector antennas in terms of feed location. While parabolic reflectors are generated by rotating a parabolic curve about an axis by 360°, sub-reflectors arise from elliptic, hyperbolic or flat curve rotated 360° around the same axis depending on the type of the application.

Classical front-fed reflector geometry is the first and mostly known kind of parabolic reflector geometry. It has only main reflector; and thus, its geometry is quite simple. The history of parabolic reflectors is based on the defense of Syracuse in 287-212 B.C. In these years, a parabolic mirror was used by the famous Greek scientist Archimedes to burn the Roman ships during Punic War (Baars, 2007). The first realized front-fed reflector in radio frequencies is the dipole-fed parabolic reflector which was practiced by German physicist Heinrich Hertz in 1888 in order to show that radio waves behave as light rays for large wavelengths (Cichon & Wiesbeck, 1995). The feed antenna in a front-fed reflector is directed toward the main reflector. Therefore, aperture of feed antenna compulsorily causes the aperture blocking, that is some of the rays reflected by the main reflector returns back to the feed aperture, which is the main problem of many reflector geometries. Aperture blocking may change the antenna pattern by increasing side lobe levels and antenna beamwidth (Rudge & Adatia, 1978). To overcome this problem, offset geometry of front-fed reflector was presented (Sandler, 1960). Feed antenna is placed below the main reflector in offset reflectors. By this way, the offset geometries of reflectors do not have aperture blocking, but the radiation pattern of the reflectors is not symmetrical in this case. All offset reflectors have this disadvantage as well as the advantage of removing aperture blocking effect. Thus, importance of the symmetrical radiation pattern determines whether using an offset reflector instead of a classical reflector is reasonable or not.

Classical dual reflector geometries consist of two famous reflectors: Cassegrain and Gregorian reflectors. Laurent Cassegrain (Hannan, 1961) and James Gregory (Bucci, Pelosi, & Selleri, 1999) have designed reflecting telescope geometries both of which have aperture blocking like the classical front-fed reflector geometry. However, they have a nice advantage that the feed structures and low noise microwave blocks can be located at the back of the main reflector. This advantage is crucial to reduce the losses of the feed network and the noise temperature of receiving reflector antenna. In most applications, it is desired to remove (or minimize) the adverse effect of aperture blocking in reflector antennas. For this purpose, offset types of these reflectors are used. In these geometries, the main beam is not exposed to aperture blocking (Mizusawa, Urasaki, & Tanaka, 1977) , (Bergmann & Palma Pereira, 1998). The radiation patterns of these reflectors are not symmetrical as in the case of offset front-fed antennas.

In addition to mentioned reflector systems above, ring focus dual reflectors (displaced-axis dual reflectors) brought a new approach to dual reflector systems (Morgan, 1964). Unlike other reflectors, their foci create a ring as it is understood from their names. The most important feature of the ring focus dual reflectors is that ring focus dual reflectors have a feed offset which their design provides. Therefore, there is no aperture blocking which occurs from the physical structures of sub-reflectors in these reflectors. It is the main advantage of ring focus dual reflectors. By this advantage, ring focus dual reflectors were especially used to control the amplitude distribution on the aperture (Milligan & Popov, 1997). To improve the design of ring focus dual reflectors, Christophe Granet introduced his own procedure (Granet, 1999). In addition to control of the amplitude distribution on the aperture, ring focus dual reflectors were also used for forming the elliptic beam (Zhi-yong, 2010) and obtaining omnidirectional coverage (Bergmann & Moreira, 2005).

The ring focus reflectors are obtained by rotating a truncated parabolic main reflector and a displaced-axis hyperbolic or elliptic sub-reflector about a rotation axis by 360°, and this rotation axis has a vertical offset from the common foci of the main and sub-reflectors. Therefore, the coordinate of the focus in ring focus dual reflectors changes for each value of the rotation angle, and this rotated coordinate provides ring focus property for the reflector system. A sample geometry for a ring focus reflector is given in Figure 1.1 and Figure 1.2 as before rotation and after rotation, respectively.

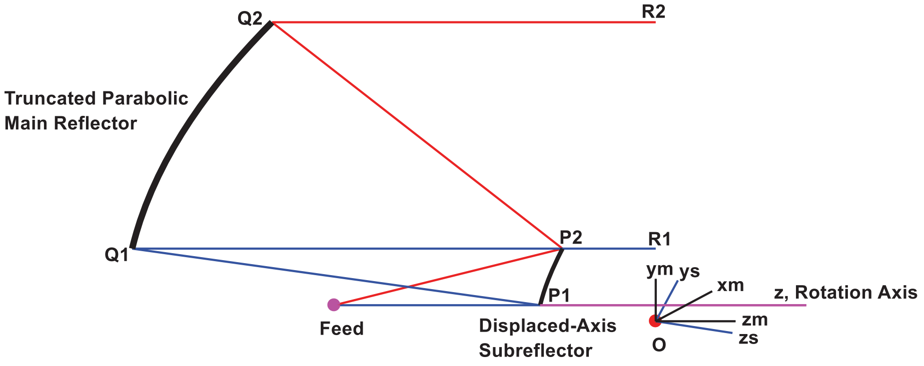

Figure 1.1. Before Rotation of the Truncated Parabolic Main Reflector and a Displaced-axis Hyperbolic or Elliptic Sub-reflector

In Figure 1.1, the curve between $Q_1$ and $Q_2$ represents the truncated parabolic main reflector and the curve between $P_1$ and $P_2$ represents the displaced-axis sub-reflector. The coordinate axes of the truncated parabolic main reflector and the displaced-axis sub-reflector are also given in the figure as $y_m$-$z_m$ and $y_s$-$z_s$, respectively. $O$ point represents the common focus of the truncated parabolic main reflector and displaced-axis sub-reflector. As shown in this figure, there is an offset between the rotation axis,$z$, and $O$ point. Thus, the focus takes the shape of ring after rotation. Also, sample propagations of two different rays are shown in this figure by blue and red lines.

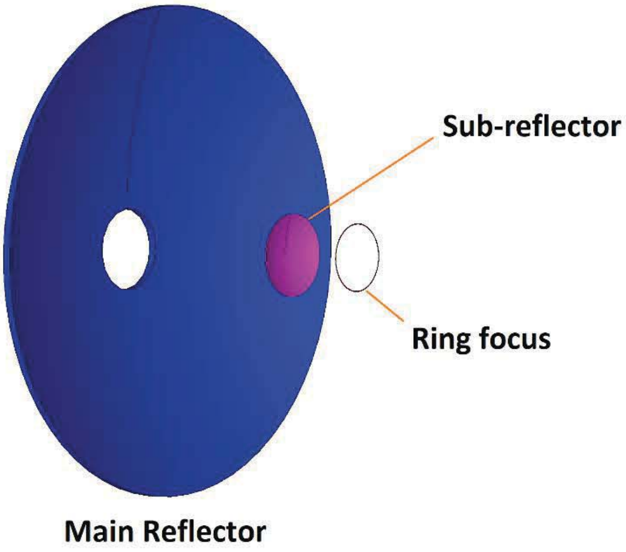

Figure 1.2. After Rotation of the Truncated Parabolic Main Reflector and a Displaced-axis Hyperbolic or Elliptic Sub-reflector

After rotation, blue, pink and black lines in Figure 1.2 show the truncated parabolic main reflector, displaced-axis sub-reflector and ring focus, respectively. As shown in this figure, the focus is annular and there is a hole in the main reflector.

Removing the effect of aperture blocking provides that ring focus dual reflectors have different antenna patterns from conventional dual reflectors. These differences may reveal good advantages in many types of microwave applications.

## 1.1. Motivation

As already mentioned, ring focus dual reflectors have distinctive physical geometries and so they produce different antenna patterns as compared to their classical forms.

The main purpose of this thesis is investigating the differences in antenna patterns for single and double offset ring focus geometries. After this examination, the benefits and disadvantages of ring focus dual reflectors are investigated. Therefore, the necessity of using ring focus systems is presented in accordance with the aim of the required application.

## 1.2. Outline

To realize the aim of the thesis, firstly, available techniques which can be applied in order to obtain the radiation patterns of reflector antennas are examined in Chapter 2. And then, the chosen analysis method in Chapter 2 are performed to the most basic form of reflector antennas (front-fed parabolic reflector) by using different feed structures in Section 3.2 and 3.3 to show the effect of feed structure on the reflector radiation pattern. This implementation creates a fundamental construction for the analysis of reflector antennas; and thus, the necessary changes could be easily carried out onto other type of reflector systems with the purpose of getting radiation patterns of them. Besides, the required feed pattern which provides uniform field distribution on the aperture plane of front-fed parabolic reflector is calculated in Chapter 3 and it is applied to written analysis code which is made for debugging purposes. After that, the fundamental construction is used in other type of reflectors in Chapters 4, 5 and 6 by only reflecting the incident field from the sub-reflector. Then, the advantages and disadvantages of ring focus dual reflectors are studied in Chapter 7 by comparison of the analyzed patterns of ring focus dual reflectors and classical dual reflectors. So, this chapter realizes the main goal of this thesis and shows the changes in the antenna patterns that arise when a ring focus reflector is used. Lastly, designs of ring focus reflectors are made in Chapter 8 and a conclusion chapter exists in Chapter 9.

# CHAPTER 2

## TECHNIQUES USED FOR ANALYSIS OF REFLECTOR ANTENNAS

Analysis of reflector antennas is an important subject for antenna designers. As mentioned in Chapter 1, reflector antennas are commonly used in microwave applications from commercial satellite communication to military radar systems. Nowadays, commercial electromagnetic simulation tools which can calculate the radiation characteristics of reflector antennas by using numerical methods are present. They give quite accurate simulation results, but the simulation time of them is very long especially if electrical size of the antenna is large. Besides, they require very expensive hardware cost if simulation time is wanted to shorten or huge mesh size is desired to solve. Due to these disadvantages of electromagnetic simulation tools, analysis tools which are based on some electromagnetic principles and use approximate methods are usually preferred to quickly obtain the radiation characteristics of reflector antennas. For this reason, analysis tools are important in terms of time saving for the design of reflector antennas. Moreover, analysis tools have a significant ability about the getting of the most suitable feed pattern which gives the required reflector pattern of the interested reflector. The reason of this ability is that analysis tools can use countless unreal feed patterns as feed of the reflector; and thus, they can obtain the most suitable feed pattern that provides the required reflector pattern. After obtaining the most suitable feed pattern, designers can focus only on its realization.

The most common methods used to calculate the radiation characteristics of reflector antennas are the Current-Distribution method and the Aperture-Field method. These methods are discussed in Section 2.1 and 2.2, respectively.

## 2.1. Current-Distribution Method

Current-Distribution method integrates the induced electric and magnetic current densities ($\bar{J}_s$ and $\bar{J}_{ms}$ respectively) over the reflector surface; and thus, this method is called the Current-Distribution method. To better understand this method, consider the generalized form of Maxwell's equations:

$$\begin{aligned}
&\bar{\nabla} \times \bar{E} = -j\omega\mu\bar{H} - \bar{J}_m \\
&\bar{\nabla} \times \bar{H} = j\omega\epsilon\bar{E} + \bar{J} \\
&\bar{\nabla} \cdot \bar{E} = \frac{1}{\epsilon}\rho \\
&\bar{\nabla} \cdot \bar{H} = \frac{1}{\mu}\rho_m
\end{aligned} \tag{2.1}$$

The solution of equation (2.1) can be obtained in terms of the scalar and vector potentials of the electric and magnetic type:

$$\begin{aligned}
\bar{E} &= -\bar{\nabla}\varphi - j\omega\bar{A} - \frac{1}{\epsilon}\bar{\nabla} \times \bar{A}_m \\
\bar{H} &= -\bar{\nabla}\varphi_m - j\omega\bar{A}_m + \frac{1}{\mu}\bar{\nabla} \times \bar{A}
\end{aligned} \tag{2.2}$$

The scalar and vector potentials satisfy the Lorentz conditions and Helmholtz wave equations:

$$\begin{aligned}
&\bar{\nabla} \cdot \bar{A} + j\omega\epsilon\mu\varphi = 0 \\
&\nabla^2\varphi + k^2\varphi = -\frac{\rho}{\epsilon} \\
&\nabla^2\bar{A} + k^2\bar{A} = -\mu\bar{J}
\end{aligned} \tag{2.3}$$

and;

$$\begin{aligned}
&\bar{\nabla} \cdot \bar{A}_m + j\omega\epsilon\mu\varphi_m = 0 \\
&\nabla^2\varphi_m + k^2\varphi_m = -\frac{\rho_m}{\mu} \\
&\nabla^2\bar{A}_m + k^2\bar{A}_m = -\epsilon\bar{J}_m
\end{aligned} \tag{2.4}$$

The solutions of the Helmholtz equations are given in terms of Green's function:

$$
\begin{aligned}
\varphi(\bar{r}) &= \int \frac{1}{\epsilon}\rho(\overline{r'})G(\bar{r}-\overline{r'})dV' \\
\bar{A}(\bar{r}) &= \int \mu\bar{J}(\overline{r'})G(\bar{r}-\overline{r'})dV'
\end{aligned}
\tag{2.5}
$$

and;

$$
\begin{aligned}
\varphi_m(\bar{r}) &= \int \frac{1}{\mu}\rho_m(\overline{r'})G(\bar{r}-\overline{r'})dV' \\
\bar{A}_m(\bar{r}) &= \int \epsilon\bar{J}_m(\overline{r'})G(\bar{r}-\overline{r'})dV'
\end{aligned}
\tag{2.6}
$$

By Lorentz conditions, the scalar potentials may be written in terms of the vector potentials, and an alternative expression for equation (2.2) is obtained:

$$
\begin{aligned}
\bar{E} &= \frac{1}{j\omega\epsilon\mu}[\overline{\nabla}(\overline{\nabla}\cdot\bar{A}) + k^2\bar{A}] - \frac{1}{\epsilon}\overline{\nabla}\times\bar{A}_m \\
\bar{H} &= \frac{1}{j\omega\epsilon\mu}[\overline{\nabla}(\overline{\nabla}\cdot\bar{A}_m) + k^2\bar{A}_m] + \frac{1}{\mu}\overline{\nabla}\times\bar{A}
\end{aligned}
\tag{2.7}
$$

Replacing $\bar{A}$ and $\bar{A}_m$ in terms of equations (2.5) and (2.6), the solutions in equation (2.7) may be expressed in terms of the current densities (Orfanidis, 1999):

$$
\begin{aligned}
\bar{E} &= \frac{1}{j\omega\epsilon}\int [\,\overline{\nabla}\,\overline{\nabla}\cdot(\bar{J}_s G)\; + k^2\bar{J}_s G - j\omega\epsilon\,\bar{J}_{ms}\times\overline{\nabla}G]\,dS' \\
\bar{H} &= \frac{1}{j\omega\mu}\int [\,\overline{\nabla}\,\overline{\nabla}\cdot(\bar{J}_{ms} G) + k^2\,\bar{J}_{ms} G + j\omega\mu\bar{J}_s\times\overline{\nabla}G]\,dS'
\end{aligned}
\tag{2.8}
$$

The parameters in equation (2.8) are described in Table 2.1.

Table 2.1. Parameter Description of Current-Distribution Method

| Symbol | Description |
|---|---|
| $\bar{E}$ | Electric field vector |
| $\bar{H}$ | Magnetic field vector |
| $G(\bar{r}-\overline{r'})$ | Scalar Green's function |
| $\overline{\nabla}$ | Del operator |

Equation (2.8) shows that the radiation characteristics of reflectors can be calculated easily if $\bar{J}_s$ and $\bar{J}_{ms}$ over the reflector surface are known. These current densities are induced by the incident field, and they can be approximated by using Physical Optics (PO) approximation as given in equation (2.9).

$$\bar{J}_s = \hat{n} \times (\bar{H}_i + \bar{H}_r) \cong 2\hat{n} \times \bar{H}_i = 2\hat{n} \times \bar{H}_r \qquad (2.9)$$

Here, $\bar{H}_i$ and $\bar{H}_r$ are the incident and reflected magnetic field vectors measured at the surface of the perfectly conducting reflector. If the value of either of them is known, $\bar{J}_s$ can be calculated by using equation (2.9). Besides, $\hat{n}$ represents the unit normal to the reflector surface.

The magnetic current density $\bar{J}_{ms}$ equals to zero on the reflector surface, because tangential electric fields are zero on perfect electric conductor. Thus, calculation of $\bar{J}_s$ is enough to obtain the radiation characteristics of reflectors in Current-Distribution method. Consequently, if incident magnetic field $\bar{H}_i$ is known, electric and magnetic field vectors in far-field can be found by using equations (2.8) and (2.9). And thus, radiation characteristics of reflectors are obtained.

Since PO is used in the Current-Distribution method, the basic assumptions used in PO approximation must also be true for the Current-Distribution method. These assumptions are summarized as below ( (Kishk, 2011) and (Balanis, Antenna Theory, 2005)).

- Radius of the reflector and size of the objects are large compared to the wavelength.
- The primary field from the feed can be treated as a plane wave.
- Reflector has a perfectly conducting surface.
- $\bar{J}_s$ is zero on the shadow side of the reflector.
- Direct radiation from the feed, edge effect of the reflector and aperture blockages resulted from the feed are neglected.

Also, since $\bar{J}_s$ and $\bar{J}_{ms}$ are the induced current densities, the assumptions made in surface equivalence theorem are also valid for Current-Distribution method. Besides, the tangential electric fields are zero on perfect electric conductor (Gibson, 2008).

### 2.2. Aperture-Field Method

Aperture-Field method is based on determining the aperture fields, $\bar{E}_a$ and $\bar{H}_a$, over the aperture plane, the plane on which the phase of the waves is constant, and using these fields to obtain the radiation pattern of the antennas. For this purpose, radiation vector of the feed antenna must be found. Radiation vector of an antenna is the Fourier transform of the electric field on the aperture plane of the antenna (Lo & Lee, 1993). A sample aperture is given in Figure 2.1.

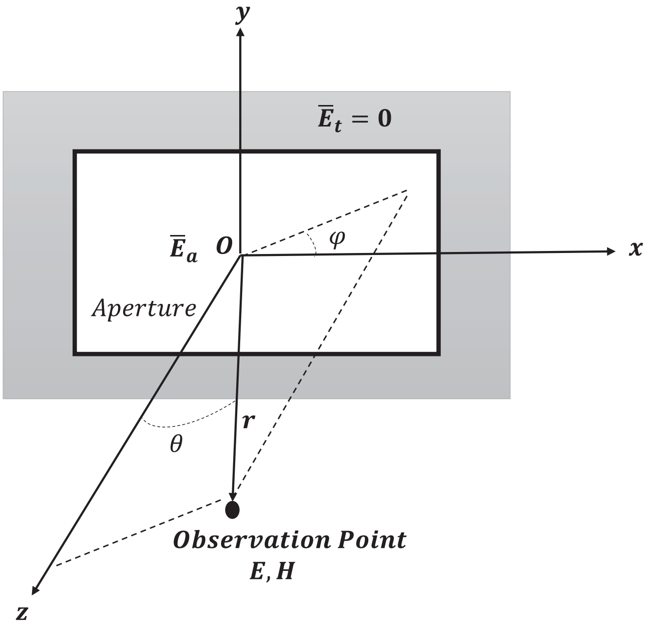

Figure 2.1. Radiation Fields from an Aperture

In Figure 2.1, $\bar{E}_a$ and $\bar{E}_t$ represent the tangential electric field on the aperture and the tangential electric field outside the aperture, respectively. It is assumed that the fields outside the aperture are zero. The radiation vector of the aperture, $\bar{f}(\theta, \varphi)$, can be calculated by equation (2.10).

$$\bar{f}(\theta,\varphi) = \int \bar{E}_a(x',y')\, e^{jk_x x' + jk_y y'} dx'dy' \tag{2.10}$$

After finding the radiation vector of the aperture, electric field components in far-field can be obtained by using equations (2.11) and (2.12) (Orfanidis, 1999).

$$E_\theta = jk\frac{e^{-jkr}}{2\pi r}\frac{1+\cos(\theta)}{2}[f_x \cos\varphi + f_y \sin\varphi] \tag{2.11}$$

$$E_\varphi = jk\frac{e^{-jkr}}{2\pi r}\frac{1+\cos(\theta)}{2}[f_y \cos\varphi - f_x \sin\varphi] \tag{2.12}$$

Descriptions of the parameters in equations (2.11) and (2.12) are listed in Table 2.2.

Table 2.2. Parameter Description of Aperture-Field Method

| Symbol | Description |
|---|---|
| $E_\theta$ | $\theta$ component of the electric field in far-field |
| $E_\varphi$ | $\varphi$ component of the electric field in far-field |
| $k$ | Wavenumber |
| $\frac{1+\cos(\theta)}{2}$ | Obliquity factor |
| $f_x$ | $x$ component of radiation vector |
| $f_y$ | $y$ component of radiation vector |

Differently from Current-Distribution method, Aperture-Field method involves Geometrical Optics (GO) approximation instead of PO approximation. Thus; the assumptions made in GO approximation are also required for Aperture-Field method. These assumptions can be summarized as below ( (Kishk, 2011) and (Balanis, Antenna Theory, 2005)).

- Radius of the reflector and size of the objects are large compared to the wavelength.

- Reflector surface is smooth enough so that it can be approximated by a plane about any reflection point on the surface.
- The wave radiated from the feed can be treated as a plane wave.
- Reflector has a perfectly conducting surface.
- Direct radiation from the feed, edge effect of the reflector and aperture blockages resulted from the feed are neglected.

When contrasting with Current-Distribution method, equivalent sources which are used to determine the radiation characteristics of reflectors are the fields on the aperture plane in Aperture-Field method instead of the induced current densities on the reflector surface. Both methods can be used to develop an analysis tool that can be used to investigate the radiation characteristics of reflectors. Due to construction of the equivalence theorem, both methods give accurate results only in the region of interest (front side of the reflector). Also, edge diffraction of reflector is not taken into account in either method; therefore, errors will occur in antenna pattern especially as we move away from the boresight of the antenna. A brief explanation about GTD can be found in Appendix C.

The main advantage of Aperture-Field method is that integration over the aperture plane has similar ease for any feed pattern or feed position. But, integration over reflector surface, which is required in Current-Distribution method, is different for each reflector type and this integration must be recalculated for each reflector type. This necessity causes additional process burden for the computation. Thus, Aperture-Field method is chosen to analyze the reflector antennas in this thesis.

# CHAPTER 3

# FRONT-FED PARABOLIC REFLECTOR

As mentioned in Chapter 2, Aperture-Field method is preferred in this thesis to analyze the radiation characteristics of reflector antennas. Aperture-Field method requires determination of aperture fields and replacing them in equation (2.11) and (2.12) to calculate the radiation characteristics of reflector antennas. Equation (2.11) and (2.12) indicate that radiated fields from an aperture can be obtained if its radiation vector is known. Therefore, finding $f_x$ and $f_y$ is enough to calculate the radiation characteristics of reflector antennas.

Front-Fed Parabolic Reflector is the first type of the reflectors investigated in this thesis. The reason of this is that Front-Fed Parabolic Reflector includes a fundamental structure for the analysis of reflector antennas. After verifying this fundamental structure, the necessary changes can be easily carried out for other reflector types. The geometry of front-fed parabolic reflector is shown in Figure 3.1.

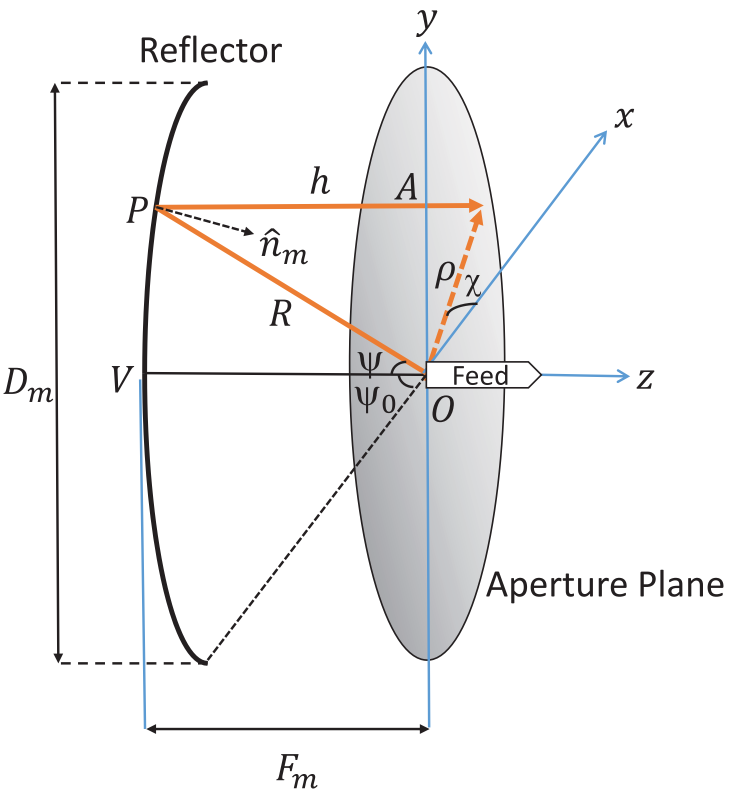

Figure 3.1. Geometry of Front-Fed Parabolic Reflector

In Figure 3.1, $O$ point shows the focus of the reflector and the feed is placed at this point. $D_m$ and $F_m$ represent the diameter and the focal length of the reflector, respectively. The rays leaving the feed are reflected from the parabolic reflector; and then, they propagate in $+z$ direction parallel to the $z$ axis. $R$ represents the path between the feed and the reflection point on the reflector, and $h$ represents the path between the reflection point on the reflector and the aperture plane of the reflector. The plane on which the phases of all the rays are constant is called an aperture plane. We will take the aperture plane as the plane that passes through the focus, $O$. On the aperture plane, all possible values of $R$ and all corresponding values of $h$ must give the same total length for each possible angle of $\psi$. $\rho$ is the distance of the ray in the aperture plane to $O$. Also, $\psi_0$is the subtended angle of the reflector and $\hat{n}_m$is the surface normal of the reflector.

To obtain the field reflected from the reflector, the field incident from the feed antenna must be known firstly. If the reflector geometry does not have a sub-reflector as in Figure 3.2, the field incident from the feed antenna are applied to main reflector directly by using equation (3.1) (Mahajan, 2014).

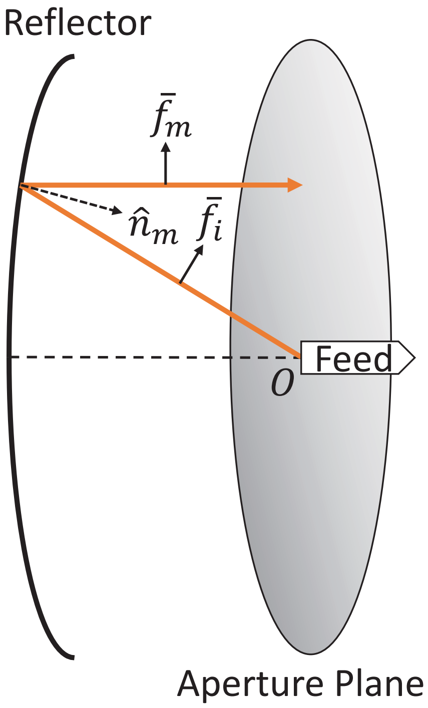

Figure 3.2. Obtaining Field Reflected from the Reflector in a Single Reflector System

In Figure 3.2, $\bar{f}_i$ is the field incident from the feed and $\bar{f}_m$ is the field reflected from the reflector. The relation between $\bar{f}_i$ and $\bar{f}_m$ is given in equation (3.1).

$$\bar{f}_m = -\bar{f}_i + 2\hat{n}_m(\hat{n}_m \cdot \bar{f}_i) \tag{3.1}$$

The derivation of equation (3.1) is given in Appendix E and descriptions of the parameters in equation (3.1) are listed in Table 3.1.

Table 3.1. List of Symbols (Field Reflected from the Main Reflector)

| Symbol | Description |
|---|---|
| $\bar{f}_i$ | Field incident from the feed antenna |
| $\bar{f}_m$ | Field reflected from the main reflector |
| $\hat{n}_m$ | Normal vector of main reflector surface |

If the reflector geometry has a sub-reflector as in Figure 3.3, the field reflected from the sub-reflector must be found by using equation (3.2).

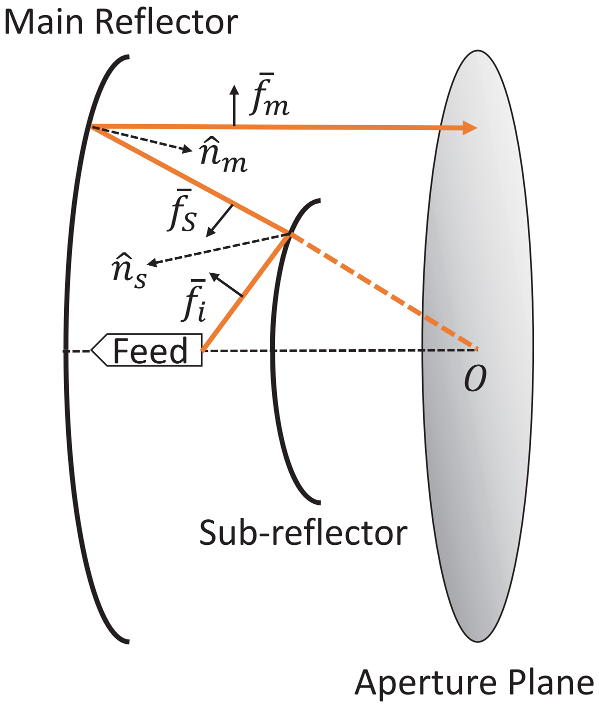

Figure 3.3. Obtaining Field Reflected from the Main Reflector in a Dual Reflector System

$$\bar{f}_s = -\bar{f}_i + 2\hat{n}_s(\hat{n}_s \cdot \bar{f}_i) \qquad (3.2)$$

Descriptions of the parameters in equation (3.2) are listed in Table 3.2.

Table 3.2. List of Symbols (Field Reflected from the Sub-reflector)

| Symbol | Description |
|---|---|
| $\bar{f}_i$ | Field incident from the feed antenna |
| $\bar{f}_s$ | Field reflected from the sub-reflector |
| $\hat{n}_s$ | Normal vector of sub-reflector surface |

After finding $\bar{f}_s$ from equation (3.2), $\bar{f}_s$ must be placed in equation (3.3) to calculate the field reflected from the main reflector.

$$\bar{f}_m = -\bar{f}_s + 2\hat{n}_m(\hat{n}_m \cdot \bar{f}_s) \tag{3.3}$$

As mentioned above, equation (3.1) is enough to obtain $\bar{f}_m$ in front-fed parabolic reflector. Otherwise, if the reflector geometry has a sub-reflector, the field reflected from the sub-reflector, which is found in equation (3.2), is applied to main reflector as in equation (3.3). With the calculation of $\bar{f}_m$, the final process is completed to obtain the radiation characteristics of front-fed parabolic reflector. After obtaining $\bar{f}_m$, the electric field on the aperture plane of the reflector can be calculated by equation (3.4).

$$\bar{E}_a = \frac{e^{-jkR}}{R}\bar{f}_m \tag{3.4}$$

where $\bar{E}_a$ is the electric field on the aperture plane of the reflector and it must be put into equation (2.10) to calculate the radiation vector of the reflector.

The reflector in Figure 3.1 is a parabolic reflector and the feed structure is placed at the focus of it. The equation of parabolic reflector is given in equation (3.5) (Sharma, Rao, & Shafai, 2013).

$$\rho^2 = 4F_m z \tag{3.5}$$

In equation (3.5), $\rho$ and $z$ represent the two axes of cylindrical coordinate system. $F_m$ is the focal length of the parabolic reflector as indicated in Figure 3.1. Normal vector of parabolic reflector ($\hat{n}_m$) can be obtained by taking the gradient of equation (3.5).

By rewriting equation (3.5):

$$\rho^2 - 4F_m z = 0 \tag{3.6}$$

By taking the gradient of equation (3.6):

$$\hat{n}_m = \frac{-\nabla(\rho^2 - 4F_m z)}{\|\nabla(\rho^2 - 4F_m z)\|} \tag{3.7}$$

By using $\bar{\rho} = x\hat{x} + y\hat{y}$ and $\rho^2 = x^2 + y^2$:

$$\hat{n}_m = \frac{-1}{\sqrt{\frac{(x^2 + y^2)}{4F_m^2} + 1}} \left( \frac{x}{2F_m}\hat{x} + \frac{y}{2F_m}\hat{y} - \hat{z} \right) \tag{3.8}$$

Only $\bar{f_i}$ remains as an unknown in equation (3.1) after finding $\hat{n}_m$ . The value of $\bar{f_i}$ depends on the feed itself and its expressions for different feed structures are given in Section 3.1 to 3.3.

$R$ and $h$ parameters in Figure 3.1 represent the path lengths of the rays $OP$ and $PA$, respectively. Any ray that emanates from the focal point $O$ is reflected in a direction parallel to the $z$ axis by the parabolic reflector and arrive at a point $A$ on the surface. The total path length traversed by any such ray is a constant that is independent of the departure angle and equals to $2F_m$ for all values of $\psi$ .

$$R + h = 2F_m \tag{3.9}$$

By using the geometric relations in Figure 3.1;

$$h = R\cos\psi \tag{3.10}$$

and then;

$$R + R\cos\psi = 2F_m \tag{3.11}$$

Thus, the expression of $R$ is obtained in terms of $F_m$ and $\psi$.

$$R = \frac{2F_m}{1 + \cos\psi} = \frac{F_m}{\cos^2\left(\frac{\psi}{2}\right)} \tag{3.12}$$

Also, by using the geometric relations in Figure 3.1 again:

$$\rho = R \sin\psi \tag{3.13}$$

Finally, we get the expression of $\rho$ in terms of $F_m$ and $\psi$.

$$\rho = 2F_m \frac{\sin\psi}{1 + \cos\psi} = 2F_m \tan\frac{\psi}{2} \tag{3.14}$$

Put $\rho = D_m/2$ and $\psi = \psi_0$ into equation (3.14);

$$\psi_0 = 2\,\mathrm{atan}\left(\frac{D_m}{4F_m}\right) \tag{3.15}$$

$\psi_0$ is called the 'subtended angle' of the parabolic reflector.

### 3.1. Debugging of Analysis Tool

In this section, a special feed that creates a uniform field over the aperture of the front-fed parabolic reflector is calculated and it is used to debug the coded analysis tool in this thesis. This analysis tool calculates the radiation pattern of the reflectors by using Aperture-Field method in Matlab environment. The input of this tool is the field incident from the feed and the tool gives radiation pattern of the chosen reflector as output. The required feed pattern for uniform aperture field of front-fed parabolic reflector can be calculated by using equations (3.1) and (3.2). The calculated feed pattern is then used as the feed of the front-fed parabolic reflector, and amplitude and phase distributions of the fields over the aperture plane are investigated. If the field over aperture plane is uniform as expected, it shows that the ray tracing step of the analysis tool is correctly implemented. This verification of the tool is important since front-fed parabolic reflector makes up a basis for all the geometries which have dual reflectors. The only difference between front-fed parabolic reflector and the structures with dual reflectors is that structures with dual reflectors use the field reflected from the sub-reflector instead of the field resulted from the feed directly. All remaining computation steps for the front-fed parabolic reflector and for the structures with dual reflectors are the same.

As discussed previously in this chapter, incident field can be used in equation (3.1) directly for the front-fed parabolic reflectors. Thus;

$$\bar{f}_m = -\bar{f}_i + 2\hat{n}_m(\hat{n}_m \cdot \bar{f}_i) \tag{3.16}$$

Let, $K(\psi, \chi)$ be defined as the scalar in equation (3.17). $\psi$ and $\chi$ are shown in Figure 3.1.

$$K(\psi, \chi) = (\hat{n}_m \cdot \bar{f}_i) \tag{3.17}$$

The $x$,$y$ and $z$ components of $\bar{f}_m$ must be equal to values in equation (3.18) in order to get a $y$-polarized uniform field over the aperture plane.

$$\begin{aligned} \bar{f}_m &= f_{mx}\hat{x} + f_{my}\hat{y} + f_{mz}\hat{z} \\ f_{mx} &= 2K(\psi,\chi)n_{mx} - f_{ix} = 0 \\ f_{my} &= 2K(\psi,\chi)n_{my} - f_{iy} = \frac{R}{e^{-jkR}} \\ f_{mz} &= 2K(\psi,\chi)n_{mz} - f_{iz} = 0 \end{aligned} \tag{3.18}$$

Solving equation (3.18) for the components of $\bar{f}_i$ yields;

$$\begin{bmatrix} f_{ix} \\ f_{iy} \\ f_{iz} \end{bmatrix} = \begin{bmatrix} -\frac{R}{e^{-jkR}}\sin(2\chi)\frac{\cos(\psi)-1}{2} \\ -\frac{R}{e^{-jkR}}\big((\cos(\psi)-1)\sin^2(\chi)+1\big) \\ -\frac{R}{e^{-jkR}}2\sin(\chi)\sin(\psi/2)\cos(\psi/2) \end{bmatrix} \tag{3.19}$$

The steps from equation (3.18) to equation (3.19) are given in Appendix D.

where $n_{mx}$, $n_{my}$ and $n_{mz}$ are the $x$,$y$ and $z$ components of $\hat{n}_m$. Their values in terms of $\psi$ and $\chi$ are given in equation (3.20).

$$\begin{aligned} n_{mx} &= -\cos(\chi)\sin(\psi/2) \\ n_{my} &= -\sin(\chi)\sin(\psi/2) \\ n_{mz} &= \cos(\psi/2) \end{aligned} \tag{3.20}$$

For a front-fed parabolic reflector that is fed with a primary feed pattern whose components $f_{ix}$, $f_{iy}$ and $f_{iz}$ are as given in equation (3.19), the field on the aperture plane of the reflector becomes uniform. To debug the analysis tool developed in this thesis, the field components found in equation (3.19) are used as the feed of the front-fed parabolic reflector and the amplitude and phase distributions on the aperture plane are investigated.

The amplitude distribution of the field on the aperture plane is shown in Figure 3.4.

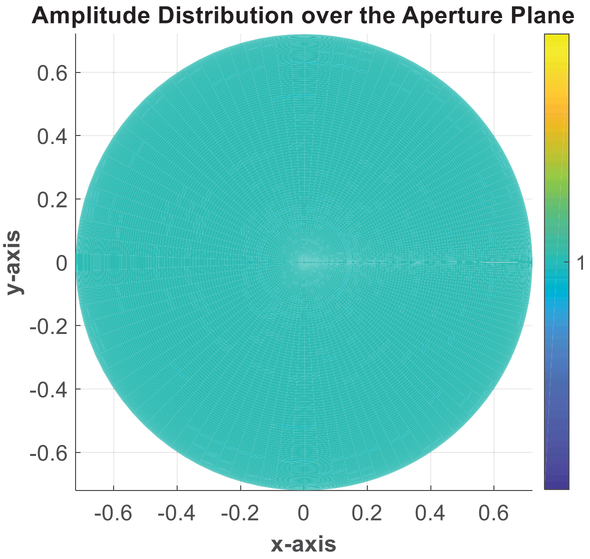

Figure 3.4. $|E_y|$ over the Aperture Plane

The phase distribution of the field on the aperture plane is given in Figure 3.5.

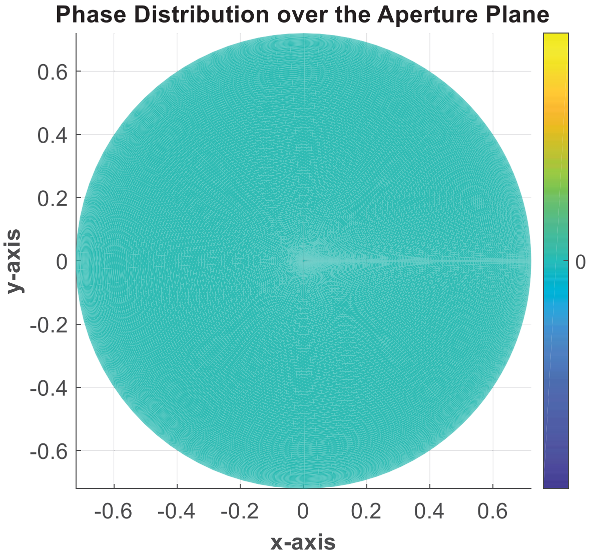

Figure 3.5. Phase of $E_y$ over the Aperture Plane

When Figure 3.4 and Figure 3.5 are examined, it can be seen that the amplitude and phase of the field on aperture plane is constant. In other words, it is a uniform field. This result validates the implementation of the analysis tool, at least for the main reflector.

## 3.2. Open Ended Waveguide Feed

In this section, the field incident from an open ended waveguide is found; and thus, the radiation characteristic of the front-fed parabolic reflector whose feed is an open ended waveguide is calculated by using equations from (3.2) to (3.15) as well as equation (2.11) and (2.12).

Firstly, consider an open ended waveguide geometry like in Figure 3.6.

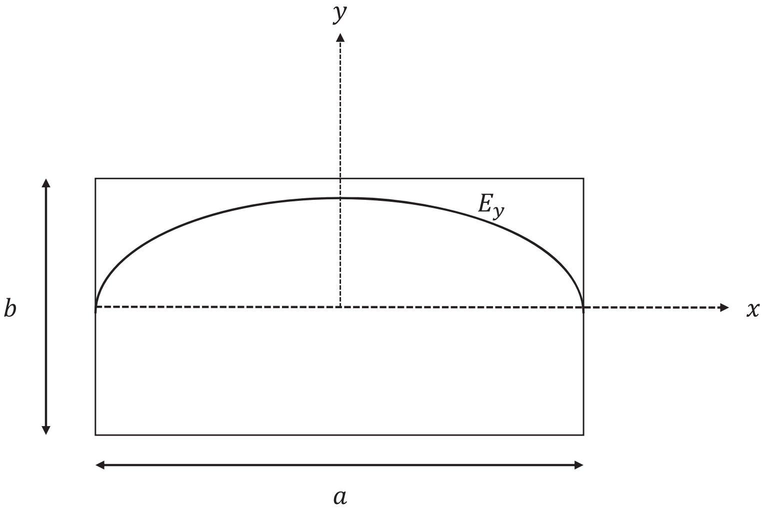

Figure 3.6. Geometry of an Open Ended Waveguide

The electric field in the open ended waveguide operating in TE10 mode can be expressed as:

$$E_y(x) = E_0 \cos\left(\frac{\pi x}{a}\right) \tag{3.21}$$

Besides, the field incident from the open ended waveguide, $f_{yw}(\theta, \varphi)$, can be calculated by obtaining the Fourier transform of the electric field over the aperture plane (Lo & Lee, 1993).

$$f_{yw}(\theta, \varphi) = \int_{-a/2}^{a/2} \int_{-b/2}^{b/2} E_y(x) e^{jk_x x + jk_y y} d_y d_x \tag{3.22}$$

By putting the value of $E_y(x)$ in equation (3.21) into equation (3.22):

$$\begin{aligned} f_{yw}(\theta, \varphi) &= E_0 \int_{-\frac{a}{2}}^{\frac{a}{2}} \int_{-\frac{b}{2}}^{\frac{b}{2}} \cos\left(\frac{\pi x}{a}\right) e^{jk_x x + jk_y y} d_y d_x \\ &= E_0 \int_{-a/2}^{a/2} \cos\left(\frac{\pi x}{a}\right) e^{jk_x x} d_x \, . \int_{-b/2}^{b/2} e^{jk_y y} d_y \end{aligned} \tag{3.23}$$

Equation (3.23) can be solved analytically:

$$
\begin{aligned}
f_{yw}(\theta,\varphi) &= E_0 \frac{2ab}{\pi} \frac{\cos(\pi v_x)}{1-4v_x^2} \frac{\sin(\pi v_y)}{\pi v_y} \\
v_x &= \frac{a}{\lambda}\sin(\theta)\cos(\varphi), v_y = \frac{b}{\lambda}\sin(\theta)\sin(\varphi)
\end{aligned}
\tag{3.24}
$$

Lastly, putting the result of $f_{yw}(\theta,\varphi)$ into equations (3.1) and (3.2) provides us to know the field reflected from the front-fed parabolic reflector whose feed is the open ended waveguide. The reflected field calculated in there is placed into equations (2.11) and (2.12) to get the radiation characteristics of the overall system.

The calculated radiation pattern of the front-fed parabolic reflector which has the open ended waveguide as the feed is shown in Figure 3.7, Figure 3.8 and Figure 3.9, and the chosen parameter values of the front-fed parabolic reflector and the open ended waveguide are listed in Table 3.3.

Table 3.3. Chosen Parameters of Front-Fed Parabolic Reflector and Open Ended Waveguide

| Parameter Name | Parameter Value |
|---|---|
| Main reflector diameter ($D_m$) | 4 m |
| Main reflector focal length ($F_m$) | 2.5 m |
| Long length of the waveguide ($a$) | 0.072 m |
| Short length of the waveguide ($b$) | 0.034 m |
| Operating Frequency ($f$) | 3.8 GHz |

The calculated E-plane ($\varphi = 0°$) radiation pattern of the front-fed parabolic reflector which has the open ended waveguide as the feed is shown in Figure 3.7.

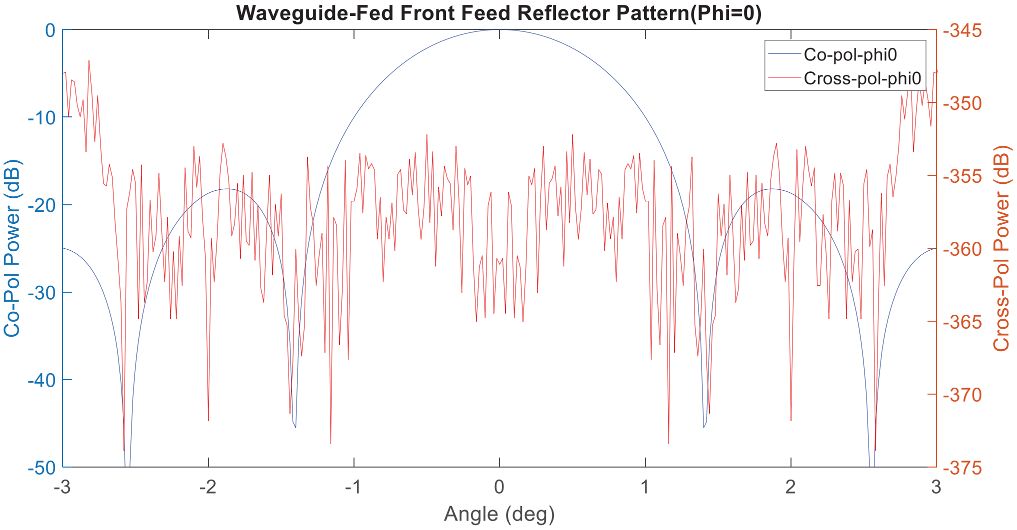

Figure 3.7. Open Ended Waveguide-Fed Front-Fed Reflector Pattern ($\varphi = 0°$)

The calculated radiation pattern of the front-fed parabolic reflector which has the open ended waveguide as the feed is shown in Figure 3.8 for ($\varphi = 45°$).

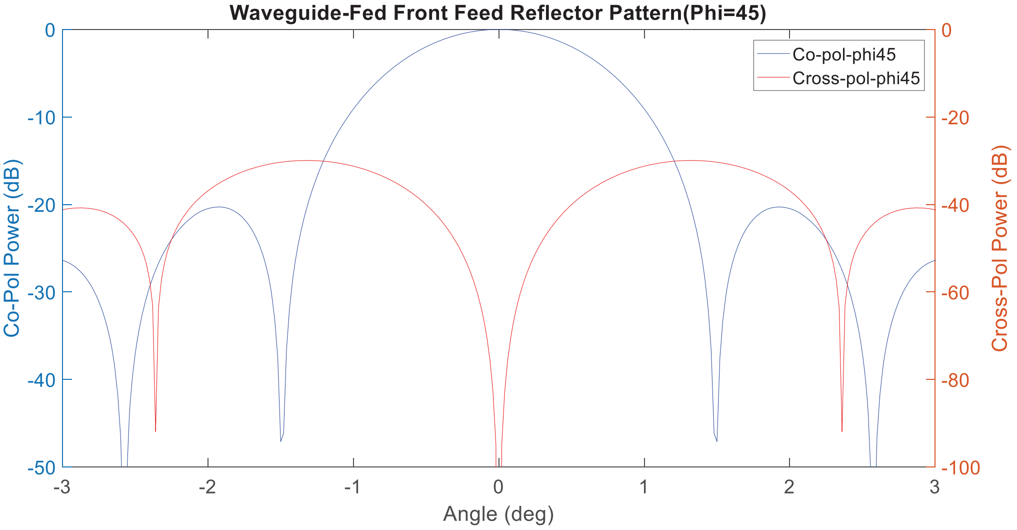

Figure 3.8. Open Ended Waveguide-Fed Front-Fed Reflector Pattern ($\varphi = 45°$)

The calculated H-plane ($\varphi = 90°$) radiation pattern of the front-fed parabolic reflector which has the open ended waveguide as the feed is shown in Figure 3.9.

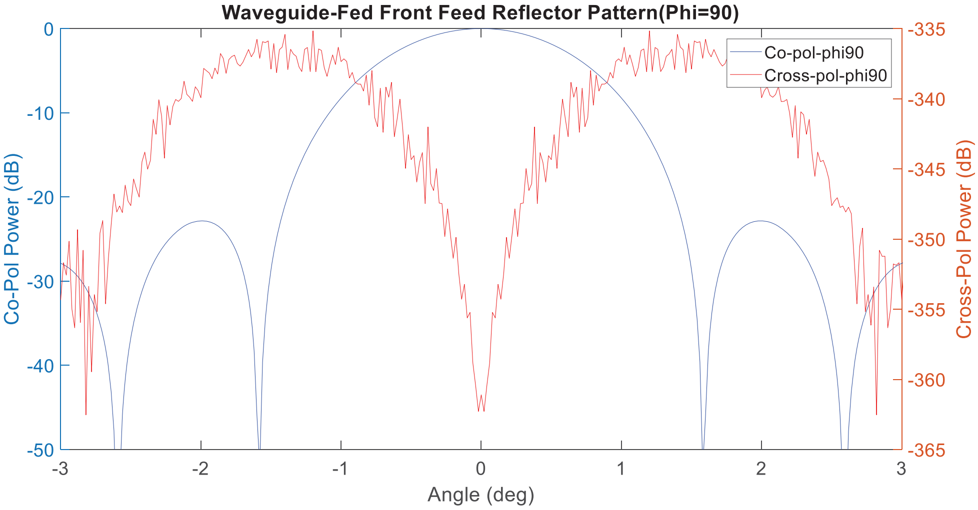

Figure 3.9. Open Ended Waveguide-Fed Front-Fed Reflector Pattern ($\varphi = 90°$)

Also, the calculated radiation pattern of the front-fed parabolic reflector which has the open ended waveguide as the feed is compared with the result of Orfanidis (Orfanidis, 1999). The comparison result is given in Figure 3.10.

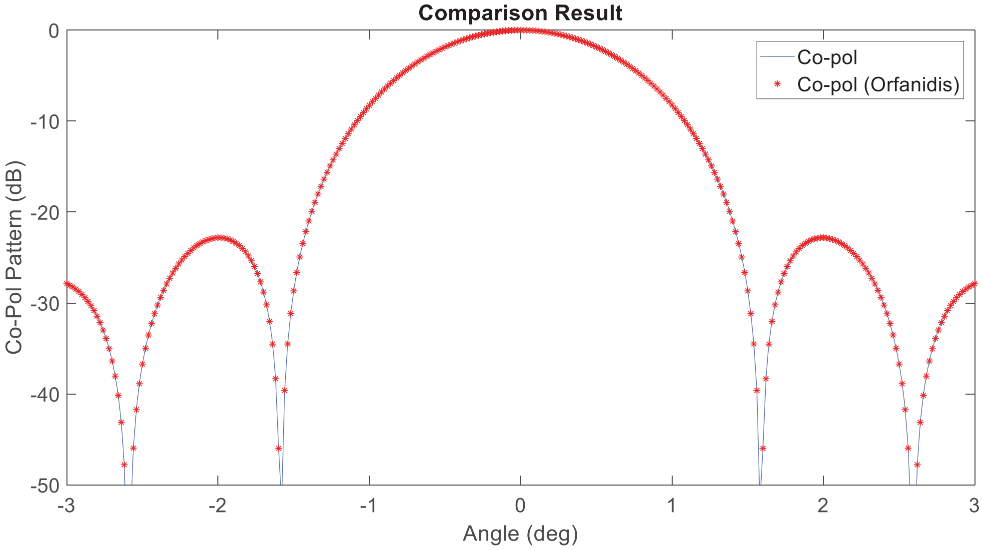

Figure 3.10. Comparison Result of Open Ended Waveguide-Fed Patterns

As shown in Figure 3.10, the calculated radiation pattern of the open ended waveguide-fed reflector is exactly the same with the result of Orfanidis.

The calculated radiation patterns of the open ended waveguide-fed and horn-fed reflectors are compared with each other in section 3.4 in order to show the effect of the used feed on the reflector pattern.

### 3.3. Horn Feed

In this section, the field incident from the horn antenna is derived; and thus, the radiation characteristic of the front-fed parabolic reflector whose feed is a horn antenna is calculated by using equations from (3.1) to (3.15) as well as equation (2.11) and (2.12).

Consider a horn geometry and its cross sections like in Figure 3.11 and Figure 3.12.

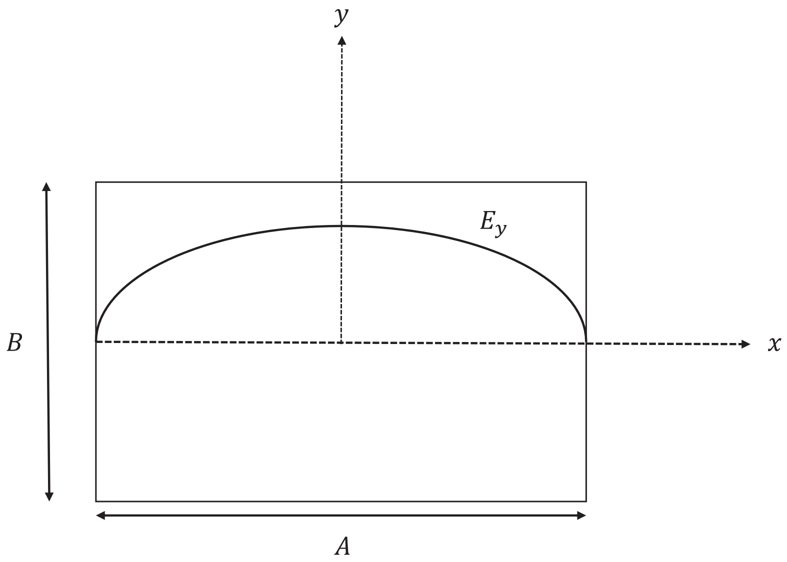

Figure 3.11. Geometry of Horn Aperture

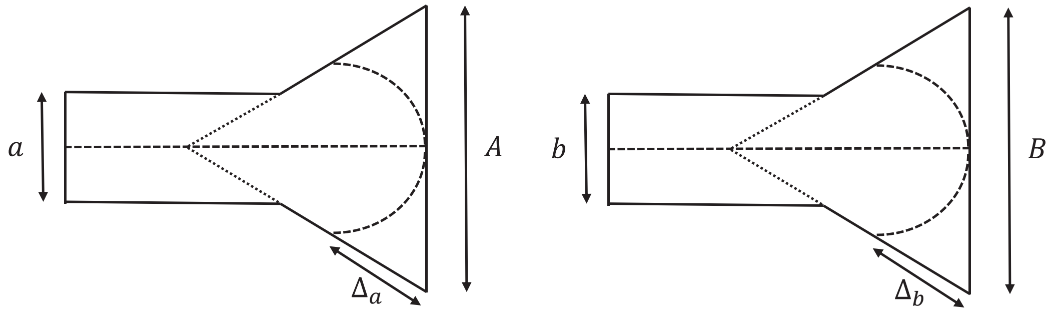

Figure 3.12. Cross Sections of Horn Structure

The electric field in the horn structure can be expressed as:

$$E_y(x,y) = E_0 \cos\left(\frac{\pi x}{a}\right) e^{-jk\Delta_a - jk\Delta_b} \tag{3.25}$$

In equation (3.25), $\Delta_a$ and $\Delta_b$ represent the delays of electric field resulted from the extra path lengths in the horn structure unlike open ended waveguide.

Besides, the field incident from the horn antenna, $f_{yh}(\theta,\varphi)$, can be calculated by obtaining the Fourier transform of the electric field over the aperture plane as mention in Section 3.2.

$$f_{yh}(\theta,\varphi) = E_0 \int_{-A/2}^{A/2} \int_{-B/2}^{B/2} \cos\left(\frac{\pi x}{a}\right) e^{-jk\Delta_a - jk\Delta_b} e^{jk_x x + jk_y y} \mathrm{d}_y \mathrm{d}_x \tag{3.26}$$

For calculation of the integrals in equation (3.26) and for other integrals in this thesis, various numerical integration methods such as Trapezoidal rule and Gauss-Legendre Quadrature method (Davis & Rabinowitz, 1984) can be used. The detailed expressions about these methods are given in Appendix A and Appendix B, respectively.

Putting the result of $f_{yh}(\theta,\varphi)$ into equations (3.1) and (3.2) gives the field incident from the front-fed parabolic reflector whose feed is the horn antenna. The reflected field calculated in there is placed in equations (2.11) and (2.12) to get the radiation characteristics of the overall system.

The calculated radiation fields of the front-fed parabolic reflector which has the horn antenna as the feed are given in Figure 3.13, Figure 3.14 and Figure 3.15, and the chosen parameter values are listed in Table 3.4.

Table 3.4. Chosen Parameters of Front-Fed Parabolic Reflector and Horn Antenna

| Parameter Name | Parameter Value |
|---|---|
| Main reflector diameter ($D_m$) | 4 m |
| Main reflector focal length ($F_m$) | 2.5 m |
| Long length of the horn aperture ($A$) | 0.144 m |
| Short length of the horn aperture ($B$) | 0.068 m |
| Operating Frequency ($f$) | 3.8 GHz |
| $\Delta_a$ | 0.03 m |
| $\Delta_b$ | 0.02 m |

The calculated E-plane ($\varphi = 0°$) radiation pattern of the front-fed parabolic reflector which has the horn antenna as the feed is shown in Figure 3.13.

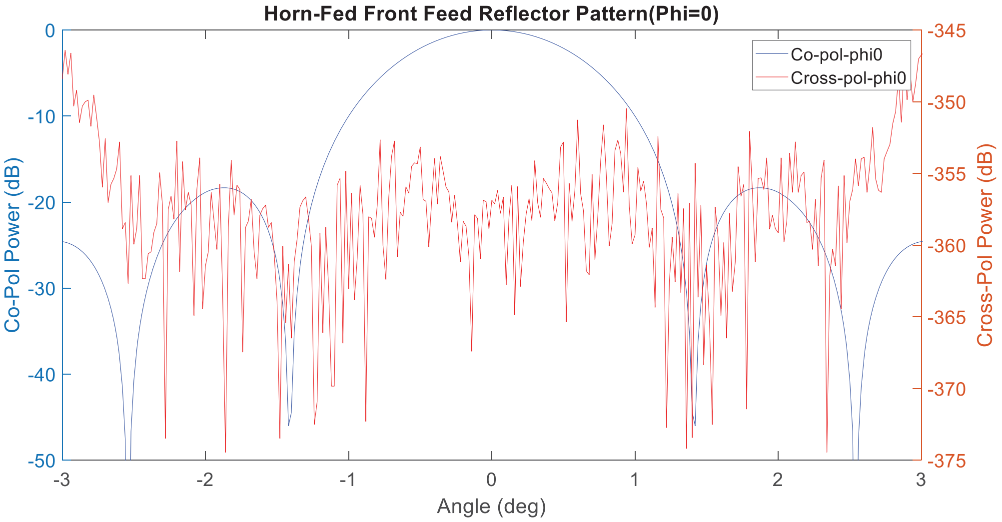

Figure 3.13. Horn-Fed Front-Fed Reflector Pattern ($\varphi = 0°$)

The calculated radiation pattern of the front-fed parabolic reflector which has the horn antenna as the feed is shown in Figure 3.14 for ($\varphi = 45°$).

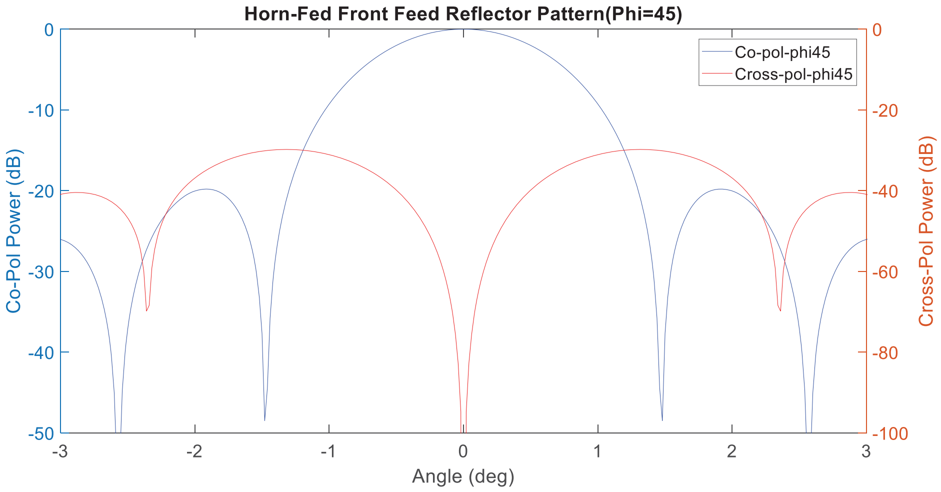

Figure 3.14. Horn-Fed Front-Fed Reflector Pattern ($\varphi = 45°$)

The calculated H-plane ($\varphi = 90°$) radiation pattern of the front-fed parabolic reflector which has the horn antenna as the feed is shown in Figure 3.15.

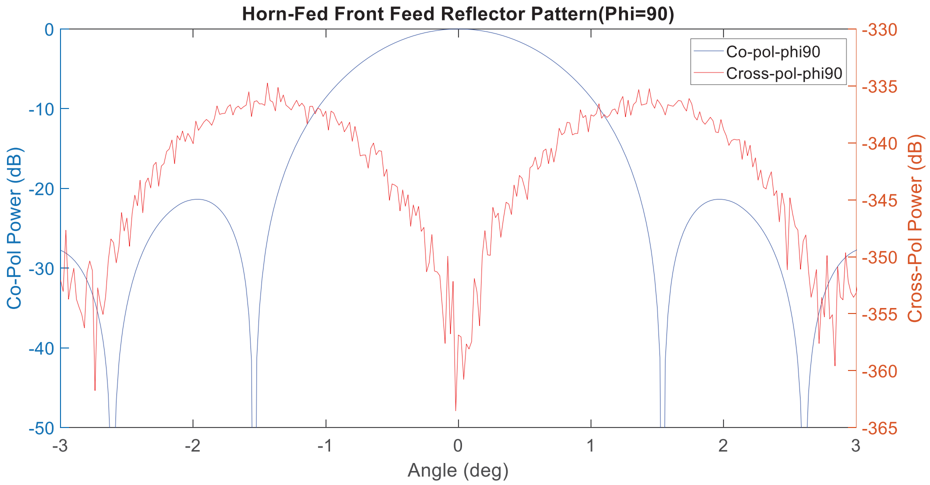

Figure 3.15. Horn-Fed Front-Fed Reflector Pattern ($\varphi = 90°$)

Also, the calculated radiation pattern of the front-fed parabolic reflector which has the horn as the feed is compared with the result of Orfanidis (Orfanidis, 1999). The comparison result is given in Figure 3.16.

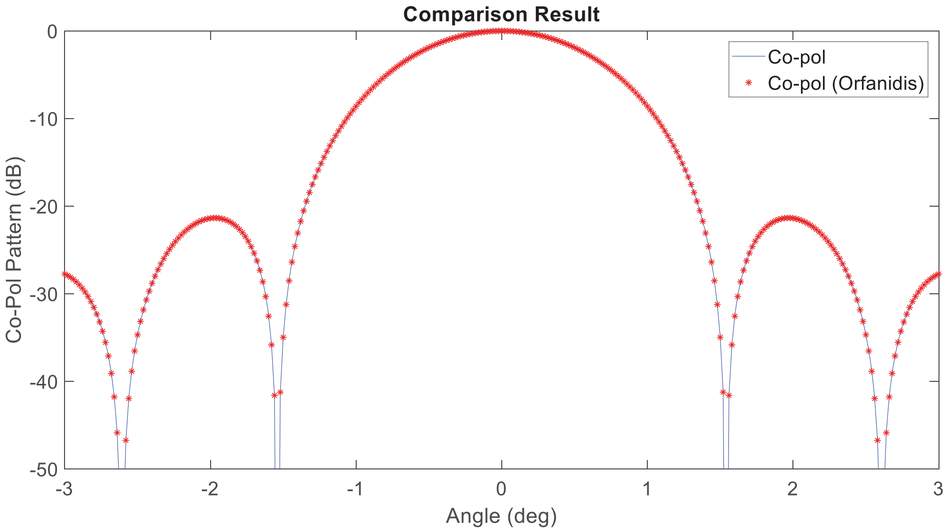

Figure 3.16. Comparison Result of Horn-Fed Patterns

As shown in Figure 3.16, the calculated radiation pattern of the horn-fed reflector is exactly the same with the result of Orfanidis.

The calculated radiation pattern of the open ended waveguide-fed and horn-fed reflectors are compared with each other in section 3.4 in order to show the effect of the used feed on the reflector pattern.

### 3.4. Comparison of Open Ended Waveguide and Horn Feed

In this section, the patterns of the same front-fed parabolic reflector which is fed with different feed structures are compared with each other. To achieve it, the results found in Sections 3.2 and 3.3 are used. The compared result is given in Figure 3.17.

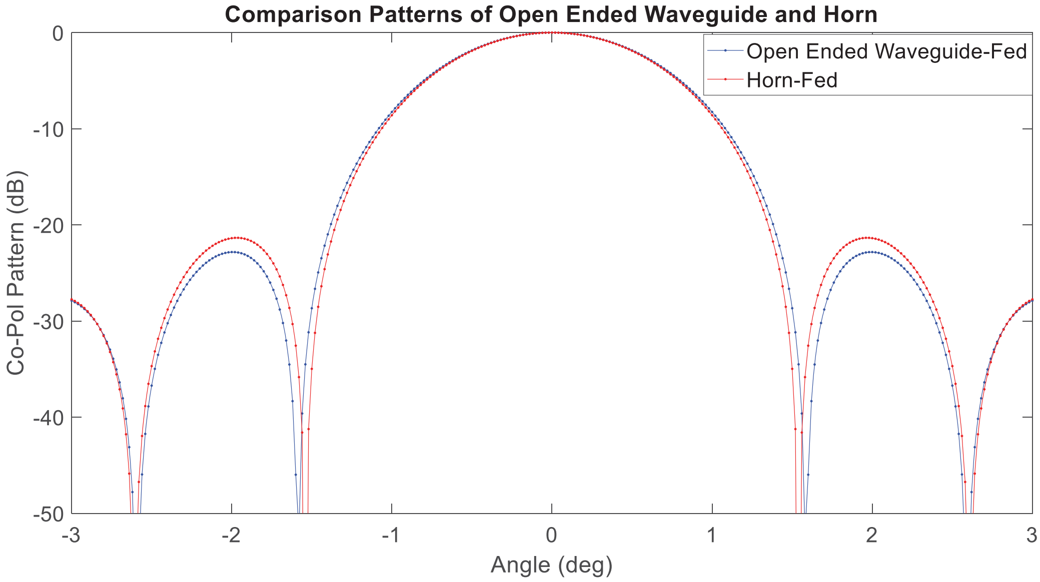

Figure 3.17. Waveguide-Fed and Horn-Fed Front-Fed Reflector Patterns

From the result in Figure 3.17, it can be seen that different feeds used in reflector systems may cause different radiation patterns. Using different feeds which have different incident fields may give rise to larger or narrower beamwidth in the reflector antennas. Also as a trade-off between beamwidth and side lobe level, larger or narrower beamwidth may cause decreasing or increasing side lobe levels, respectively, in the reflector antennas.

To better understand the effect of the feed, some concepts are mentioned in this section. The first concept is spillover efficiency. Let $U_{feed}(\psi, \chi)$ be the feed antenna's radiation intensity. The directivity of an aperture is given in equation (3.27).

$$G_a = \frac{4\pi U_{max}}{P_a} \tag{3.27}$$

where $P_a$ is the total power through the aperture and $U_{max}$ is the maximum value of $U_{feed}(\psi, \chi)$. Also the directivity of a reflector antenna is given in equation (3.28) relative to the total power $P_{feed}$ of the feed antenna.

$$G_{ant}=\frac{4\pi U_{max}}{P_{feed}}=\frac{4\pi U_{max}}{P_a}\frac{P_a}{P_{feed}}= G_a e_{spl} \tag{3.28}$$

The factor $e_{spl}=P_a/P_{feed}$ is referred to as spillover efficiency. It represents the fraction of the power $P_{feed}$ that actually is reflected by the reflector antenna. Spill over efficiency can also be expressed in equation (3.29) relative to $U_{feed}(\psi,\chi)$ (Orfanidis, 1999).

$$e_{spl}=\frac{P_a}{P_{feed}}=\frac{\int_0^{\psi_0}\int_0^{2\pi}U_{feed}(\psi,\chi)\sin\psi\,\mathrm{d}\psi\,\mathrm{d}\chi}{\int_0^{\pi}\int_0^{2\pi}U_{feed}(\psi,\chi)\sin\psi\,\mathrm{d}\psi\,\mathrm{d}\chi} \tag{3.29}$$

The second concept is aperture-taper efficiency. Aperture-taper efficiency is the measure of how uniform the electric field across the antenna's aperture is. Aperture-taper efficiency can be expressed in equation (3.30) relative to $U_{feed}(\psi,\chi)$ (Orfanidis, 1999).

$$\begin{aligned}e_{atl}&=\frac{|\int|E_a|\,dA|^2}{A\int|E_a|^2\,dA}\\&=\frac{1}{\pi}\cot^2\left(\frac{\psi_0}{2}\right)\frac{\left|\int_0^{\psi_0}\int_0^{2\pi}\sqrt{U_{feed}(\psi,\chi)}\tan\left(\frac{\psi}{2}\right)\mathrm{d}\psi\,\mathrm{d}\chi\right|^2}{\int_0^{\psi_0}\int_0^{2\pi}U_{feed}(\psi,\chi)\sin\psi\,\mathrm{d}\psi\,\mathrm{d}\chi}\end{aligned} \tag{3.30}$$

There is a tradeoff between the spillover efficiency and aperture-taper efficiency. If one of them increases, the other decreases. The last concept, illumination efficiency, is related to this tradeoff. It is the product of spillover efficiency and aperture-taper efficiency. It can be expressed in equation (3.31).

$$e_{ill}=\frac{1}{\pi}\cot^2\left(\frac{\psi_0}{2}\right)\frac{\left|\int_0^{\psi_0}\int_0^{2\pi}\sqrt{U_{feed}(\psi,\chi)}\tan\left(\frac{\psi}{2}\right)\mathrm{d}\psi\,\mathrm{d}\chi\right|^2}{\int_0^{\pi}\int_0^{2\pi}U_{feed}(\psi,\chi)\sin\psi\,\mathrm{d}\psi\,\mathrm{d}\chi} \tag{3.31}$$

Illumination efficiency of the feed is the main factor that affects the radiated fields of the reflector antennas. The efficiency values of the feeds in Section 3.2 and 3.3 are listed in Table 3.5.

Table 3.5. Efficiency Values of Waveguide and Horn Feed

| Feed Type | *Spillover Efficiency* | *Aperture-taper Efficiency* | *Illumination Efficiency* |
|---|---|---|---|
| Open Ended Waveguide | 0.33 | 0.46 | 0.15 |
| Horn | 0.85 | 0.44 | 0.38 |

From the results in Table 3.5, it can be seen that the illumination efficiency of the horn is higher than the illumination efficiency of the open ended waveguide. Thus, the beamwidth of the horn-fed reflector is narrower than the beamwidth of the open ended waveguide-fed reflector. On the other hand, the aperture fields of the open-ended waveguide fed-reflector and the horn-fed reflector are compared with each other. To make a correct comparison, the aperture fields are normalized with the total powers of the feed antennas. The total power of the open ended waveguide is given in equation (3.32).

$$P_{waveguide} = \int_{-a/2}^{a/2} \int_{-b/2}^{b/2} \frac{E_w \times H_w^*}{2} \, dy \, dx \tag{3.32}$$

where $E_w$ and $H_w$ are the electric and magnetic fields on the aperture of the open ended waveguide, respectively. $E_w$ is given in equation (3.25) for TE$_{10}$ mode and $H_w$ can be calculated by the relation in equation (3.33) for TE$_{10}$ mode (Cheng, 1983).

$$\begin{gathered} E_w = -Z_{TE}(\hat{z} \times H_w) \\ Z_{TE} = j\omega\mu/\gamma \end{gathered} \tag{3.33}$$

The total power of the horn is given in equation (3.34).

$$P_{horn} = \int_{-A/2}^{A/2} \int_{-B/2}^{B/2} \frac{E_h \times H_h^*}{2} \, dy \, dx \tag{3.34}$$

where $E_h$ and $H_h$ are the electric and magnetic fields on the aperture of the horn, respectively. $E_h$ is obtained in equation (3.26) and $H_h$ can be calculated by the relation in equation (3.35).

$$H_h = H_w e^{-jk\Delta_a - jk\Delta_b} \tag{3.35}$$

The aperture field strength of the open ended waveguide-fed reflector is given in Figure 3.18.

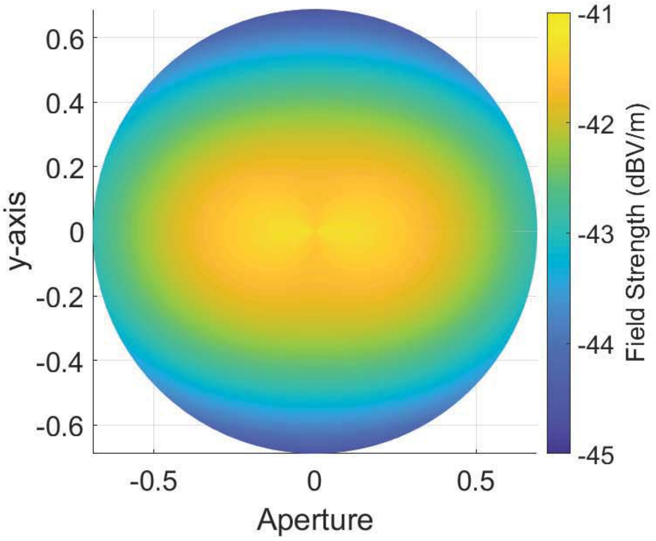

Figure 3.18. Aperture Field Strength of Open Ended Waveguide-Fed Reflector

The aperture field strength of the horn-fed reflector is given in Figure 3.19.

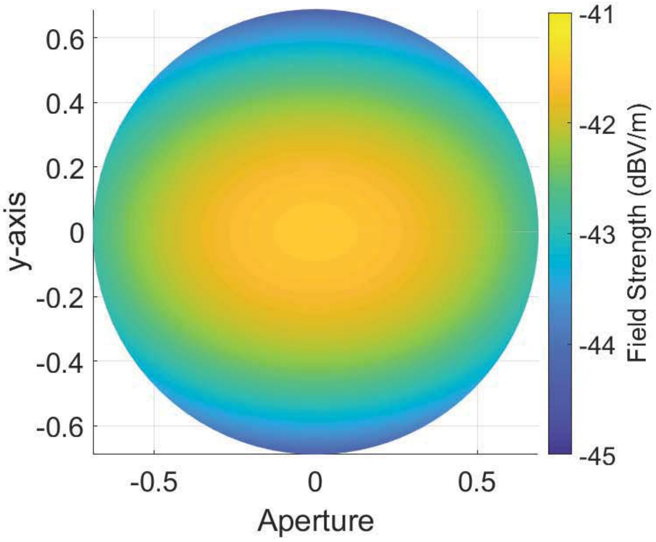

Figure 3.19. Aperture Field Strength of Horn-Fed Reflector

The aperture field in the horn-fed reflector is between -42dB and -44dB while it is between -41.5dB and -44.5dB in the open ended waveguide-fed reflector. Thus, the field at the edge of the reflector is stronger in the horn-fed reflector as compared with the open ended waveguide-fed reflector. Therefore, the field at the side lobe is stronger in the horn-fed reflector; and thus, the side lobe level of the horn-fed reflector is higher than the side lobe level of the open ended waveguide-fed reflector. The importance of narrow beamwidth or low side lobe level for proposed reflector system determines which feed is required for the reflector system. The results obtained in this section are significant for the next sections of this thesis especially when comparing the differences which result from two different feed scenarios of reflectors with each other.

# CHAPTER 4

# CLASSICAL DUAL REFLECTORS

In this chapter, the radiation patterns of classical dual reflectors are obtained and these radiation patterns are compared with the radiation patterns of ring focus reflectors in Chapter 7. By this way, the advantages and disadvantages of the ring focus reflectors are understood.

Classical dual reflectors can be separated into two subcategories. One of them is Cassegrain reflector and the other is Gregorian reflector. Usage of classical dual reflectors is quite widespread in today’s world. Detailed information about them is given in Section 4.1 and 4.2.

## 4.1. Cassegrain Reflector

Cassegrain reflector consists of a paraboloidal main reflector and a hyperboloidal sub-reflector. Having a sub-reflector provides an important advantage for Cassegrain reflector. This advantage is that feed structure whose orientation is toward sub-reflector can be placed near the main reflector; thus, the feed line losses are reduced in Cassegrain reflector.

The geometry of Cassegrain reflector is shown in Figure 4.1.

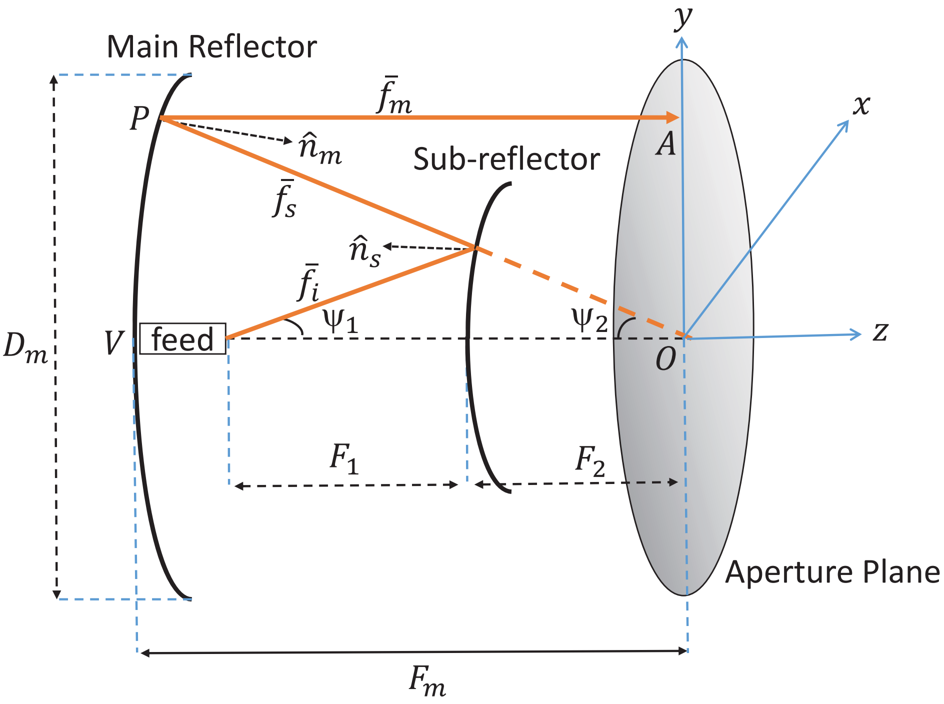

Figure 4.1. Geometry of Cassegrain Reflector

In Figure 4.1, $O$ point shows the focus of the main reflector and $F_1$ and $F_2$ show the foci of the hyperboloidal sub-reflector. The feed is placed on the left focus of the sub-reflector. $D_m$ and $F_m$ represent the diameter of the reflector and focal length of the reflector, respectively. The right focus of the sub-reflector is common with the focus of the main reflector. The rays leaving from the feed are firstly reflected from the sub-reflector and then, they are reflected from the paraboloidal main reflector. And lastly; they proceed to $+z$ direction parallel to $z$ axis. The plane perpendicular to the $z$ axis that passes through the point $O$ is taken as the aperture plane. The phases of all the rays are same on this plane. Thus, all possible ray lengths must be equal for each possible angle of $\psi_1$. $\hat{n}_m$ and $\hat{n}_s$ represent the surface normals of the paraboloidal main reflector and hyperboloidal sub-reflector, respectively. Also, $\bar{f}_i$ is the field incident from the feed, $\bar{f}_s$ is the field reflected from the sub-reflector and $\bar{f}_m$ is the field reflected from the main reflector.

Equations from (3.1) to (3.8) are valid for Cassegrain reflector. The missing part to calculate the radiated fields unlike front-fed reflector is finding of $\hat{n}_s$. The equation of the hyperboloidal sub-reflector is given in equation (4.1).

$$\frac{z^2}{a^2} - \frac{\rho^2}{b^2} = 1 \tag{4.1}$$

In equation (4.1), $\rho$ and $z$ represent the two axes of cylindrical coordinate system. Also, $a$ and $b$ are the sub-reflector parameters, which are shown in Figure 4.2.

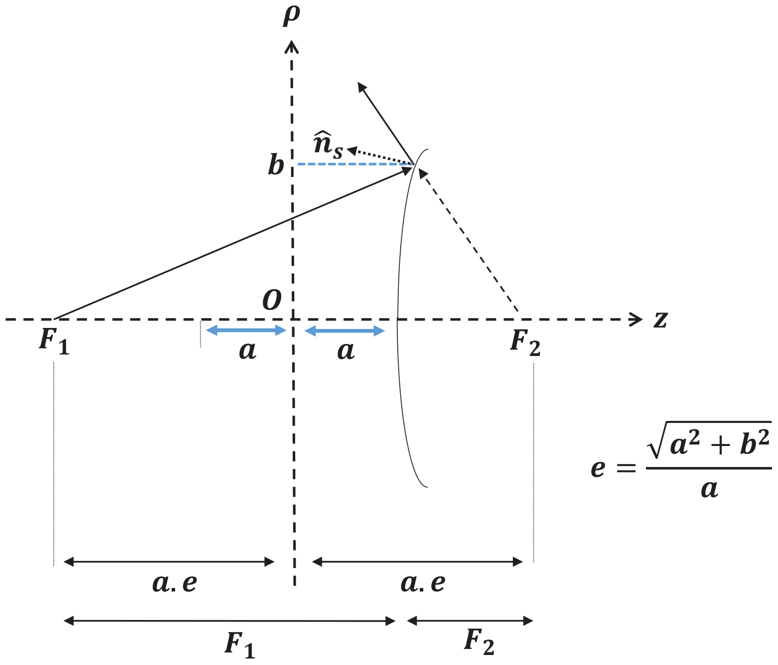

Figure 4.2. Geometry of Hyperbolic Sub-reflector

Normal vector of hyperboloidal sub-reflector can be obtained by taking gradient of equation (4.1).

$$\hat{n}_s = \frac{-\nabla\left(\frac{z^2}{a^2} - \frac{\rho^2}{b^2}\right)}{\left\|\nabla\left(\frac{z^2}{a^2} - \frac{\rho^2}{b^2}\right)\right\|} \tag{4.2}$$

By using $\bar{\rho} = x\hat{x} + y\hat{y}$ and $\rho^2 = x^2 + y^2$:

$$\hat{n}_s = \frac{-1}{\sqrt{\frac{x^2+y^2}{b^4}+\frac{z^2}{a^4}}}\left[-\frac{x}{b^2}\hat{x}-\frac{y}{b^2}\hat{y}+\frac{z}{a^2}\hat{z}\right] \tag{4.3}$$

Once $\hat{n}_s$ is obtained, the field reflected from the main reflector can be found by using equation (3.1) and (3.2). Then, the radiated fields are obtained by putting these into equation (2.11) and (2.12).

The analyzed radiation pattern of the Cassegrain reflector, which is obtained by using Aperture-Field Method, and the simulated radiation pattern of the Cassegrain reflector, which is obtained by using electromagnetic simulation tool CST Microwave Studio, are compared with each other in order to show how analyzed result is close to real reflector pattern. In this comparison, WR90 open ended waveguide feed (which operates in 8.2-12.4 GHz) is used as the feed antenna. The field incident from the feed antenna must be known in order to achieve the radiation fields of reflectors in Aperture-Field Method. For this aim, equation (3.24) is used to get the field incident from WR90. The chosen parameters of the Cassegrain reflector used in this comparison are listed in Table 4.1.

Table 4.1. Chosen Parameters of Cassegrain Reflector

| Parameter Name | Parameter Value |
|---|---|
| Main reflector diameter ($D_m$) | 600 mm |
| Main reflector focal length ($F_m$) | 300 mm |
| Distance between foci | 42 mm |
| Sub-reflector eccentricity | 2.1 |
| Operating frequency ($f$) | 10 GHz |

The comparison result is given in Figure 4.3.

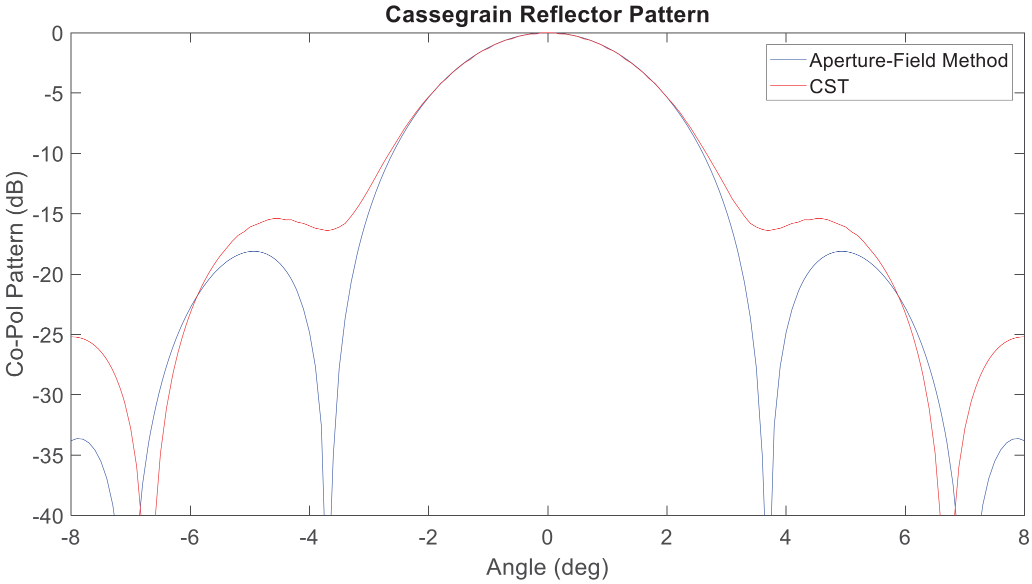

Figure 4.3. Results of Aperture-Field Method and CST Microwave Studio for Cassegrain Reflector

From Figure 4.3, it can be seen that the result obtained by Aperture-Field Method and the result obtained by CST Microwave Studio are quite similar in the main beam of Cassegrain reflector. The differences between these two radiation patterns result from that CST Microwave Studio is a full-wave simulator and it includes many effects which are not taken into account in Aperture-Field Method such as diffraction, multi-reflection etc. Thus, these radiation patterns usually do not become exactly the same with each other. When investigating these two radiation patterns in detail, it can also be seen that Aperture-Field Method cannot calculate the null filling on the pattern correct enough since it does not take into account the diffraction. Due to the same reason, the result obtained by Aperture-Field Method becomes inaccurate as we move away from the boresight of the antenna and the side lobe level obtained by Aperture-Field Method may become different from the side lobe level obtained by CST Microwave Studio. On the other hand, Aperture-Field Method calculates the main lobe very accurately. For example, the 3dB beamwidth obtained by Aperture-Field Method is 3.24° while the 3dB beamwidth obtained by CST Microwave Studio is 3.30°. Also, Aperture-Field Method is successful in predicting the positon of nulls.

## 4.2. Gregorian Reflector

Gregorian reflector consists of a paraboloidal main reflector and an ellipsoidal sub-reflector. The feed structure can be placed near the main reflector like in Cassegrain reflector. However, due to natural geometries of Cassegrain and Gregorian reflectors, the total reflector length in Gregorian reflector is longer than the total reflector length in Cassegrain reflector for the same reflector diameter and focal length. Thus, Cassegrain reflectors are preferred in the applications that total reflector length is critical.

The geometry of Gregorian reflector is given in Figure 4.4.

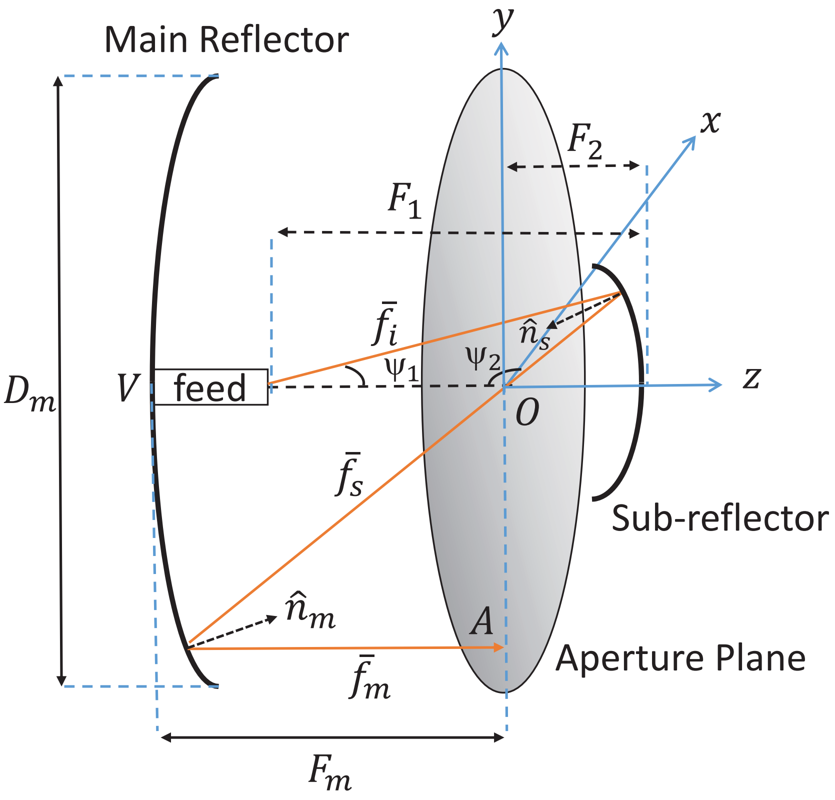

Figure 4.4. Geometry of Gregorian Reflector

In Figure 4.4, $O$ point shows the focus of the main reflector and $F_1$ and $F_2$ show the foci of the sub-reflector. The feed is placed on the left focus of the sub-reflector. $D_m$ and $F_m$ represent the diameter of the reflector and focal length of the reflector, respectively. The right focus of the sub-reflector is common with the focus of the main reflector. The rays leaving the feed are reflected from the sub-reflector and then, they are reflected from the paraboloidal main reflector. And lastly; they proceed to $+z$ direction parallel to $z$ axis. The plane perpendicular to the $z$ axis that passes through the point $O$ is taken as the aperture plane. The phases of all the rays are same on this plane. Thus, all possible ray lengths must be equal for each possible angle of $\psi_1$. $\hat{n}_m$ and $\hat{n}_s$ represent the surface normal of the paraboloidal main reflector and ellipsoidal sub-reflector, respectively. Also, $\bar{f}_i$ is the field incident from the feed, $\bar{f}_s$ is the field reflected from the sub-reflector and $\bar{f}_m$ is the field reflected from the main reflector.

Equations from (3.1) to (3.8) are valid for Gregorian reflector. The expression for $\hat{n}_s$ for a Gregorian reflector is different from that of a Cassegrain reflector, since Gregorian reflector has an ellipsoidal sub-reflector instead of a hyperboloidal sub-reflector. The equation of ellipsoidal sub-reflector is given in equation (4.4).

$$\frac{z^2}{a^2} + \frac{\rho^2}{b^2} = 1 \tag{4.4}$$

In equation (4.4), $\rho$ and $z$ represent the two axes of cylindrical coordinate system, and $a$ and $b$ represent sub-reflector parameters as in Cassegrain reflector.

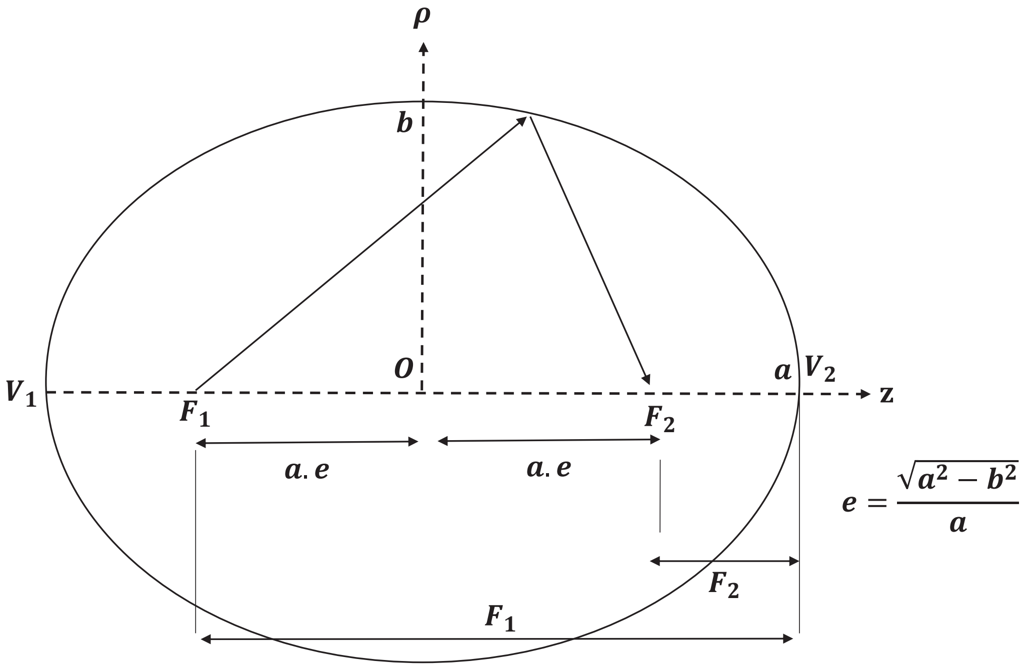

Figure 4.5. Geometry of Ellipsoidal Sub-reflector

Normal vector of ellipsoidal sub-reflector can be obtained by taking gradient of equation (4.4).

$$\hat{n}_s = \frac{-\nabla\left(\frac{z^2}{a^2} + \frac{\rho^2}{b^2}\right)}{\left\|\nabla\left(\frac{z^2}{a^2} + \frac{\rho^2}{b^2}\right)\right\|} \tag{4.5}$$

By using $\bar{\rho} = x\hat{x} + y\hat{y}$ and $\rho^2 = x^2 + y^2$:

$$\hat{n}_s = \frac{-1}{\sqrt{\frac{x^2 + y^2}{b^4} + \frac{z^2}{a^4}}}\left[\frac{x}{b^2}\hat{x} + \frac{y}{b^2}\hat{y} + \frac{z}{a^2}\hat{z}\right] \tag{4.6}$$

Once $\hat{n}_s$ is obtained, the field reflected from the main reflector can be found by using equation (3.1) and (3.2). Then, the radiated fields are obtained by putting these into equation (2.11) and (2.12).

The analyzed radiation pattern of the Gregorian reflector, which is obtained by using Aperture-Field Method, and the simulated radiation pattern of the Gregorian reflector, which is obtained by using electromagnetic simulation tool CST Microwave Studio, are compared with each other in order to show how analyzed result is close to real reflector pattern. In this comparison, WR90 open ended waveguide feed (which operates in 8.2-12.4 GHz) is used as the feed antenna. The field incident from the feed antenna must be known in order to achieve the radiation fields of reflectors in Aperture-Field Method. For this aim, equation (3.24) is used to get field incident from WR90. The chosen parameters of the Gregorian reflector used in this comparison are listed in Table 4.2.

Table 4.2. Chosen Parameters of Gregorian Reflector

| Parameter Name | Parameter Value |
|---|---|
| Main reflector diameter ($D_m$) | 600 mm |
| Main reflector focal length ($F_m$) | 300 mm |
| Distance between foci | 363 mm |
| Sub-reflector eccentricity | 0.48 |
| Operating frequency ($f$) | 10 GHz |

The comparison result is shown in Figure 4.6.

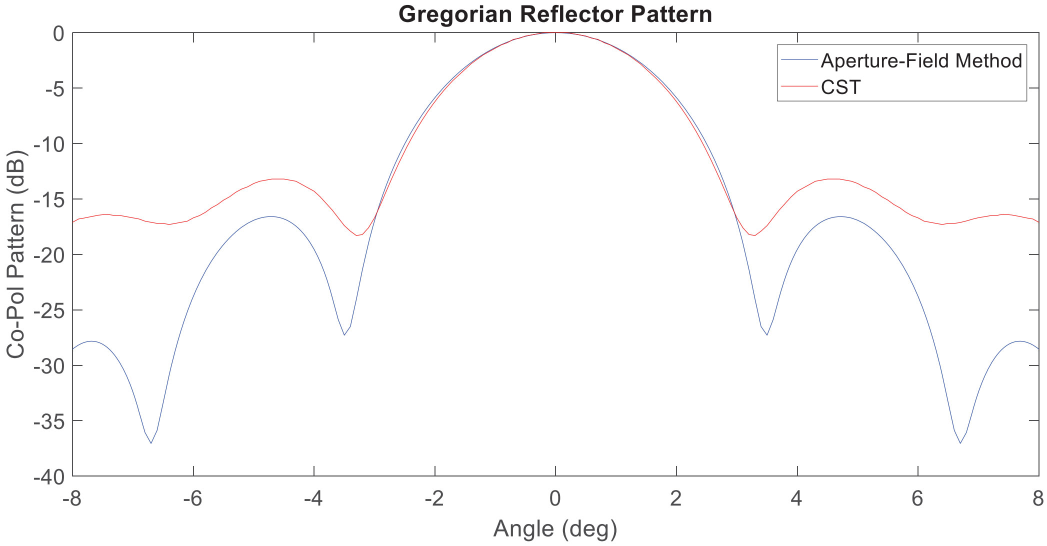

Figure 4.6. Results of Aperture-Field Method and CST Microwave Studio for Gregorian Reflector

As can be seen from the comparison of the results given in Figure 4.6, the radiation pattern of Gregorian reflector obtained by Aperture-Field Method is very close to that obtained by full wave analysis using CST Microwave Studio in the main beam. The 3dB beamwidth obtained by these methods are 3.30° and 3.25°, respectively. Outside the main beam, these results are different. As mentioned previously in section 4.1, Aperture-Field Method is a very rough approximation which excludes diffraction effects, spill-over etc. In the side lobe region, side lobe levels and null depths are not calculated accurately, but the position of the nulls and side-lobe peaks are more accurate.

# CHAPTER 5

# SINGLE OFFSET RING FOCUS DUAL REFLECTORS

Single Offset Ring Focus Dual Reflectors have two types as Cassegrain and Gregorian. The name of Single Offset means that the distance between bottom edge of half main reflector and bottom edge of half sub-reflector equals half of the sub-reflector diameter ($D_s/2$ ).

## 5.1. Single Offset Ring Focus Cassegrain Reflector

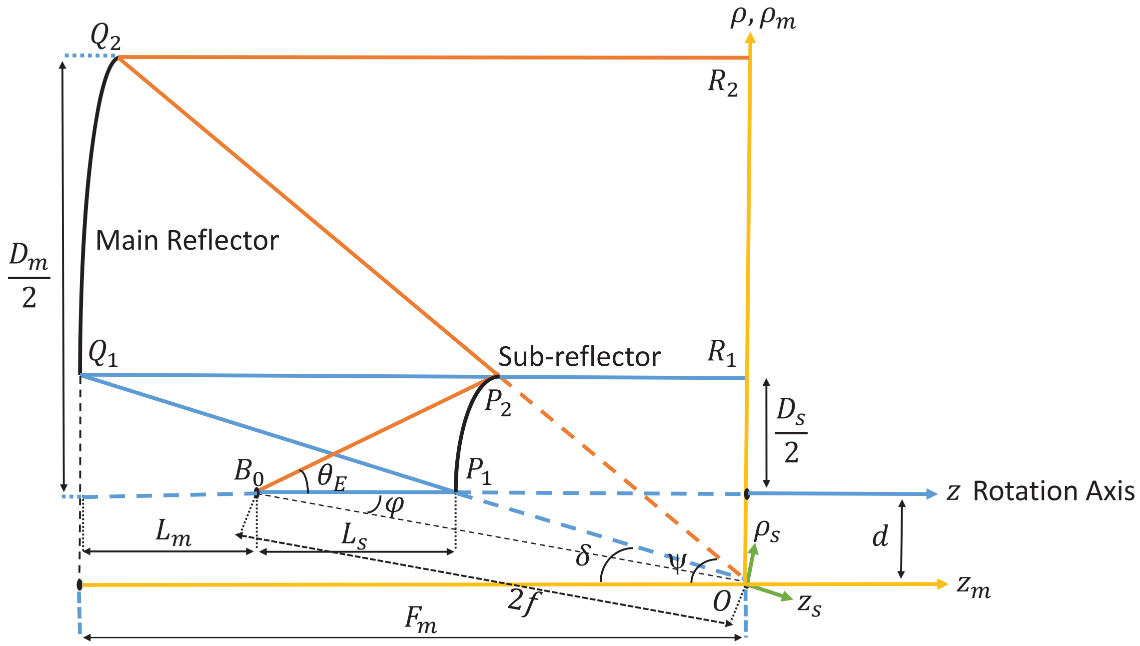

Figure 5.1. Geometry of Single Offset Ring Focus Cassegrain Reflector

The geometry of Single Offset Ring Focus Cassegrain antenna is shown in Figure 5.1, which shows a cross-section of the antenna. The 3D figure can be obtained by rotating the structure about the $z$ axis (Rotation axis) indicated in the figure. The black solid curve between $Q_1$ and $Q_2$ is the truncated parabolic main reflector with its focus at $O$, and the black solid curve between $P_1$and $P_2$ is the displaced-axis hyperbolic sub-reflector with one focus at $O$ and the other at $B_0$. The feed is located at this focus $B_0$ of the sub-reflector. We use cylindrical coordinates to describe the main and sub-reflectors, denoted, respectively, by $\rho_m$, $z_m$ and $\rho_s$, $z_s$, both having their origins at $O$. Note that the sub-reflector coordinate system is rotated with respect to main reflector system by an angle $\varphi$. $O$ is the common focus of the two reflectors and is displaced by a distance "$d$" from the rotation axis. When the curves $Q_1Q_2$ and $P_1P_2$ are rotated about the $z$ axis, we obtain the figure of revolution shown in Figure 5.2. Since $O$ is displaced from the rotation axis, the common focal point traces a circle under this rotation and hence the name ring focus. Propagation paths of two rays that go through the edges of the reflectors are also shown in Figure 5.1 by the blue and red solid lines. All other ray paths lie between these two paths.

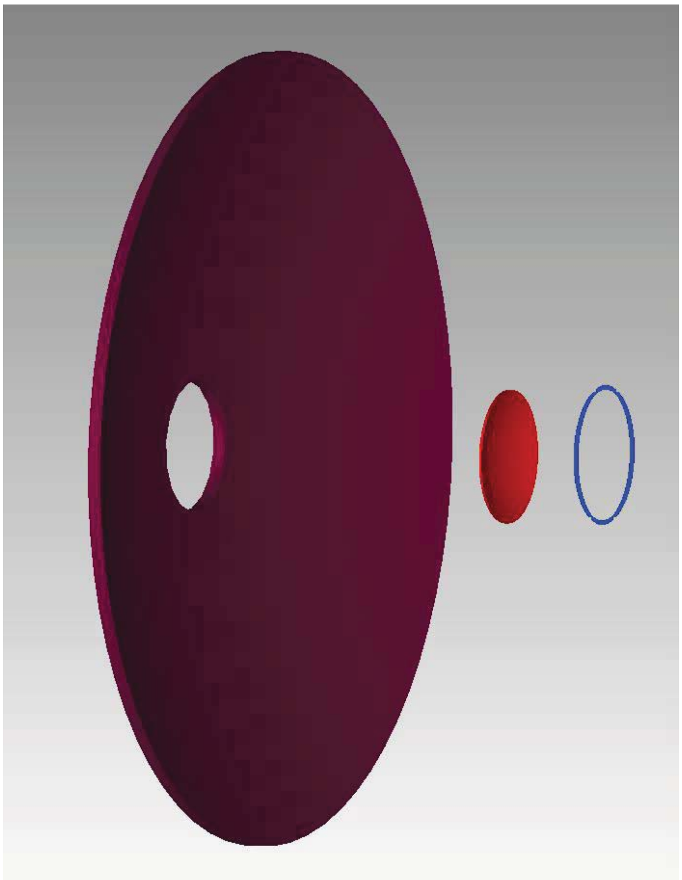

Figure 5.2. Three Dimensional Appearance of SORF Cassegrain Reflector

In Figure 5.2, purple, red and blue shapes represent the three dimensional appearance of the truncated parabolic main reflector, displaced-axis hyperbolic sub-reflector and ring focus, respectively. As shown in this figure, the focus is annular and there is a hole in the main reflector.

There are many parameters which take part in the geometry of Single Offset Ring Focus Cassegrain, but only four parameters ($D_m, F_m, D_s, \theta_E$) are enough to describe the full geometry. Other parameters can be expressed in terms of these four parameters. The descriptions of all parameters are listed in Table 5.1.

Table 5.1. Parameter Description of SORF Cassegrain Reflector

| Symbol | Description |
|---|---|
| $D_m$ | Main reflector diameter |
| $F_m$ | Main reflector focal length |
| $D_s$ | Sub-reflector diameter |
| $\theta_E$ | Angle between the $z$ axis and the ray emanating from the focus of the sub- reflector in the direction of sub-reflector edge |
| $B_0$ | Feed position |
| $\varphi$ | Offset angle between main reflector and sub-reflector coordinate systems (counter clockwise) |
| $\psi$ | Angle between the $z$ axis of the main reflector and the ray emanating from the origin in the direction of main reflector top edge |
| $\delta$ | Angle between the $z$ axis of the main reflector and the ray emanating from the origin in the direction of main reflector bottom edge |
| $L_s$ | Distance between the focus and apex of sub-reflector |
| $L_m$ | Distance between the focus and the projection of bottom edge of main reflector onto $z$ axis |
| $2f$ | Focal length of sub-reflector |
| $d$ | Offset parameter |

The coordinates of the parameters given in Figure 5.1 are presented in Table 5.2 (Granet, 1999).

Table 5.2. Coordinates of SORF Cassegrain Parameters

| Point | $\rho_m$ | $z_m$ |
|---|---|---|
| $Q_1$ | $\frac{D_s}{2}+d$ | $\frac{(D_s+2d)^2}{16F_m}-F_m$ |
| $Q_2$ | $\frac{D_m}{2}+d$ | $\frac{(D_m+2d)^2}{16F_m}-F_m$ |
| $P_1$ | $d$ | $\frac{2d\left(\frac{(D_s+2d)^2}{16F_m}-F_m\right)}{D_s+2d}$ |
| $P_2$ | $\frac{D_s}{2}+d$ | $\frac{(D_s+2d)\left(\frac{(D_m+2d)^2}{16F_m}-F_m\right)}{D_m+2d}$ |
| $R_1$ | $\frac{D_s}{2}+d$ | 0 |
| $R_2$ | $\frac{D_m}{2}+d$ | 0 |
| $B_0$ | $d$ | $\frac{(D_s+2d)\left(\frac{(D_m+2d)^2}{16F_m}-F_m\right)}{D_m+2d}-\frac{D_s}{2\tan(\theta_E)}$ |

Equations from (3.1) to (3.8) are valid for Single Offset Ring Focus Cassegrain reflector. However, we need to find the expression of $\hat{n}_s$. A complication is that the sub-reflector surface is defined in the sub-reflector coordinate system but we need the expression of $\hat{n}_s$ in the main reflector coordinate system. Thus, we need to relate the two coordinate systems.

The relations of main reflector and sub-reflector coordinate systems are given in equation (5.1).

$$\begin{aligned} z_m &= \cos(\varphi)\, z_s - \sin(\varphi)\rho_s \\ \rho_m &= \sin(\varphi)\, z_s + \cos(\varphi)\rho_s \end{aligned} \tag{5.1}$$

where $\varphi$ is defined in Table 5.1, and note that its direction is counter clockwise, i.e. its numerical value is negative in Figure 5.1.

By using equation (4.2) and (5.1), the normal vector of the sub-reflector of Single Offset Ring Focus Cassegrain reflector can be obtained.

$$
\begin{aligned}
\hat{n}_s &= \hat{n}_{s\rho} + \hat{n}_{sz} \\
\hat{n}_{s\rho} &= \frac{1}{\sqrt{\frac{x^2+y^2}{b^4}+\frac{z^2}{a^4}}}\left(\frac{z\sin(\varphi)}{a^2}+\frac{x\cos(\varphi)}{b^2}+\frac{y\cos(\varphi)}{b^2}\right)\hat{\rho} \\
\hat{n}_{sz} &= \frac{1}{\sqrt{\frac{x^2+y^2}{b^4}+\frac{z^2}{a^4}}}\left(\frac{z\cos(\varphi)}{a^2}-\frac{x\sin(\varphi)}{b^2}-\frac{y\sin(\varphi)}{b^2}\right)\hat{z}
\end{aligned}
\tag{5.2}
$$

The parameters $a$ and $b$ in equation (5.2) can be expressed in terms of four parameters $(D_m, F_m, D_s, \theta_E)$ for Single Offset Ring Focus Cassegrain reflector.

$$
\begin{aligned}
a &= \frac{\left(|B_0P_1| - \sqrt{\left(P_{1\rho_m}\right)^2 + \left(P_{1z_m}\right)^2}\right)}{2} \\
b &= \sqrt{\frac{\left(B_{0\rho_m}\right)^2 + \left(B_{0z_m}\right)^2}{4} - a^2}
\end{aligned}
\tag{5.3}
$$

Once $\hat{n}_s$ is obtained, the field reflected from the main reflector can be found by using equation (3.1) and (3.2). Then, the radiated fields are obtained by putting these into equations (2.11) and (2.12) as in previous sections.

The analyzed radiation pattern of the Single Offset Ring Focus Cassegrain reflector, which is obtained by using Aperture-Field Method, and the simulated radiation pattern of the Single Offset Ring Focus Cassegrain reflector, which is obtained by using electromagnetic simulation tool CST Microwave Studio, are compared with each other in order to show how analyzed result is close to real reflector pattern. In this comparison, WR90 open ended waveguide feed (which operates in 8.2-12.4 GHz) is used as the feed antenna. The field incident from the feed antenna must be known in order to achieve the radiation fields of reflectors in Aperture-Field Method. For this aim, equation (3.24) is used to get field incident from WR90. The chosen parameters of the Single Offset Ring Focus Cassegrain reflector used in this comparison are listed in Table 5.3.

Table 5.3. Chosen Parameters of SORF Cassegrain Reflector

| Parameter Name | Parameter Value |
|---|---|
| Main reflector diameter ($D_m$) | 600 mm |
| Main reflector focal length ($F_m$) | 300 mm |
| Sub-reflector diameter ($D_s$) | 100 mm |
| Sub-reflector subtended angle ($\theta_E$) | 20° |
| Operating frequency ($f$) | 10 GHz |

The comparison result is shown in Figure 5.3.

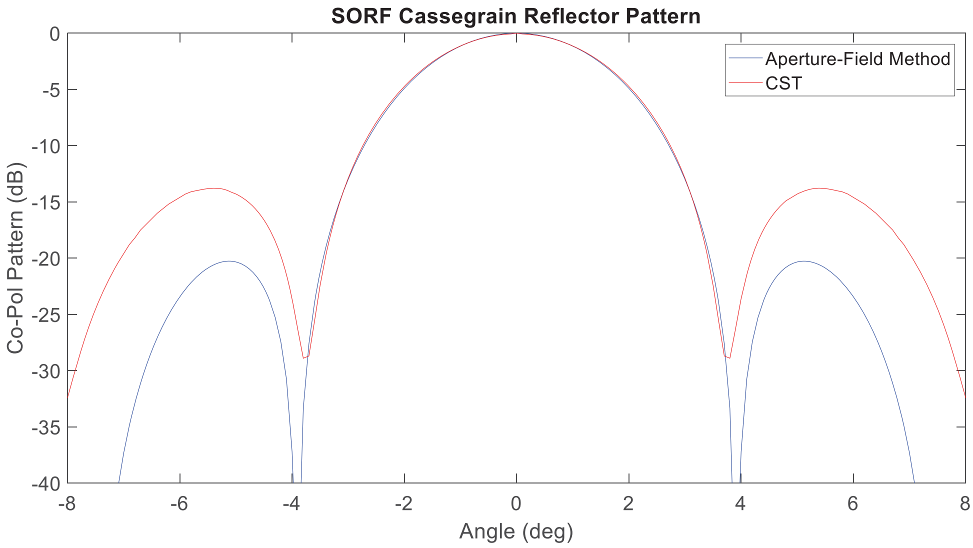

Figure 5.3. Results of Aperture-Field Method and CST Microwave Studio for SORF Cassegrain Reflector

From the result in Figure 5.3, it can be seen that the result of Aperture-Field Method and the result of CST Microwave Studio are almost the same in the main beam of SORF Cassegrain reflector, although there are significant differences between them outside the main beam. The reason of these differences is related to diffraction as referred in Chapter 4. The comments on the miscalculation of the null filling in

Chapter 4 are also valid for SORF Cassegrain reflector. Also, the 3dB beamwidths obtained by Aperture-Field Method and CST Microwave Studio are 3.18° and 3.24°, respectively.

## 5.2. Single Offset Ring Focus Gregorian Reflector

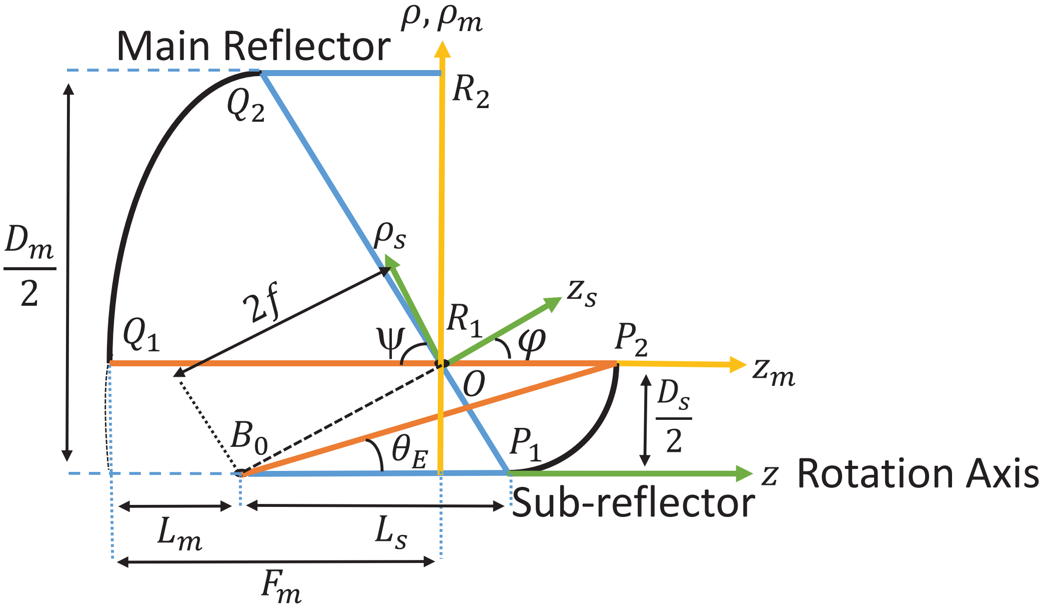

Figure 5.4. Geometry of Single Offset Ring Focus Gregorian Reflector

The geometry of Single Offset Ring Focus Gregorian antenna is shown in Figure 5.4, which shows a cross-section of the antenna. The 3D figure can be obtained by rotating the structure about the $z$ axis (Rotation axis) indicated in the figure. The black solid curve between $Q_1$ and $Q_2$ is the truncated parabolic main reflector with its focus at $O$, and the black solid curve between $P_1$ and $P_2$ is the displaced-axis elliptic sub-reflector with one focus at $O$ and the other at $B_0$. The feed is located at this focus $B_0$ of the sub-reflector. We use cylindrical coordinates to describe the main and sub-reflectors, denoted, respectively, by $\rho_m$, $z_m$ and $\rho_s$, $z_s$, both having their origins at $O$. Note that the sub-reflector coordinate system is rotated with respect to main reflector system by an angle $\varphi$. $O$ is the common focus of the two reflectors and is displaced by a distance "$d$" from the rotation axis. When the curves $Q_1Q_2$ and $P_1P_2$ are rotated about the $z$

axis, we obtain the figure of revolution shown in Figure 5.5. Since $O$ is displaced from the rotation axis, the common focal point traces a circle under this rotation and hence the name ring focus. Propagation paths of two rays that go through the edges of the reflectors are also shown in Figure 5.4 by the blue and red solid lines. All other ray paths lie between these two paths.

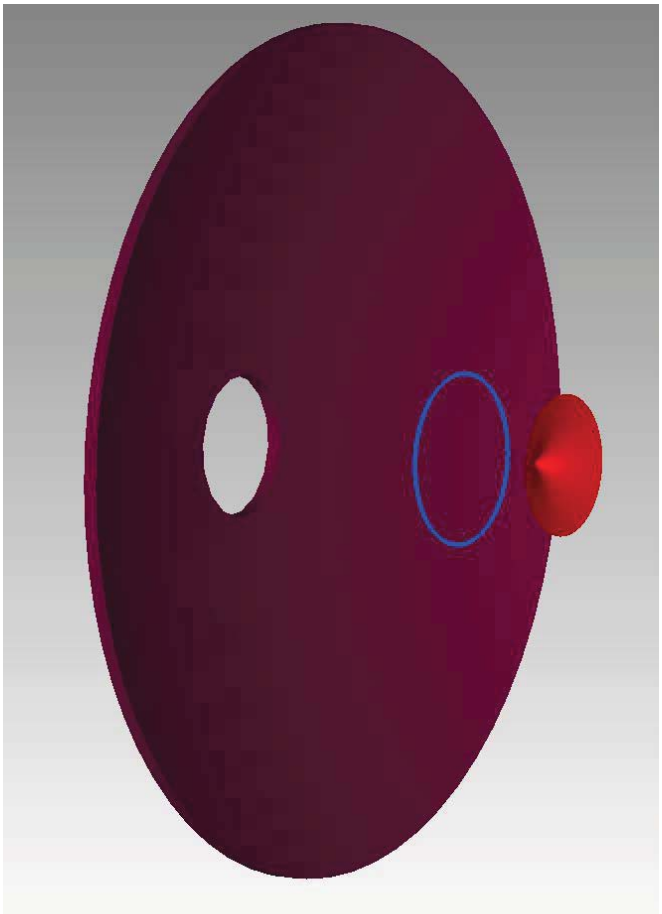

Figure 5.5. Three Dimensional Appearance of SORF Gregorian Reflector

In Figure 5.5, purple, red and blue shapes represent the three dimensional appearance of the truncated parabolic main reflector, displaced-axis elliptic sub-reflector and ring focus, respectively. As shown in this figure, the focus is annular and there is a hole in the main reflector.

As in all ring focus dual reflectors, only four parameters ($D_m, F_m, D_s, \theta_E$) are enough to describe the full geometry of Single Offset Ring Focus Gregorian reflector and the other parameters can be expressed in terms of these four parameters. The descriptions of all parameters are listed in Table 5.1.

The coordinates of the parameters given in Figure 5.4 are presented in Table 5.4 (Granet, 1999).

Table 5.4. Coordinates of SORF Gregorian Parameters

| Point | $y_m$ | $z_m$ |
|---|---|---|
| $Q_1$ | $0$ | $-F_m$ |
| $Q_2$ | $\frac{D_m - D_s}{2}$ | $-\left(\frac{D_m - D_s}{2}\right)\cot(\psi)$ |
| $P_1$ | $-\frac{D_s}{2}$ | $L_s + L_m - F_m$ |
| $P_2$ | $0$ | $\left(\frac{D_s}{2}\cot(\theta_E) - L_s\right) + L_s + L_m - F_m$ |
| $R_1$ | $0$ | $0$ |
| $R_2$ | $\frac{D_m - D_s}{2}$ | $0$ |
| $B_0$ | $-\frac{D_s}{2}$ | $L_m - F_m$ |

Except main four parameters, other required parameters in Table 5.4 are expressed in equations (5.4) to (5.8) in terms of main four parameters.

$$L_m = \frac{F_m D_m}{D_m - D_s} - \frac{D_s}{4}\left[\frac{\cos(\theta_E) + 1}{\sin(\theta_E)}\right] \tag{5.4}$$

$$\varphi = \operatorname{atan}\left(\frac{2}{\frac{\cos(\theta_E) + 1}{\sin(\theta_E)} - \frac{4F_m}{D_m - D_s}}\right) \tag{5.5}$$

$$f = \frac{D_s}{4\sin(\varphi)} \tag{5.6}$$

$$\psi = \operatorname{atan}\left(\frac{8F_m(D_m - D_s)}{(D_m - D_s)^2 - 16F_m^2}\right) \tag{5.7}$$

$$L_s = 2f\cos(\varphi) + \frac{D_s}{2\tan(\psi)} \tag{5.8}$$

Besides, $d$ and $\delta$ are zero for Single Offset Ring Focus Gregorian reflector. Equations from (3.1) to (3.8) are valid for Single Offset Ring Focus Gregorian reflector. However, we need to find the expression of $\hat{n}_s$. A complication is that the sub-reflector surface is defined in the sub-reflector coordinate system but we need the expression of $\hat{n}_s$ in the main reflector coordinate system. Thus, we need to relate the two coordinate systems.

The relations of main reflector and sub-reflector coordinate systems are given in equation (5.1). By using equation (4.5) and (5.1), the normal vector of the sub-reflector of Single Offset Ring Focus Gregorian reflector can be obtained.

$$\begin{gathered}
\hat{n}_s = \hat{n}_{s\rho} + \hat{n}_{sz} \\
\hat{n}_{s\rho} = \frac{1}{\sqrt{\frac{x^2+y^2}{b^4} + \frac{z^2}{a^4}}}\left(\frac{z\sin(\varphi)}{a^2} - \frac{x\cos(\varphi)}{b^2} - \frac{y\cos(\varphi)}{b^2}\right)\hat{\rho} \\
\hat{n}_{sz} = \frac{1}{\sqrt{\frac{x^2+y^2}{b^4} + \frac{z^2}{a^4}}}\left(\frac{z\cos(\varphi)}{a^2} + \frac{x\sin(\varphi)}{b^2} + \frac{y\sin(\varphi)}{b^2}\right)\hat{z}
\end{gathered} \tag{5.9}$$

The parameters $a$ and $b$ in equation (5.9) can be expressed in terms of four parameters $(D_m, F_m, D_s, \theta_E)$ for Single Offset Ring Focus Gregorian reflector.

$$\begin{aligned} a &= \frac{D_s}{8}\left[\frac{\cos(\theta_E)+1}{\sin(\theta_E)}\right] + \frac{F_m D_s}{2(D_m - D_s)} \\ b &= \sqrt{\left(\frac{D_s}{4\sin(\varphi)}\right)^2 + a^2} \end{aligned} \tag{5.10}$$

Once $\hat{n}_s$ is obtained, the field reflected from the main reflector can be found by using equation (3.1) and (3.2). Then, the radiated fields are obtained by putting these into equations (2.11) and (2.12) as in previous sections.

The analyzed radiation pattern of the Single Offset Ring Focus Gregorian reflector, which is obtained by using Aperture-Field Method, and the simulated radiation pattern of the Single Offset Ring Focus Gregorian reflector, which is obtained by using electromagnetic simulation tool CST Microwave Studio, are compared with each other in order to show how analyzed result is close to real reflector pattern. In this comparison, WR90 open ended waveguide feed (which operates in 8.2-12.4 GHz) is used as the feed antenna. The field incident from the feed antenna must be known in order to achieve the radiation fields of reflectors in Aperture-Field Method. For this aim, equation (3.24) is used to get the field incident from WR90. The chosen parameters of the Single Offset Ring Focus Gregorian reflector used in this comparison are listed in Table 5.5.

Table 5.5. Chosen Parameters of SORF Gregorian Reflector

| Parameter Name | Parameter Value |
|---|---|
| Main reflector diameter ($D_m$) | 600 mm |
| Main reflector focal length ($F_m$) | 300 mm |
| Sub-reflector diameter ($D_s$) | 100 mm |
| Sub-reflector subtended angle ($\theta_E$) | 20° |
| Operating frequency ($f$) | 10 GHz |

The comparison result is shown in Figure 5.6.

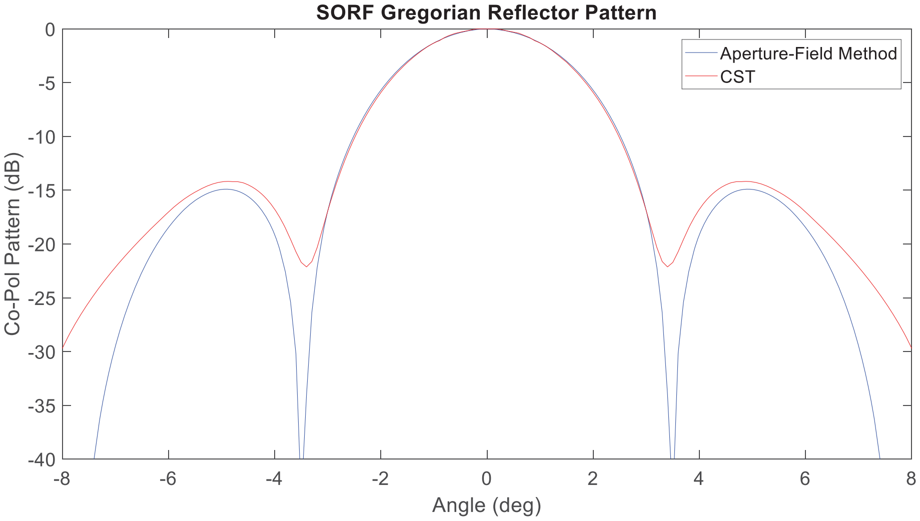

Figure 5.6. Results of Aperture-Field Method and CST Microwave Studio for SORF Gregorian Reflector

The result in Figure 5.6 shows the parallelism of the results of Aperture-Field Method and CST Microwave Studio in the main beam of SORF Gregorian reflector. The 3dB beamwidths are calculated as 2.92° with Aperture-Field Method, it is found to be 3.04° from CST Microwave Studio. The results of Aperture-Field Method and CST Microwave Studio agree well in the main beam, but the results of Aperture-Field Method are not accurate outside the main beam due to the reason explained previously in Chapter 4.

# CHAPTER 6

# DOUBLE OFFSET RING FOCUS DUAL REFLECTORS

Double Offset Ring Focus Dual Reflectors have two types as Cassegrain and Gregorian like in Single Offset Ring Focus Dual Reflectors. The name of Double Offset means that the distance between bottom edge of half main reflector and bottom edge of half sub-reflector equals the sub-reflector diameter ($D_s$).

## 6.1. Double Offset Ring Focus Cassegrain Reflector

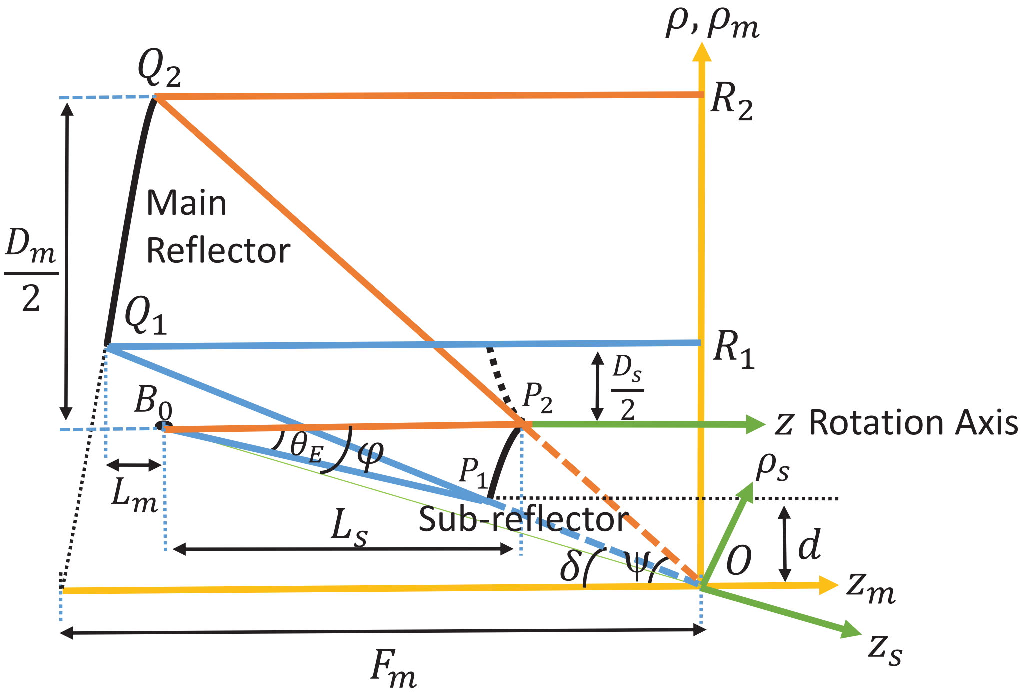

Figure 6.1. Geometry of Double Offset Ring Focus Cassegrain Reflector

The geometry of Double Offset Ring Focus Cassegrain antenna is shown in Figure 6.1, which shows a cross-section of the antenna. The 3D figure can be obtained by rotating the structure about the *z* axis (Rotation axis) indicated in the figure. The black solid curve between $Q_1$ and $Q_2$ is the truncated parabolic main reflector with its focus at $O$, and the black solid curve between $P_1$and $P_2$ is the displaced-axis hyperbolic sub-reflector with one focus at $O$ and the other at $B_0$. The feed is located at this focus $B_0$ of the sub-reflector. We use cylindrical coordinates to describe the main and sub-reflectors, denoted, respectively, by $\rho_m$, $z_m$ and $\rho_s$, $z_s$, both having their origins at $O$. Note that the sub-reflector coordinate system is rotated with respect to main reflector system by an angle $\varphi$. $O$ is the common focus of the two reflectors and is displaced by a distance "$d$" from the rotation axis. When the curves $Q_1Q_2$ and $P_1P_2$ are rotated about the $z$ axis, we obtain the figure of revolution shown in Figure 6.2. Since $O$ is displaced from the rotation axis, the common focal point traces a circle under this rotation and hence the name ring focus. Propagation paths of two rays that go through the edges of the reflectors are also shown in Figure 6.1 by the blue and red solid lines. All other ray paths lie between these two paths.

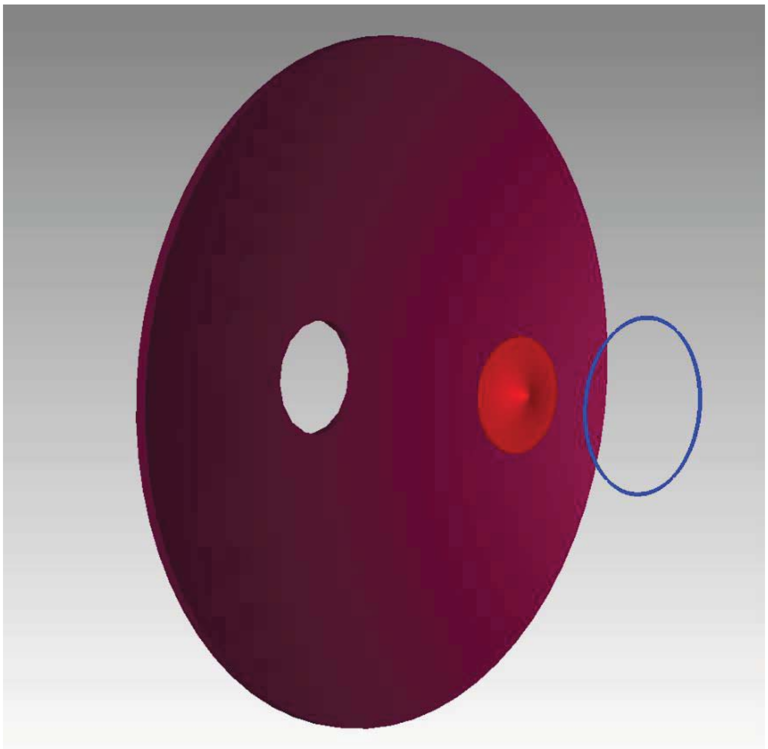

Figure 6.2. Three Dimensional Appearance of DORF Cassegrain Reflector

In Figure 6.2, purple, red and blue shapes represent the three dimensional appearance of the truncated parabolic main reflector, displaced-axis hyperbolic sub-reflector and ring focus, respectively. As shown in this figure, the focus is annular and there is a hole in the main reflector.

As in all ring focus dual reflectors, only four parameters ($D_m, F_m, D_s, \theta_E$) are enough to describe the full geometry of Double Offset Ring Focus Cassegrain reflector and the other parameters can be expressed in terms of these four parameters. The descriptions of all parameters are listed in Table 5.1.

The coordinates of the parameters given in Figure 6.1 are presented in Table 6.1 (Granet, 1999).

Table 6.1. Coordinates of DORF Cassegrain Parameters

| Point | $y_m$ | $z_m$ |
|---|---|---|
| $Q_1$ | $D_s + d$ | $\frac{(D_s + d)^2}{4F_m} - F_m$ |
| $Q_2$ | $\frac{D_m + D_s + 2d}{2}$ | $\frac{(D_m + D_s + 2d)^2}{16F_m} - F_m$ |
| $P_1$ | $d$ | $\frac{d\left[\frac{(D_s + d)^2}{4F_m} - F_m\right]}{D_s + d}$ |
| $P_2$ | $\frac{D_s + 2d}{2}$ | $\frac{(D_s + 2d)\left[\frac{(D_m + D_s + 2d)^2}{16F_m} - F_m\right]}{D_m + D_s + 2d}$ |
| $R_1$ | $D_s + d$ | 0 |
| $R_2$ | $\frac{D_m + D_s + 2d}{2}$ | 0 |
| $B_0$ | $\frac{D_s + 2d}{2}$ | $\frac{d\left[\frac{(D_s + d)^2}{4F_m} - F_m\right]}{D_s + d} - \frac{D_s}{2\tan(\theta_E)}$ |

Equations from (3.1) to (3.8) and from (5.1) to (5.2) are valid for Double Offset Ring Focus Cassegrain reflector. However, we need to find the expression of $\hat{n}_s$. $\hat{n}_s$ can be calculated by using equation (5.1) to (5.2). The parameters of $a$ and $b$ in equation (5.2) can be expressed in terms of four parameters $(D_m, F_m, D_s, \theta_E)$ for Double Offset Ring Focus Cassegrain reflector.

$$
\begin{aligned}
a &= \frac{\left(|B_0P_1| - \sqrt{\left(P_{1\rho_m}\right)^2 + \left(P_{1z_m}\right)^2}\right)}{2} \\
b &= \sqrt{\frac{\left(B_{0\rho_m}\right)^2 + \left(B_{0z_m}\right)^2}{4} - a^2}
\end{aligned}
\qquad (6.1)
$$

The expression of $\hat{n}_s$ is the same with the expression in Single Double Offset Ring Focus Cassegrain reflector, but the parameter values of these two expressions are different from each other. The new parameter values can be obtained by Table 6.1 and equation (6.1). Once $\hat{n}_s$ is obtained, the field reflected from the main reflector can be found by using equation (3.1) and (3.2). Then, the radiated fields are obtained by putting these into equations (2.11) and (2.12) as in previous sections.

The analyzed radiation pattern of the Double Offset Ring Focus Cassegrain reflector, which is obtained by using Aperture-Field Method, and the simulated radiation pattern of the Double Offset Ring Focus Cassegrain reflector, which is obtained by using electromagnetic simulation tool CST Microwave Studio, are compared with each other in order to show how analyzed result is close to real reflector pattern. In this comparison, WR90 open ended waveguide feed (which operates in 8.2-12.4 GHz) is used as the feed antenna. The field incident from the feed antenna must be known in order to achieve the radiation fields of reflectors in Aperture-Field Method. For this aim, equation (3.24) is used to get the field incident from WR90. The chosen parameters of the Double Offset Ring Focus Cassegrain reflector used in this comparison are listed in Table 6.2.

Table 6.2. Chosen Parameters of DORF Cassegrain Reflector

| Parameter Name | Parameter Value |
|---|---|
| Main reflector diameter ($D_m$) | 600 mm |
| Main reflector focal length ($F_m$) | 300 mm |
| Sub-reflector diameter ($D_s$) | 100 mm |
| Sub-reflector subtended angle ($\theta_E$) | 20° |
| Operating frequency ($f$) | 10 GHz |

The comparison result is shown in Figure 6.3.

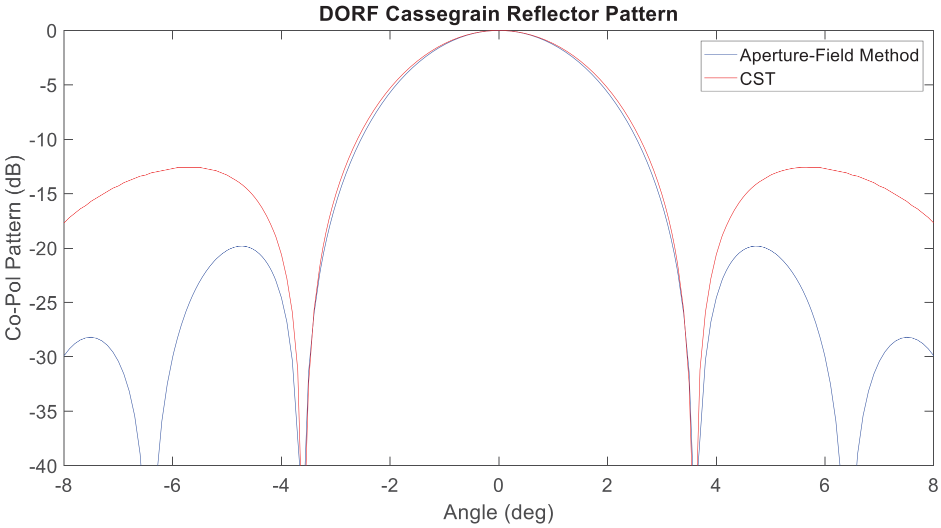

Figure 6.3. Results of Aperture-Field Method and CST Microwave Studio for DORF Cassegrain Reflector

The result given in Figure 6.3 indicate that the results of Aperture-Field Method and CST Microwave Studio are quite similar in the main beam of DORF Cassegrain reflector like in previous chapters, but they are different from each other outside the main beam. As mentioned in previous chapters, diffraction is the main cause of this discrepancy. Due to the diffraction, the null filling and side lobe level cannot be calculated accurately. On the other hand, Aperture-Field Method is very successful to calculate the 3dB beamwidth and position of nulls. For instance, the 3dB beamwidth obtained by Aperture-Field Method is 2.98° and the 3dB beamwidth obtained by CST Microwave Studio is 3.08°.

### 6.2. Double Offset Ring Focus Gregorian Reflector

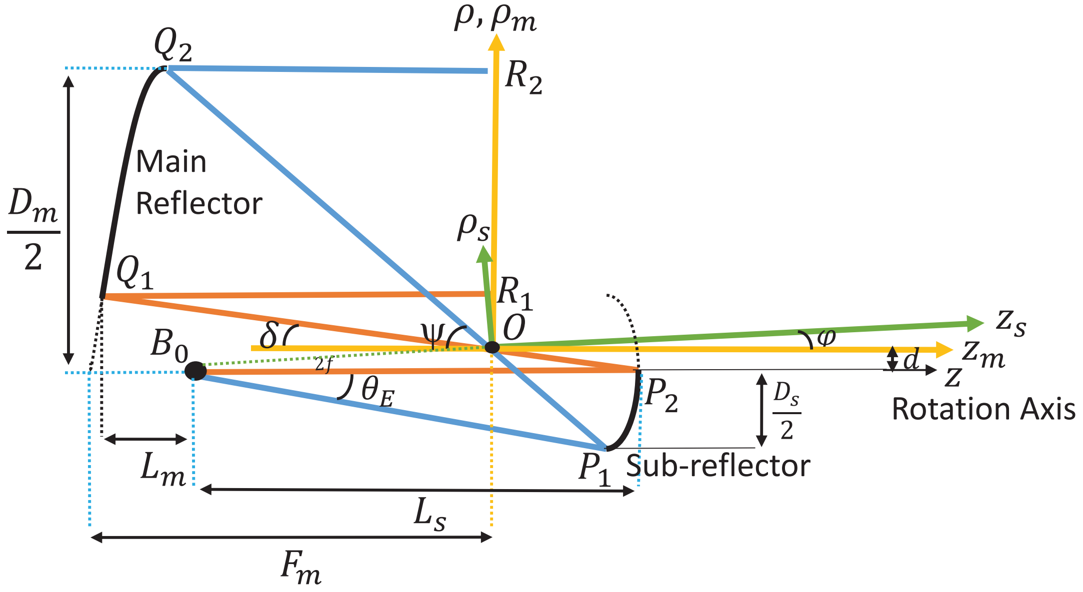

Figure 6.4. Geometry of Double Offset Ring Focus Gregorian Reflector

The geometry of Double Offset Ring Focus Gregorian antenna is shown in Figure 6.4, which shows a cross-section of the antenna. The 3D figure can be obtained by rotating the structure about the $z$ axis (Rotation axis) indicated in the figure. The black solid curve between $Q_1$ and $Q_2$ is the truncated parabolic main reflector with its focus at $O$, and the black solid curve between $P_1$and $P_2$ is the displaced-axis elliptic sub-reflector with one focus at $O$ and the other at $B_0$. The feed is located at this focus $B_0$ of the sub-reflector. We use cylindrical coordinates to describe the main and sub-reflectors, denoted, respectively, by $\rho_m$, $z_m$ and $\rho_s$, $z_s$, both having their origins at $O$. Note that the sub-reflector coordinate system is rotated with respect to main reflector system by an angle $\varphi$. $O$ is the common focus of the two reflectors and is displaced by a distance "$d$" from the rotation axis. When the curves $Q_1Q_2$ and $P_1P_2$ are rotated about the $z$ axis, we obtain the figure of revolution shown in Figure 6.5. Since $O$ is displaced from the rotation axis, the common focal point traces a circle under this rotation and hence the name ring focus. Propagation paths of two rays that go through the edges of the reflectors are also shown in Figure 6.4 by the blue and red solid lines. All other ray paths lie between these two paths.

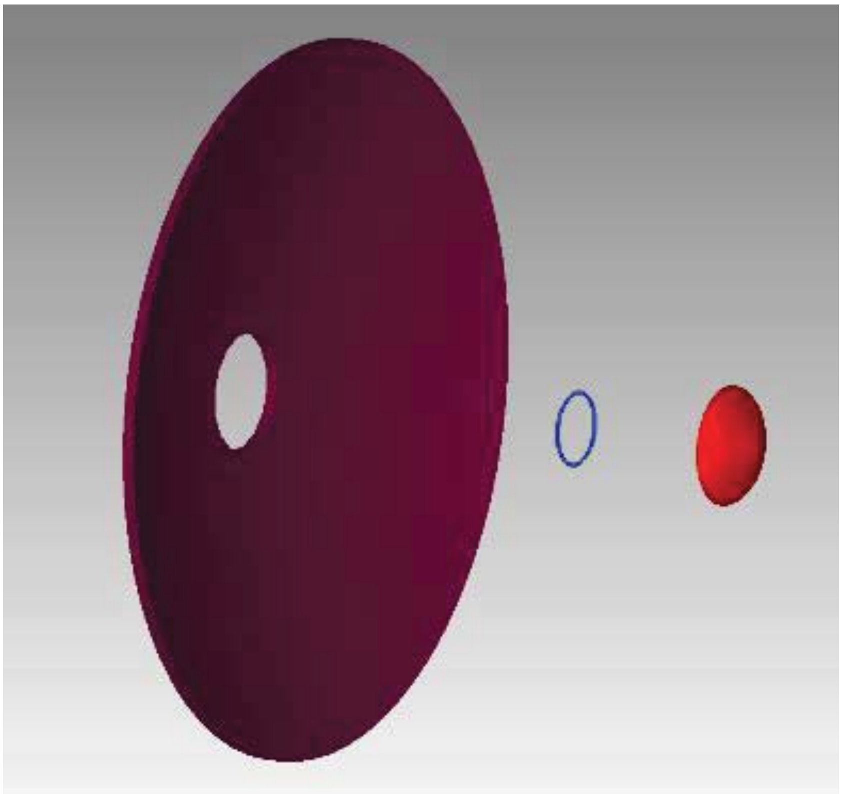

Figure 6.5. Three Dimensional Appearance of DORF Gregorian Reflector

In Figure 6.5, purple, red and blue shapes represent the three dimensional appearance of the truncated parabolic main reflector, displaced-axis elliptic sub-reflector and ring focus, respectively. As shown in this figure, the focus is annular and there is a hole in the main reflector.

As in all ring focus dual reflectors, only four parameters $(D_m, F_m, D_s, \theta_E)$ are enough to describe the full geometry of Double Offset Ring Focus Gregorian reflector and the other parameters can be expressed in terms of these four parameters. The descriptions of all parameters are listed in Table 5.1.

The coordinates of the parameters in Figure 6.4 are presented in Table 6.3 (Granet, 1999).

Table 6.3. Coordinates of DORF Gregorian Parameters

| Point | $y_m$ | $z_m$ |
|---|---|---|
| $Q_1$ | $\frac{D_s - 2d}{2}$ | $\frac{(D_s - 2d)^2}{16F_m} - F_m$ |
| $Q_2$ | $\frac{D_m - 2d}{2}$ | $\frac{(D_m - 2d)^2}{16F_m} - F_m$ |
| $P_1$ | $\frac{-D_s - 2d}{2}$ | $\frac{(-D_s - 2d)\left[\frac{(D_m - 2d)^2}{16F_m} - F_m\right]}{(D_m - 2d)}$ |
| $P_2$ | $-d$ | $\frac{2d\left[\frac{(D_s - 2d)^2}{16F_m} - F_m\right]}{(D_s - 2d)}$ |
| $R_1$ | $\frac{D_s - 2d}{2}$ | 0 |
| $R_2$ | $\frac{D_m - 2d}{2}$ | 0 |

Equations from (3.1) to (3.8), and (5.1) and (5.9) are valid for Double Offset Ring Focus Gregorian reflector. However, we need to find the expression of $\hat{n}_s$. $\hat{n}_s$ can be calculated by using equation (5.1) and (5.9). The parameters of $a$ and $b$ in equation (5.9) can be expressed in terms of four parameters $(D_m, F_m, D_s, \theta_E)$ for Double Offset Ring Focus Gregorian reflector.

$$\begin{gathered} a = \frac{\left(|B_0P_1| + \sqrt{\left(P_{1\rho_m}\right)^2 + \left(P_{1z_m}\right)^2}\right)}{2} \\ b = \sqrt{\frac{\left(B_{0\rho_m}\right)^2 + \left(B_{0z_m}\right)^2}{4} + a^2} \end{gathered} \tag{6.2}$$

The expression of $\hat{n}_s$ is the same with the expression in Single Double Offset Ring Focus Cassegrain reflector, but the parameter values of these two expressions are different from each other. The new parameter values can be obtained by Table 6.3 and equation (6.2). Once $\hat{n}_s$ is obtained, the field reflected from the main reflector can be found by using equation (3.1) and (3.2). Then, the radiated fields are obtained by putting these into equations (2.11) and (2.12) as in previous sections.

The analyzed radiation pattern of the Double Offset Ring Focus Gregorian reflector, which is obtained by using Aperture-Field Method, and the simulated radiation pattern of the Double Offset Ring Focus Gregorian reflector, which is obtained by using electromagnetic simulation tool CST Microwave Studio, are compared with each other in order to show how analyzed result is close to real reflector pattern. In this comparison, WR90 open ended waveguide feed (which operates in 8.2-12.4 GHz) is used as the feed antenna. The field incident from the feed antenna must be known in order to achieve the radiation fields of reflectors in Aperture-Field Method. For this aim, equation (3.24) is used to get the field incident from WR90. The chosen parameters of the Double Offset Ring Focus Gregorian reflector used in this comparison are listed in Table 6.4.

Table 6.4. Chosen Parameters of DORF Gregorian Reflector

| Parameter Name | Parameter Value |
|---|---|
| Main reflector diameter ($D_m$) | 600 mm |
| Main reflector focal length ($F_m$) | 300 mm |
| Sub-reflector diameter ($D_s$) | 100 mm |
| Sub-reflector subtended angle ($\theta_E$) | 20° |
| Operating frequency ($f$) | 10 GHz |

The comparison result is shown in Figure 6.6.

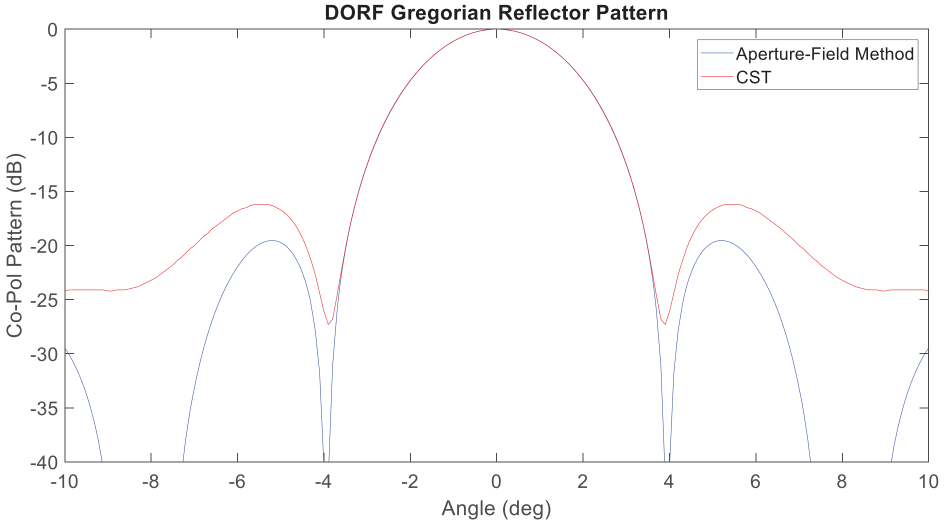

Figure 6.6. Results of Aperture-Field Method and CST Microwave Studio for DORF Gregorian Reflector

From the comparison of the patterns given in Figure 6.6, it might be seen that the result of Aperture-Field Method is similar to the result of CST Microwave Studio in the main beam of DORF Gregorian reflector. The 3dB beamwidth obtained by Aperture-Field Method is 3.20° while the 3dB beamwidth obtained by CST Microwave Studio is 3.24°. The differences between these two radiation patterns result from the diffraction as mentioned in previous chapters. Aperture-Field Method is quite successful in the main beam and the positions of the nulls, and also peaks of the side lobes can be obtained with some accuracy. However, Aperture-Field Method is not very successful in predicting the null and side lobe levels.

# CHAPTER 7

# COMPARISON OF SAME KIND DUAL REFLECTORS

Classical, SORF and DORF types of the Cassegrain and Gregorian reflectors are compared with each other in this chapter to demonstrate the advantages and disadvantages of ring focus dual reflectors.

The first comparison is made for Cassegrain type reflectors. For this aim, classical, SORF and DORF Cassegrain reflectors which are fed with the same feed antenna (WR90 waveguide) are compared with each other. The chosen parameters of Cassegrain type reflectors are presented in Table 7.1.

Table 7.1. Chosen Parameters of Cassegrain Type Reflectors

| Reflector Type | Main Reflector Diameter ($D_m$) | Main Reflector Focal Length ($F_m$) | Sub-reflector Diameter ($D_s$) | $\theta_E$ |
|---|---|---|---|---|
| Cassegrain | 600 mm | 300 mm | 100 mm | - |
| SORF Cassegrain | 600 mm | 300 mm | 100 mm | 50° |
| DORF Cassegrain | 600 mm | 300 mm | 100 mm | 50° |

The radiation patterns of Cassegrain type reflectors are shown in Figure 7.1.

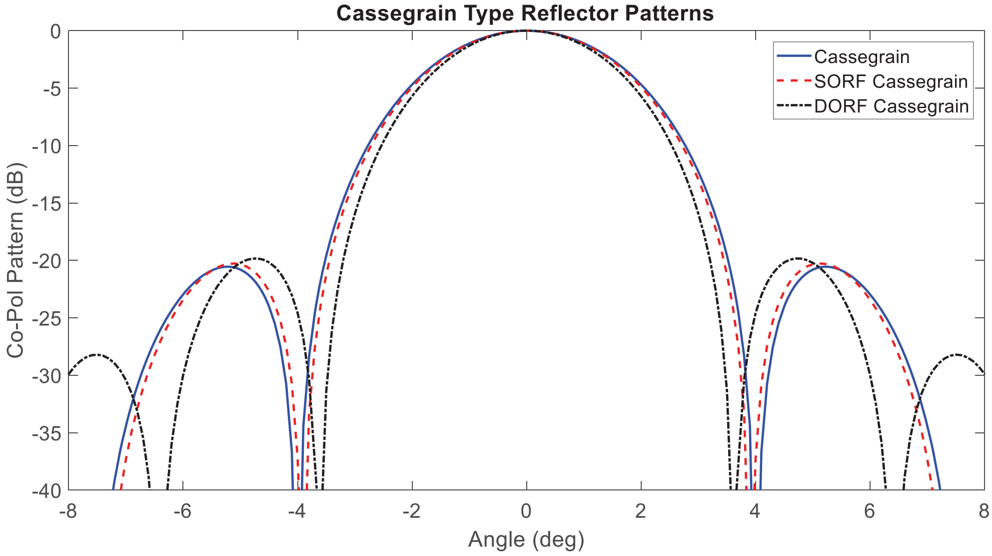

Figure 7.1. Comparison of Cassegrain Type Reflectors

From Figure 7.1, it can be seen that SORF and DORF Cassegrain reflectors provide narrower beamwidth than classical Cassegrain reflector. Narrower beamwidth means that efficiency and directivity of the reflector is high. Therefore, it can be understood that efficiency and directivity of SORF and DORF Cassegrain reflectors are higher than classical Cassegrain reflector. This advantage is also mentioned by Ivashina et al. (Ivashina, et al., 2011). The reason of this advantage is that the aperture field strengths of the SORF and DORF Cassegrain reflectors is closer to uniform field as compared to the aperture field strength of the classical Cassegrain reflector for the same reflector sizes. Uniform field strength on the aperture provides more directive beam and also cause the higher field strength at the edge of the reflector. Due to the higher field strength at the edge of the reflector, the side lobe level of the reflector becomes higher. The aperture field strengths of the Cassegrain type reflectors in Table 7.1 are given in Figure 7.2, Figure 7.3 and Figure 7.4.

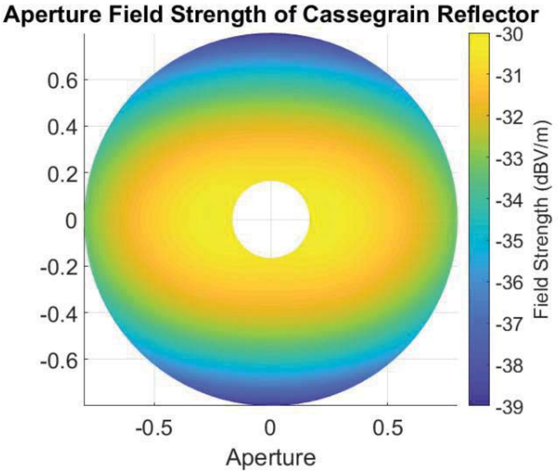

Figure 7.2. Aperture Field Strength of Cassegrain Reflector

The aperture field strength of the classical Cassegrain reflector in Table 7.1 changes between -30dB and -39 dB.

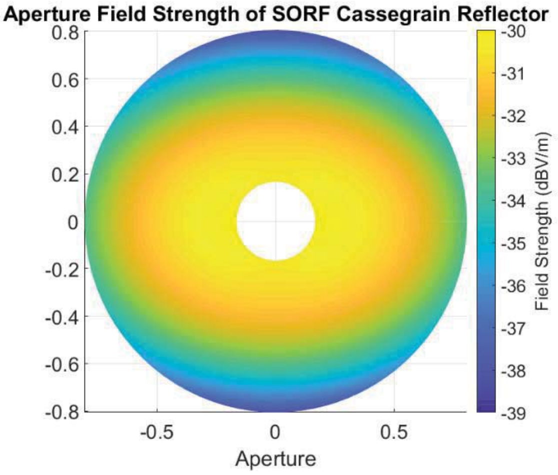

Figure 7.3. Aperture Field Strength of SORF Cassegrain Reflector

The aperture field strength of the SORF Cassegrain reflector in Table 7.1 changes between -30dB and -38 dB.

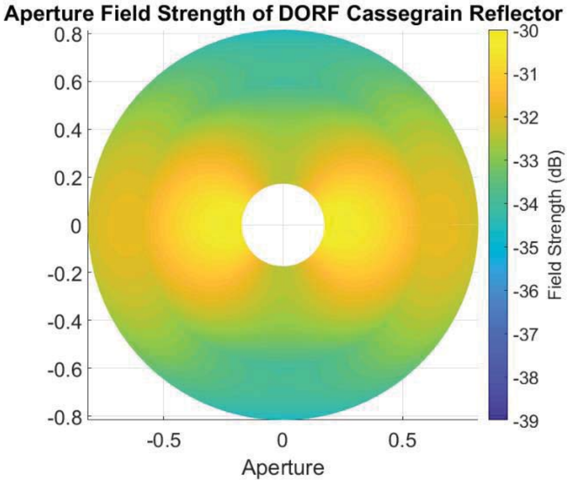

Figure 7.4. Aperture Field Strength of DORF Cassegrain Reflector

The aperture field strength of the DORF Cassegrain reflector in Table 7.1 changes between -30dB and -35 dB.

From Figure 7.2, Figure 7.3 and Figure 7.4, it can be seen that the aperture field strength distribution of the DORF Cassegrain reflector is closer to uniform as compared to that of the SORF Cassegrain reflector and the classical Cassegrain reflector. Thus, the beamwidth of the DORF Cassegrain reflector is the narrowest among them. Also, the field strength at the edge of the reflector is highest in the DORF Cassegrain reflector. This increases the side lobe level of the DORF Cassegrain reflector. Besides, the field strength of the SORF Cassegrain reflector is closer to uniform as compared the field strength of the classical Cassegrain reflector. Thus, the beamwidth of the SORF Cassegrain reflector is narrower than the beamwidth of the classical Cassegrain reflector. As a trade-off, the field strength at the edge of the SORF Cassegrain reflector is higher than the field strength at the edge of the classical Cassegrain reflector; thus, the side lobe level of the SORF Cassegrain reflector is higher than the side lobe level of the classical Cassegrain reflector.

The second comparison is made for Gregorian type reflectors. For this purpose, classical, SORF and DORF Gregorian reflectors which are fed with the same feed antenna (WR90 waveguide) are compared with each other. The chosen parameters of different type Gregorian reflectors are presented in Table 7.2.

Table 7.2. Chosen Parameters of Gregorian Type Reflectors

| Reflector Type | Main Reflector Diameter ($D_m$) | Main Reflector Focal Length ($F_m$) | Sub-reflector Diameter ($D_s$) | $\theta_E$ |
|---|---|---|---|---|
| Gregorian | 600 mm | 300 mm | 100 mm | - |
| SORF Gregorian | 600 mm | 300 mm | 100 mm | 50° |
| DORF Gregorian | 600 mm | 300 mm | 100 mm | 50° |

The radiation patterns of Gregorian type reflectors are shown in Figure 7.5.

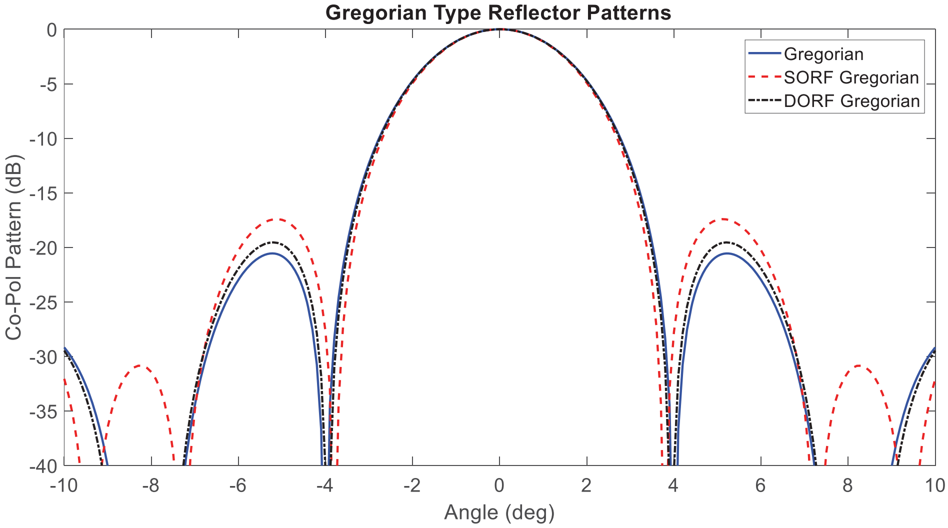

Figure 7.5. Comparison of Gregorian Type Reflectors

From Figure 7.5, it can be seen that SORF and DORF Gregorian reflectors provide narrower beamwidth than classical Gregorian reflector. Narrower beamwidth means that aperture efficiency and directivity of the reflector is high. Therefore, it can be understood that efficiency and directivity of SORF and DORF Gregorian reflectors are higher than classical Gregorian reflector. The reason of this advantage is that the aperture field strengths of the SORF and DORF Gregorian reflectors are closer to uniform field as compared to the aperture field strength of the classical Gregorian reflector for the same reflector sizes. Uniform field strength on the aperture provides more directive beam and also cause higher field strength at the edge of the reflector. Due to the increased field strength at the edge of the reflector, the side lobe level of the reflector becomes higher. The field strengths of the Gregorian type reflectors in Table 7.2 are given in Figure 7.6, Figure 7.7 and Figure 7.8.

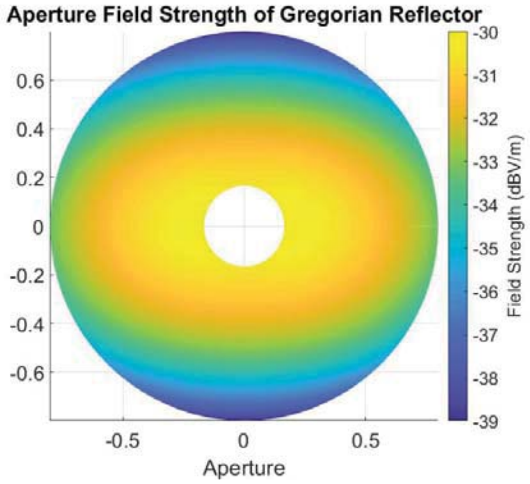

Figure 7.6. Aperture Field Strength of Classical Gregorian Reflector

The aperture field strength of the classical Gregorian reflector in Table 7.2 changes between -30dB and -39 dB.

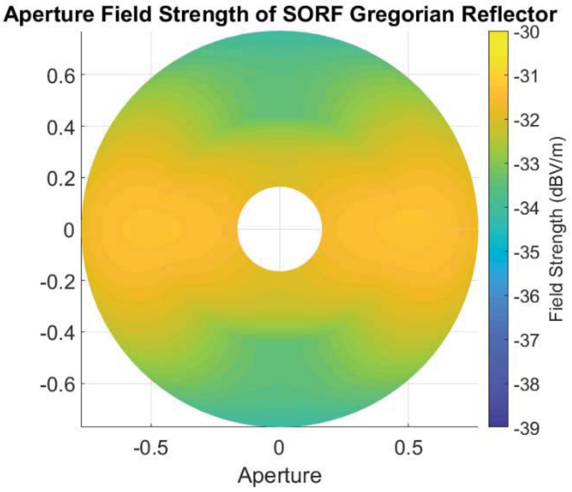

Figure 7.7. Aperture Field Strength of SORF Gregorian Reflector

The aperture field strength of the SORF Gregorian reflector in Table 7.2 changes between -31dB and -34 dB.

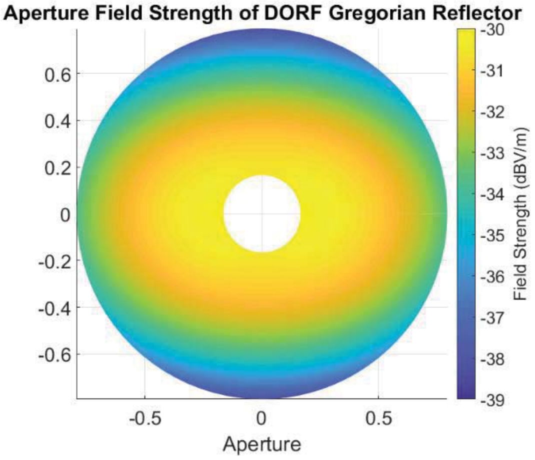

Figure 7.8. Aperture Field Strength of DORF Gregorian Reflector

The aperture field strength of the DORF Gregorian reflector in Table 7.2 changes between -30dB and -38 dB.

From the results in Figure 7.6, Figure 7.7 and Figure 7.8, it can be seen that the field strength of the SORF Gregorian reflector is closer to uniform field as compared to the field strengths of the DORF Gregorian reflector and the classical Gregorian reflector. Thus, the beamwidth of the SORF Gregorian reflector is the narrowest among them. Also, the field strength at the edge of the reflector is highest in the SORF Gregorian reflector. This is the reason that the side lobe level of the SORF Gregorian reflector is the highest. Besides, the field strength of the DORF Gregorian reflector is closer to uniform as compared to the field strength of the classical Gregorian reflector. Thus, the beamwidth of the DORF Gregorian reflector is narrower than the beamwidth of the classical Gregorian reflector. As a trade-off, the field strength at the edge of the DORF Gregorian reflector is higher than the field strength at the edge of the classical Gregorian reflector; thus, the side lobe level of the DORF Gregorian reflector is higher than the side lobe level of the classical Gregorian reflector.

From the results in Figure 7.4 and Figure 7.7, the field strength of the SORF Gregorian reflector is closer to uniform as compared to the field strength of the DORF Cassegrain reflector. Thus, the beamwidth of the SORF Gregorian reflector is narrower than the beamwidth of the DORF Cassegrain reflector. Thus, the beamwidth of the SORF Gregorian reflector is the narrowest among all ring focus reflectors.

As a result of these advantages of SORF and DORF reflectors, they may be used to obtain a smaller reflector size for a specified beamwidth. This feature of ring focus reflectors are very useful in the applications which have limited volume for antenna. In addition to advantages of SORF and DORF reflectors, they cause higher side lobe levels than classical types as a disadvantage. This disadvantage may become important in the applications which require low side lobe level such as direction finding etc.

# CHAPTER 8

# DESINGS OF RING FOCUS REFLECTORS

In this chapter, designs of the ring focus reflectors are carried out. As a design limit, maximum reflector diameter and $f/D$ ratio of the main reflector are assumed to be 2.4m and 0.5 respectively. Also, operation frequency is chosen as 10 GHz and an aperture efficiency above 70% are aimed for the ring focus reflectors as the design requirement.

A horn antenna, with parameters given in Table 8.1 in accordance with Figure 3.11 and Figure 3.12, is preferred as the feed of the reflectors since its E-plane and H-plane patterns are almost equal with each other for the angles smaller than the subtended angle of the sub-reflector ($\theta_E$) and its design is simple.

Table 8.1. Chosen Parameters of Horn Antenna

| Parameter Name | Parameter Value |
|---|---|
| Long length of the horn aperture ($A$) | 50 mm |
| Short length of the horn aperture ($B$) | 35 mm |
| Operating Frequency ($f$) | 10 GHz |
| $\Delta_a$ | 10.0 mm |
| $\Delta_b$ | 4.5 mm |

The E-plane and H-plane patterns of the horn antenna is given in Figure 8.1.

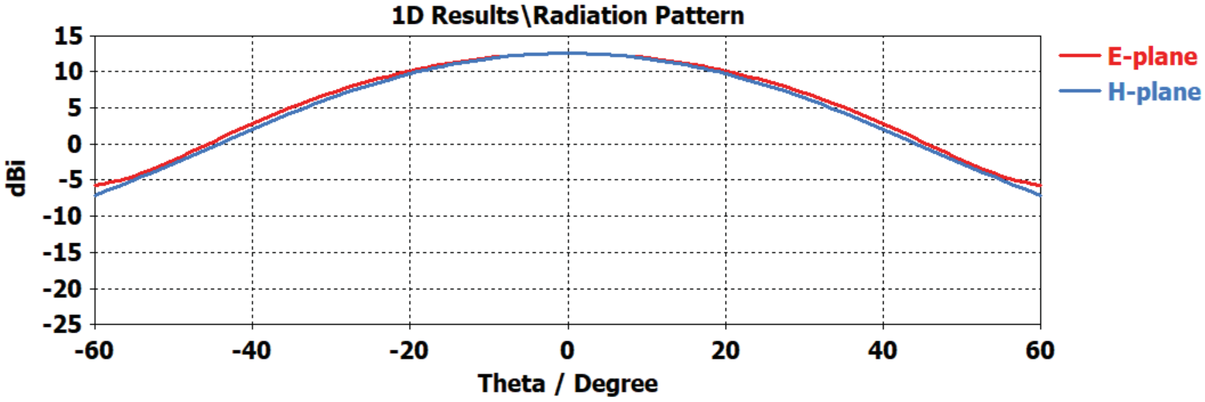

Figure 8.1. Radiation Pattern of Horn Antenna

Feed taper is the ratio of the power at the subtended angle of the radiation pattern and the power at the boresight angle of the radiation pattern. Prata et al. indicate that optimum efficiency for the reflector is achieved when feed taper equals to approximately -11 dB (Prata, Moreira, & Amaro, 2003). Thus, this value of the feed taper is considered in the designs of the ring focus reflectors in this chapter. The feed taper of -11dB for this horn antenna means that $\theta_E$ approximately equals to 42.5°. Thus, $\theta_E$ is taken as 42.5° for all simulations in this chapter.

### 8.1. Single Offset Ring Focus Dual Reflector Design

In this section, designs of single offset ring focus dual reflectors are carried out. In order to take into account all lossy effects such as multi-reflection, diffraction etc., the designs are made in CST Microwave Studio which is a full-wave simulator. In addition to the result of CST Microwave Studio, the result of Aperture-Field method is also given.

### 8.1.1. Single Offset Ring Focus Cassegrain Reflector Design

To find an optimum $D_s/D_m$ ratio for Single Offset Ring Focus Cassegrain reflector, which is the ratio of the diameters of the hyperboloidal sub-reflector and the paraboloidal main reflector, a parameter sweep is performed in CST Microwave Studio. This sweep is performed in CST Microwave Studio, since it takes into account all lossy effects, for example the aperture blockage resulted from the feed, and these effects may decrease the aperture efficiency of the reflector. The result of the parameter sweep is given in Figure 8.2.

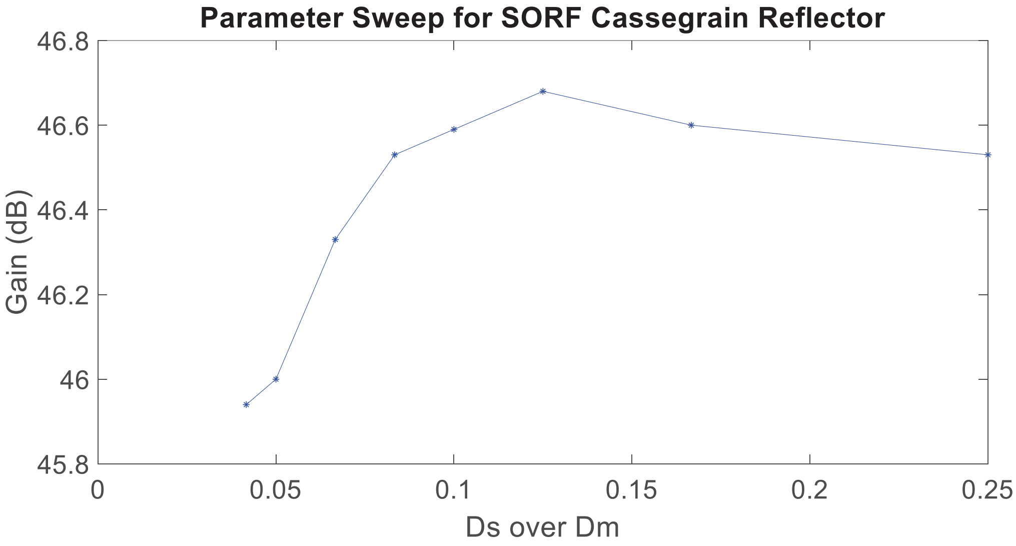

Figure 8.2. Parameter Sweep for SORF Cassegrain Reflector

From the result in Figure 8.2, it can be seen that the efficiency of the SORF Cassegrain reflector is best when $D_s \approx D_m/8$. Thus, this $D_s/D_m$ ratio is used for the design. The simulated result is given in Figure 8.3 together with the result of Aperture-Field method.

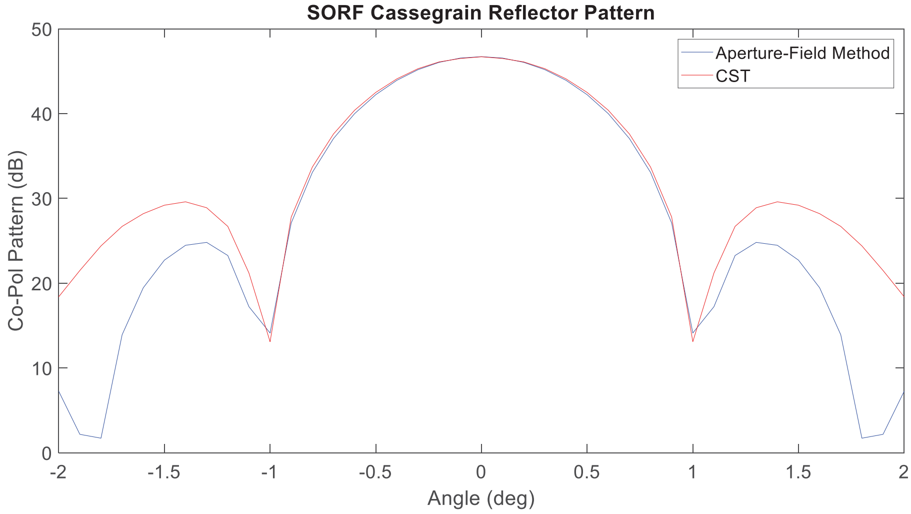

Figure 8.3. Designed Patterns of SORF Cassegrain Reflector

From the results given in Figure 8.3, the designed SORF Cassegrain reflector has a gain of 46.68 dB and an aperture efficiency of 74%. Thus, the design goal is achieved. Also, the result obtained by Aperture-Field Method in this section is closer to the result obtained by CST Microwave Studio when compared to the results in section 5.1. The reason of this situation is that electrically larger reflector size increases the accuracy of Aperture-Field Method and chosen reflector size in this section is electrically larger than the chosen reflector size in section 5.1.

The process time required for Aperture-Field Method takes about 5 minutes while the process time required for CST Microwave Studio takes approximately 1 day. This is the main advantage of the analysis tool considered in this thesis.

### 8.1.2. Single Offset Ring Focus Gregorian Reflector Design

To find an optimum $D_s/D_m$ ratio for Single Offset Ring Focus Gregorian reflector, which is the ratio of the diameters of the ellipsoidal sub-reflector and the paraboloidal main reflector, a parameter sweep are performed in CST Microwave Studio. This sweep is performed in CST Microwave Studio, since it takes into account all lossy effects, for example the aperture blockage resulted from the feed, and these effects may decrease the aperture efficiency of the reflector. The result of the parameter sweep is given in Figure 8.4.

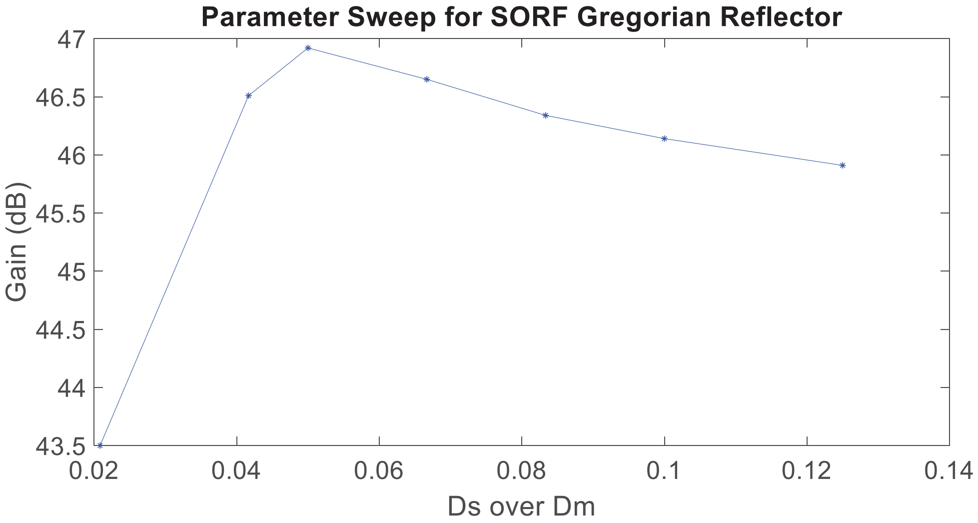

Figure 8.4. Parameter Sweep for SORF Gregorian Reflector

From the result in Figure 8.4, it can be seen that the efficiency of the SORF Gregorian reflector is best when $D_s \approx D_m/20$. Thus, this $D_s/D_m$ ratio is used for the design. The simulated result is given in Figure 8.5 together with the result of Aperture-Field method.

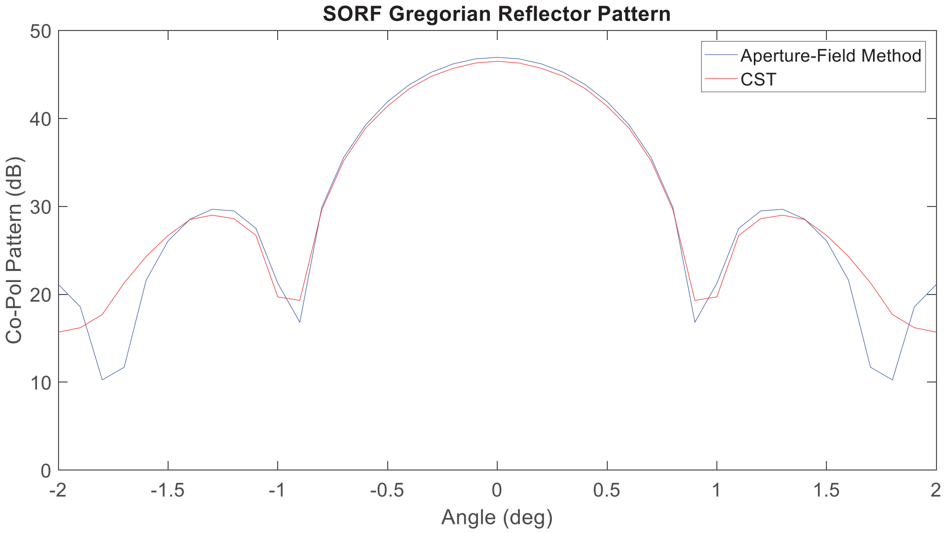

Figure 8.5. Designed Patterns of SORF Gregorian Reflector

From the results given in Figure 8.5, the designed SORF Gregorian reflector has a gain of 46.92 dB and an aperture efficiency of 78%. Thus, the design goal is achieved. Besides, the result obtained by Aperture-Field Method in this section is more similar to the result obtained by CST Microwave Studio as compared with the results in section 5.2 due to the chosen reflector sizes.

The process time required for Aperture-Field Method takes much less time than the process time required for CST Microwave Studio as remarked in section 8.1.1.

## 8.2. Double Offset Ring Focus Reflector Design

In this section, designs of single offset ring focus dual reflectors are carried out. In order to take into account all lossy effects such as multi-reflection, diffraction etc., the designs are made in CST Microwave Studio which is a full-wave simulator. In addition to the result of CST Microwave Studio, the result of Aperture-Field method is also given.

### 8.2.1. Double Offset Ring Focus Cassegrain Reflector Design

To find an optimum $D_s/D_m$ ratio for Double Offset Ring Focus Cassegrain reflector, which is the ratio of the diameters of the hyperboloidal sub-reflector and the paraboloidal main reflector, a parameter sweep are performed in CST Microwave Studio. This sweep is performed in CST Microwave Studio, since it takes into account all lossy effects, for example the aperture blockage resulted from the feed, and these effects may decrease the aperture efficiency of the reflector. The result of the parameter sweep is given in Figure 8.6.

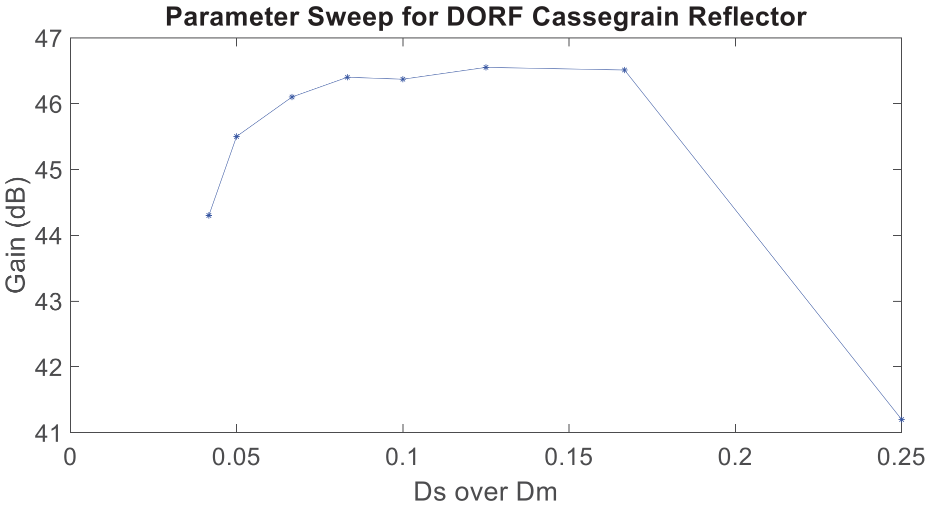

Figure 8.6. Parameter Sweep for DORF Cassegrain Reflector

From the result in Figure 8.6, it can be seen that the efficiency of the DORF Cassegrain reflector is best when $D_s \approx D_m/8$. Thus, this $D_s/D_m$ ratio is used for the design. The simulated result is given in Figure 8.7 together with the result of Aperture-Field method.

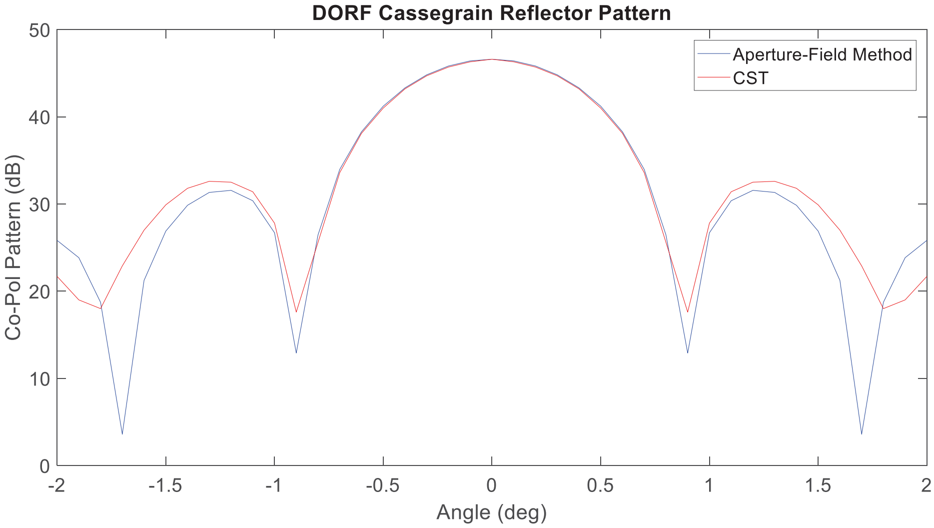

Figure 8.7. Designed Patterns of DORF Cassegrain Reflector

From the results in Figure 8.7, the designed DORF Cassegrain reflector has a gain of 46.55 dB and an aperture efficiency of 72%. Thus, the design goal is achieved.

Furthermore, the similarity between the results obtained by Aperture-Field Method and CST Microwave Studio in this section are more than the similarity between the results obtained by Aperture-Field Method and CST Microwave Studio in section 6.1 because of the chosen reflector sizes.

The process time required for Aperture-Field Method takes much less time than the process time required for CST Microwave Studio as specified in previous sections.

### 8.2.2. Double Offset Ring Focus Gregorian Reflector Design

To find an optimum $D_s/D_m$ ratio for Double Offset Ring Focus Gregorian reflector, which is the ratio of the diameters of the ellipsoidal sub-reflector and the paraboloidal main reflector, a parameter sweep are performed in CST Microwave Studio. This sweep is performed in CST Microwave Studio, since it takes into account all lossy effects, for example the aperture blockage resulted from the feed, and these effects may decrease the aperture efficiency of the reflector. The result of the parameter sweep is given in Figure 8.8.

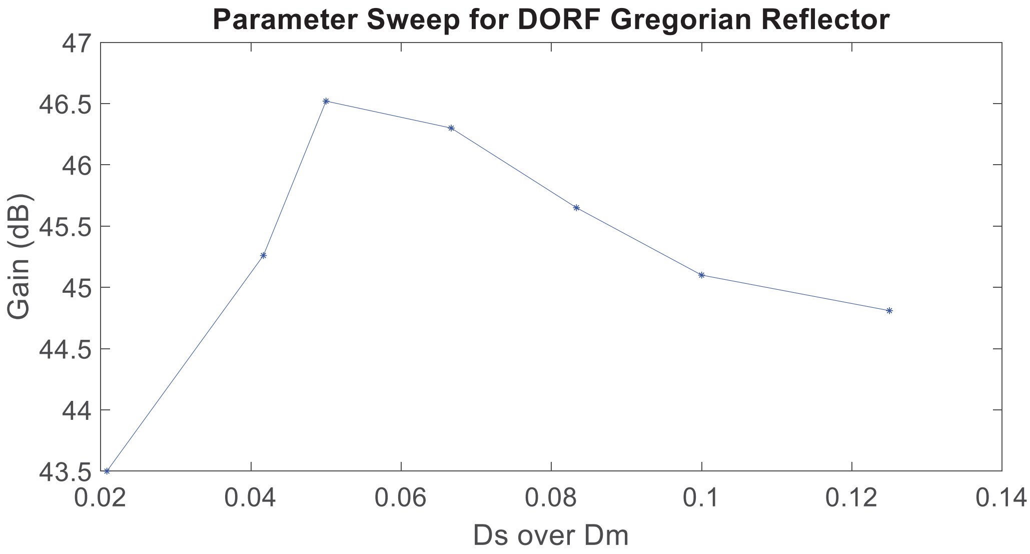

Figure 8.8. Parameter Sweep for DORF Gregorian Reflector

From the result in Figure 8.6, it can be seen that the efficiency of the DORF Gregorian reflector is best when $D_s \approx D_m/20$. Thus, this $D_s/D_m$ ratio is used for the design. The simulated result is given in Figure 8.9 together with the result of Aperture-Field method.

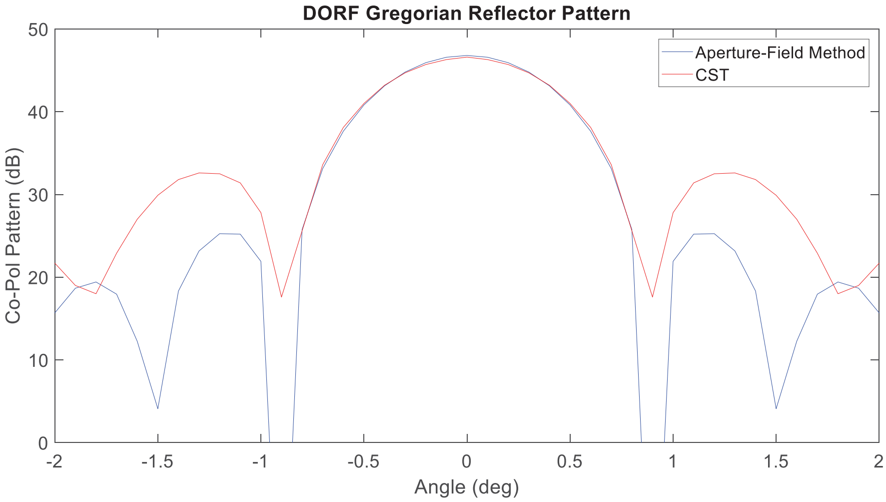

Figure 8.9. Designed Patterns of DORF Gregorian Reflector

From the results in Figure 8.9, the designed DORF Gregorian reflector has a gain of 46.52 dB and an aperture efficiency of 71%. Thus, the design goal is achieved. Also, the chosen reflector size in this section provides the result obtained by Aperture-Field Method to be closer to the result obtained by CST Microwave Studio when compared with the results in section 6.2.

The process time required for Aperture-Field Method is much less than the process time required for CST Microwave Studio as indicated in previous sections.

# CHAPTER 9

# CONCLUSION

Ring focus reflectors are the main subject of this thesis. In this thesis, radiation characteristics of the ring focus reflectors have been aimed to calculate and the differences which are resulted from the usage of the ring focus architecture are desired to learn. In terms of these purposes, firstly the methods used for the calculation of the reflector patterns are investigated. And then, a proper method, Aperture-Field method, is chosen to obtain the radiation patterns of the reflectors and the radiation patterns of the reflectors are analyzed for each type of reflectors by using Aperture-Field method. To learn the suitability of the analyzed results to real world, the analyzed patterns which are obtained by Aperture-Field method and the simulated patterns which are obtained by CST Microwave Studio that uses the numerical electromagnetic methods to calculate the radiation patterns of the antennas is investigated. Besides, radiation patterns of classical dual and ring focus dual reflectors are compared with each other. As a result of these comparisons, it is seen that ring focus dual reflectors have some advantages and disadvantages according to classical dual reflectors. The first and main advantage of ring focus reflectors is that the beamwidth of ring focus reflectors is narrower than classical dual reflectors for a specified main reflector diameter. Narrower beamwidth for a specified main reflector diameter means that efficiency and directivity is higher; therefore, the directivities of ring focus dual reflectors are higher than the directivities of classical dual reflectors. Another advantage of ring focus reflectors is that the total size in ring focus dual reflectors is smaller than classical dual reflectors. Geometrical properties of ring focus dual reflectors allow to place the feed closer enough to the sub-reflector without any aperture blockage. Therefore, total size of the reflector system is smaller in ring focus dual reflectors as compared to classical dual reflectors. This feature of the ring focus dual reflectors makes them a good option in compact antenna applications. On the other hand, the disadvantage of ring focus dual reflectors is that ring focus dual reflectors cause increased side lobe level as a trade-off between narrow beamwidth and increased side lobe level. Thus, usage of ring focus architecture may not be reasonable in the applications in which side lobe level is crucial.

In the direction of above information about the ring focus dual reflectors, the main differences in the radiation pattern which exist as a result of usage of ring focus dual reflectors are expressed, and the advantages and disadvantages of ring focus dual reflectors are indicated. Consequently, the purposes of this thesis mentioned in Chapter 1 are carried out. Also, the following future works may contribute this thesis and they may make the methods applied in this thesis more accurate.

## 9.1. Future Works

In this thesis, some assumptions are made when choosing analysis method (Aperture-Field Method) to calculate the radiation patterns of reflectors. The main assumption made in thesis is related to that the reflectors which are analyzed in this thesis are electrically large, and it means that this method may give inaccurate results in electrically small reflectors. Also, diffraction effects are not taken into account in this thesis. This situation may cause wrong results at the far angles of reflector pattern. Therefore, following works may be purposed to make a more convenient analysis tool.

- A supporting method may be applied to analysis tool in order to analyze the electrically small reflectors.
- The methods which are used to calculate diffraction may be added to analysis tool.

Besides, following works may be done in order to develop the analysis tool.

- A program which can calculate the optimum feed for the desired reflector pattern may be improved.
- Other types of reflectors may be added to analysis tool.

# REFERENCES

Baars, J. W. (2007). *The Paraboloidal Reflector Antenna in Radio Astronomy and Communication.* New York: Spinger Science+Business Media, LLC.

Balanis, C. A. (1989). *Advanced Enginering Electromagnetics.* New York: John Wiley and Sons.

Balanis, C. A. (2005). *Antenna Theory.* New Jersey: John Wiley and Sons.

Bergmann, J. R., & Palma Pereira, L. C. (1998). Shaped Subreflector for Offset Gregorian Reflector Antenna with a Paraboloidal Main Reflector. *IEEE Antennas and Propagation Society International Symposium.* Atlanta, GA, USA.

Bergmann, J., & Moreira, F. (2005). Simple design equations for omnidirectional axis-displaced dual-reflector antennas. *Microwave and Optical Technology Letters*, 159-163.

Bucci, O. M., Pelosi, G., & Selleri, S. (1999). Cassegrain[telescopes]. *IEEE, 41*(3), 7-13.

Cheng, D. K. (1983). *Field and Wave Electromagnetics.* Menlo Park, California: Addison-Wesley Publishing Company, Inc.

Cichon, D. J., & Wiesbeck, W. (1995). The Heinrich Hertz Wireless Experiments at Karlsruhe in the View of Modern Communication. *100 Years of Radio.* Germany.

Davis, P. J., & Rabinowitz, P. (1984). *Methods of Numerical Integration.* London: Elsevier Inc., Academic Press.

Gibson, W. C. (2008). *The Method of Moments in Electromagnetics.* New York: Chapman&Hall/CRC.

Granet, C. (1999). A Simple Procedure for the Design of Classical Displaced-Axis Dual-Reflector Antennas Using a Set of Geometric Parameters. *IEEE Antennas and Propagation Magazine* , 64-72.

Hannan, P. W. (1961). Microwave Antennas Derived from the Cassegrain Telescopes. *IEEE, 9*(2), 140-153.

Ivashina, M. V., Bakker, R., bij de Vaate, J. G., Iupikov, O. A., Arts, M., Dekker, J., & van Ardenne, A. (2011). An Axi-Symmetric Segmented Composite SKA Dish Design: Performance and Production Analysis. *Proceedings of the Asia-Pacific Microwave Conference.* Melbourne, Australia.

Jenn, D. C., Vered, N., & Ordonez, M. (Jan 1993). Small Efficient Axially Symmetric Dual Reflector Antennas. *IEEE Transactions on Antennas and Propagation, 41*(1), 115-117.

Keller, J. (February 1962). Geometrical Theory of Diffraction. *Journal Optical Society of America, 52*(2), 116-130.

Kishk, A. A. ( 2011). *Electromagnetic Waves Propagation In Complex Matter.* Rijeka: InTech.

Leifer, A. C., & Rotman, W. (1986). Grasp: An improved displaced-axis, dual-reflector antenna design for EHF applications. *1986 Antennas and Propagation Society International Symposium* (pp. 507-510). Philadelphia, PA, USA: IEEE.

Lo, Y. T., & Lee, S. W. (1993). *Antenna Handbook.* New York: Van Nostrand Reinhold.

Mahajan, V. N. (2014). *Fundamentals of Geometrical Optics.* Bellingham, Washington, USA: SPIE.

Milligan, T., & Popov, A. (1997). Amplitude aperture-distribution control in displaced-axis two-reflector antennas. *IEEE Antennas and Propagation Magazine*, 58-63.

Mizusawa, M., Urasaki, S., & Tanaka, H. (1977). An Offset Shaped-Reflector Cassegrain Antenna. *Antennas and Propagation Society International Symposium.* Stanford, CA, USA.

Morgan, S. (1964). Some examples of generalized cassegrainian and gregorian antennas. *IEEE Transactions on Antennas and Propagation*, 685-691.

Orfanidis, S. J. (1999). *Electromagnetic Waves and Antennas.* Rutgers University.

Prata, A., Moreira, F. J., & Amaro, L. R. (2003). Displaced-Axis-Ellipse Reflector Antenna for Spacecraft Communications. *Proceedings of the 2003 SBMO/IEEE MTT-S International Microwave and Optoelectronics Conference.* Foz do Iguacu, Brazil.

Press, W. H., Teukolsky, S. A., Vetterling, W. T., & Flannery, B. P. (1997). *Numerical Recipes in C: The Art of Sicentific Computing.* New York: The Press Syndicate of the University of Cambridge.

Rudge, A. W., & Adatia, N. A. (1978). Offset-Parabolic-Reflector Antennas: A Review. *IEEE, 66*(12), 1592 - 1618.

Sandler, S. (1960). Paraboloidal reflector patterns for off-axis feed. *IRE Transactions on Antennas and Propagation* , 368-379.

Sharma, S. K., Rao, S., & Shafai, L. (2013). *Handbook of Reflector Antennas and Feed Systems.* Artech House.

Sommerfeld, A. (1954). *OPTICS.* New York: Academic Press Inc.

Zhi-yong, L. (2010). A efficient ring-focus antenna for forming an elliptic beam. *2010 International Conference on Microwave and Millimeter Wave Technology* (s. 1880-1882). Chengdu, China: IEEE.

# APPENDICES

## A. Trapezoidal Rule

Trapezoidal rule is one of the simplest techniques for numerical integration. To understand this rule, firstly consider an integral shown in Figure 0.1.

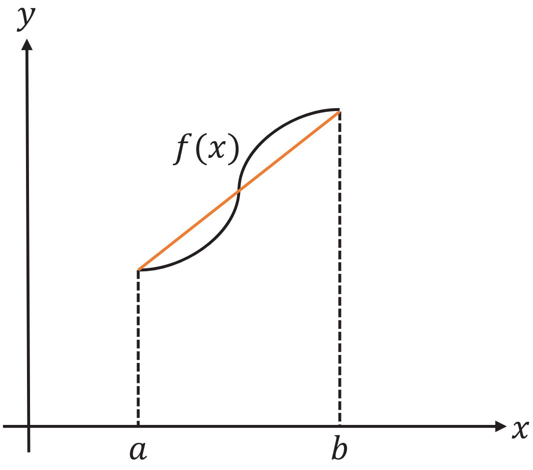

Figure 0.1. Sample Integral for Trapezoidal Rule

Trapezoidal rule states that the area under curve is approximately equals to the area of trapezoid which occurs from the corner points of this curve. Therefore, equation (0.1) is obtained.

$$\int_a^b f(x)dx \approx (b-a)\left[\frac{f(a)+f(b)}{2}\right] \qquad (0.1)$$

The required integral is divided to small enough intervals, and the integrals are calculated by using equation (0.1) on each interval. Superposition of these integrals on each interval gives the result of required integral.

## B. Gauss-Legendre Quadrature Method

Consider the integral of $f(x)$ in equation (0.1). To integrate this identity by using Gauss-Legendre Quadrature method, firstly approximate $f(x)$ over interval of $[-1,1]$. After that, $f(x)$ is written in terms of nodes ($x_i$) and weights ($w_i$).

$$\int_{-1}^{1} f(x)d_x \approx \sum_{i=1}^{n} w_i f(x_i) \tag{0.2}$$

The $n$ computation points $x_i$ are the roots of n-th order Legendre Polynomials $P_n(x)$. Legendre Polynomials are defined in equation (0.3).

$$\begin{gathered} P_0(x) = 1 \\ P_1(x) = x \\ nP_n(x) = (2n-1)xP_{n-1}(x) - (n-1)P_{n-2}(x) \end{gathered} \tag{0.3}$$

Derivative of Legendre Polynomials is given in equation (0.4).

$$P'_n(x) = \frac{n}{x^2-1}\left(xP_n(x) - P_{n-1}(x)\right) \tag{0.4}$$

The roots of those polynomials are not analytically solvable. By using Newton-Raphson iteration (Press, Teukolsky, Vetterling, & Flannery, 1997);

$$x_{n+1} = x_n - \frac{f(x_n)}{f'(x_n)} \tag{0.5}$$

The initial value of $x_0$ for i-th root of $P_n(x)$ can be calculated in equation (0.6).

$$x_0 = \cos\left(\pi \frac{i-\frac{1}{4}}{n+\frac{1}{2}}\right) \tag{0.6}$$

After finding $x_0$, all values of $x_i$ can be found. Suitable weights can be calculated by using equation (0.7).

$$w_i = \frac{2}{(1-x_i^2)[P'_n(x_i)]^2} \tag{0.7}$$

After we get all nodes and weights by using equations (0.2) to (0.7), the integral of $f(x)$ can be approximated in equation (0.8).

$$\int_a^b f(x)dx \approx \frac{(b-a)}{2}\sum_{i=1}^{n} w_i f\left(\frac{b-a}{2}x_i + \frac{a+b}{2}\right) \tag{0.8}$$

### C. Geometrical Theory of Diffraction

GO depends on some assumptions which are mentioned in Section 2.2 and does not take the account that objects in the medium may include edge, corner or vertex which are the main factors of diffraction. However, this assumption usually does not occur in the real world. Many shapes in the real world has discontinuity points result from the edges, corners or vertices in their geometries, and these discontinuity points cause the diffraction of the incident ray. Diffraction cannot be calculated by using classical techniques of GO. When comparing with classical GO, the only difficulty in the calculation of diffraction is obtaining of the initial field values on each diffracted ray. To determine the initial value of the field on a diffracted ray, firstly the incident field must be known. After that, the incident field is multiplied by a suitable diffraction coefficient which is obtained by the solving of the canonical problem of the related field. The canonical problem is a simple local problem and it includes only the immediate neighborhood of the diffraction point. Geometrical and physical properties of the local area around the diffraction point and the wavelength are used to obtain the solution of the canonical problem. Differently from the discontinuity points, another type of the diffraction is the diffraction that occurs at the caustic or focus of the ordinary or the diffracted rays. This type of the diffraction results from the intersection of the neighboring rays. Intersection of the neighboring rays causes that the cross-sectional area of a tube of rays becomes zero; and thus, the amplitude of the field cannot be calculated correctly at these points. To determine the amplitude of the field at these points correctly, the field on a ray which are passing through a caustic must be multiplied by a caustic correction factor. Caustic correction factor can be obtained by the solution of the canonical problems.

Since the solution of the canonical problems are not the same in the different local areas, diffraction coefficients are varied for edges, corners and vertices. Keller developed the Geometrical Theory of Diffraction in order to calculate the diffraction coefficients of various problems (Keller, February 1962). He modelled various diffraction mechanisms to defeat the some restrictions of GO. The first modelled diffraction mechanism is edge-diffracted rays. Edge-diffracted rays includes two different diffraction cases. The first case of it is that the incident wave propagates in a direction which is normal to the edge. In this scenario, the diffracted rays are cylindrical and the diffraction point is the center of this cylinder. This case is illustrated in Figure 0.2.

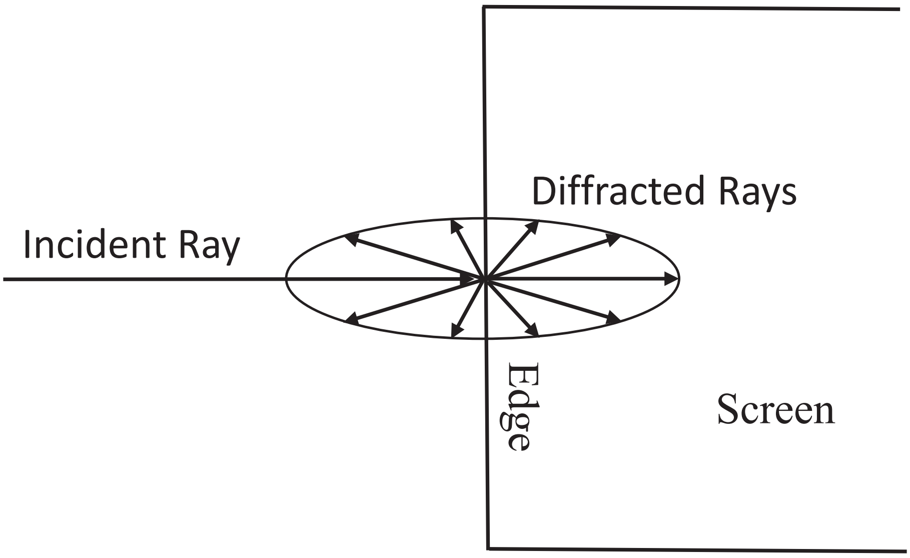

Figure 0.2. Cylindrical Diffracted Rays

In Figure 0.2, let $\bar{u}_e$ becomes the field on a diffracted ray from the edge and $\bar{u}_i$ becomes the incident field to the edge. The incident field $\bar{u}_i$ can be expressed in equation (0.9).

$$\bar{u}_i = A_i e^{j\psi_i} \tag{0.9}$$

In equation (0.9), $A_i$ represents the amplitude of the incident field and $\psi_i$ represents the phase of the incident field.

Let, the wavelength is denoted by $\lambda$ and the distance from the edge is denoted by $r$. In this case, the wavenumber $k$ equals to $2\pi/\lambda$. Since the diffracted rays are cylindrical in the first case of edge-diffracted rays and the flux through this cylinder ($rA_r^2$) must be constant, the cross-sectional are of the unit cylinder is proportional to $r$. Thus, the amplitude of diffracted ray $A_r$ is proportional to $r^{-1/2}$. If the diffraction coefficient is denoted by $D$, $\bar{u}_d$ can be expressed in equation (0.10).

$$\bar{u}_d = D\bar{u}_i r^{-1/2} e^{jkr} \tag{0.10}$$

Sommerfeld express the diffraction coefficient value in equation (0.10) as in equation (0.11) (Sommerfeld, 1954).

$$D = -\frac{e^{j\pi/4}}{2(2\pi k)^{1/2}\sin\beta}\left[\sec\frac{1}{2}(\theta-\alpha) \pm \csc\frac{1}{2}(\theta+\alpha)\right] \tag{0.11}$$

In equation (0.11), $\beta$ is the angle between the incident ray and the edge. This angle is equals to $\pi/2$ in this scenario because incident ray is in a direction normal to edge. $\alpha$ and $\theta$ are the angles between the incident and diffracted ray and the normal to edge respectively. They are illustrated in Figure 0.3. The upper sign in equation (0.11) is valid when boundary condition on the half-plane is $u = 0$ and the lower sign in equation (0.11) is valid when boundary condition on the half-plane is $\partial u/\partial n = 0$.

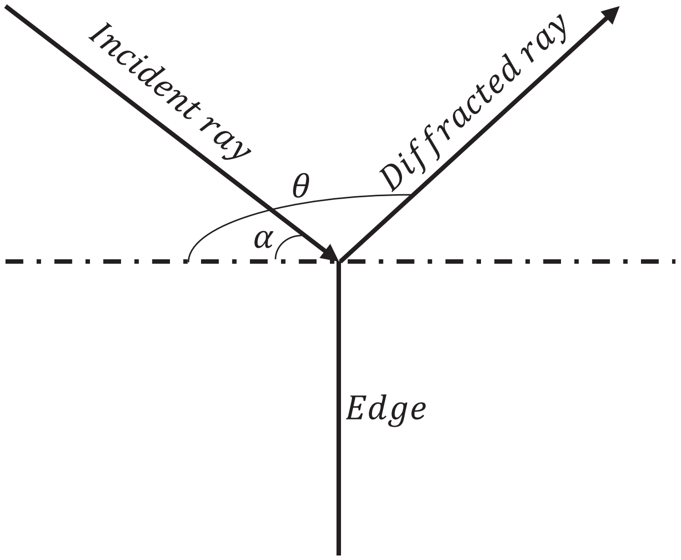

Figure 0.3. $\alpha$ and $\theta$ definitions

The second case of edge-diffracted rays is that incident wave propagates in a direction which is oblique to the edge. In this scenario, the diffracted rays are conical and the diffraction point is the top of this cone. This case is illustrated in Figure 0.4.

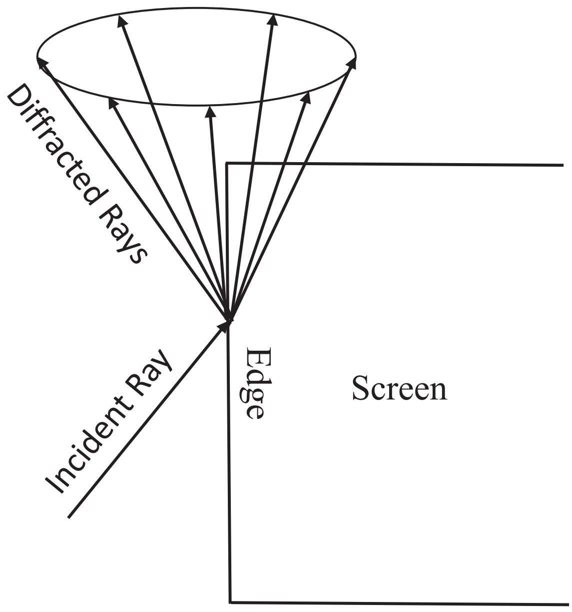

Figure 0.4. Conical Diffracted Rays

Equations from (0.9) to (0.11) are valid for the second case of edge-diffracted rays. The only distinctness of this case is that $\beta$ does not equal to $\pi/2$. It can take any value according to obliquity of the incident ray.

The second modelled diffraction mechanism is the fields diffracted by curved edges. The diffracted rays from a curved edge are illustrated in Figure 0.5.

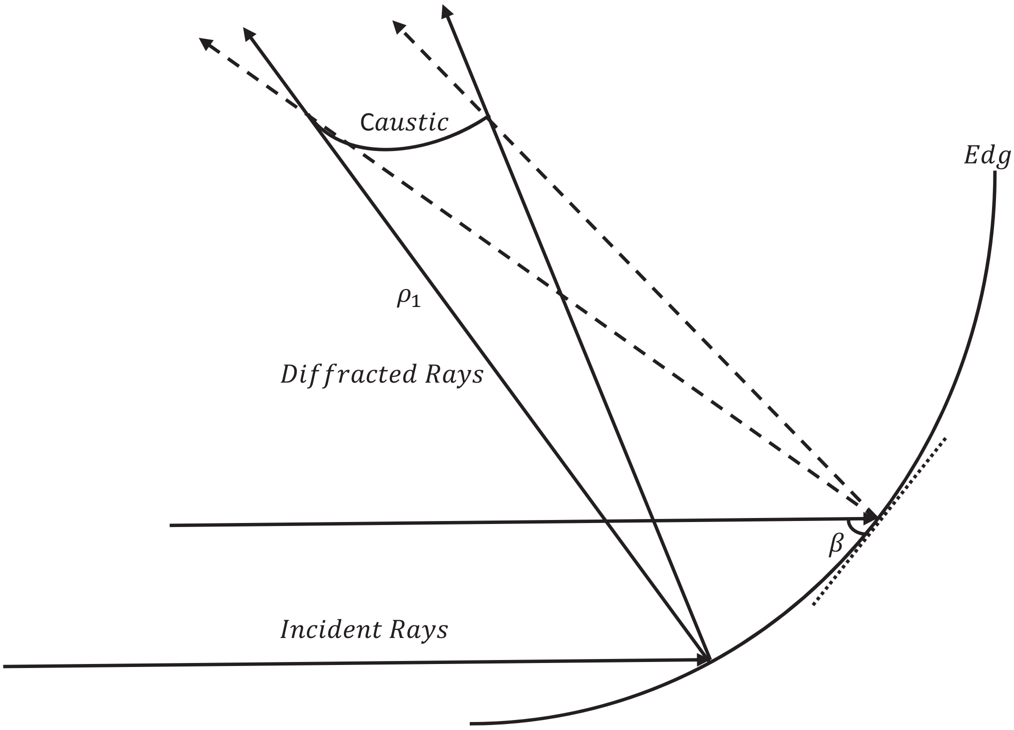

Figure 0.5. Diffracted Rays from Curved Edge

In Figure 0.5, $\rho_1$ represents the distance from the edge to caustic and $\beta$ represents the angle between the incident ray and the tangent to the edge. To obtain the cross-sectional area of a tube of rays, let $\rho_1$ and $\rho_2$ denote the radii of curvature of the wave front. At a distance $r$ further along tube, $(\rho_1 + r)$ and $(\rho_2 + r)$ are the corresponding radii. Thus, the cross-sectional area of a tube of rays is proportional to $(\rho_1 + r)(\rho_2 + r)A_r$. This proportion must be constant since the flux in the cross-sectional area must be constant. So, $A_r$ must be proportional to $\left((\rho_1 + r)(\rho_2 + r)\right)^{-\frac{1}{2}}$.

The diffracted rays form a caustic at the edge in Figure 0.5; thus, $\rho_2$ becomes zero. In this case, $A_r$ is proportional to $\left((1 + p_1^{-1}r)r\right)^{-\frac{1}{2}}$. The expression of $\bar{u}_d$ can be written in equation (0.12).

$$\bar{u}_d = D\bar{u}_i\left((1 + p_1^{-1}r)r\right)^{-\frac{1}{2}}e^{jkr} \tag{0.12}$$

The expressions of diffraction coefficient and incident field in equation (0.9) and (0.10) are also valid for the diffraction coefficient and incident field in equation (0.12).

The third modelled diffraction mechanism, which is the last diffraction mechanism mentioned in this thesis, is corner or tip diffraction. The incident wave which hits a corner of an edge of a boundary surface or a tip of a conical boundary surface causes the infinitely many diffracted rays. In homogeneous medium, these diffracted rays are straight lines and the wave fronts of them are spheres whose center is the corner or the tip. Since the wave fronts are spheres, the cross sectional are of a tube of rays is proportional to radius of the sphere. Thus, the amplitude of diffracted field is proportional to the root of the radius of the sphere. Thus, the diffracted field in this type of diffraction mechanism is given in equation (0.13).

$$\bar{u}_d = C\bar{u}_i r^{-\frac{1}{2}} e^{jkr} \tag{0.13}$$

In equation (0.13), $r$ is the distance of the diffracted-ray to diffraction point, $\bar{u}_i$ is the incident field and $C$ is the appropriate corner or tip diffraction coefficient. $C$ depends on the local geometry of diffraction point, the directions of incident and diffracted rays and the local properties of the media. Since $C$ is proportional to a length, it is proportional to $k^{-1}$.

After calculation of the initial fields on each diffracted ray, the amplitude and phase of total field must be found. The amplitude of total field at a point is determined by the addition of the fields on each ray passing through this point and the phase of total field at a point is obtained from the optical length of the ray whose starting point a reference point and whose endpoint is this point. More detailed information about diffraction can be found in (Balanis, Advanced Enginering Electromagnetics, 1989).

## D. Calculations

As discussed in chapter 3, incident field can be used in equation (3.1) directly for the front-fed parabolic reflectors. Thus;

$$\bar{f_m} = -\bar{f_i} + 2\hat{n}_m(\hat{n}_m \cdot \bar{f_i}) \tag{0.14}$$

Let, $K(\psi, \chi)$ be defined as the scalar in equation (0.15). The definitions of ψ and χ present in Figure 3.1.

$$K(\psi, \chi) = (\hat{n}_m \cdot \bar{f_i}) \tag{0.15}$$

The $x$,$y$ and $z$ components of $\bar{f_m}$ must be equal to values in equation (0.16) in order to get a $y$-polarized uniform field over the aperture plane.

$$\begin{gathered} \bar{f_m} = f_{mx}\hat{x} + f_{my}\hat{y} + f_{mz}\hat{z} \\ f_{mx} = 2K(\psi, \chi)n_{mx} - f_{ix} = 0 \\ f_{my} = 2K(\psi, \chi)n_{my} - f_{iy} = \frac{R}{e^{-jkR}} \\ f_{mz} = 2K(\psi, \chi)n_{mz} - f_{iz} = 0 \end{gathered} \tag{0.16}$$

Solving equation (0.16) for the components of $\bar{f_i}$ yields;

$$\begin{gathered} f_{ix} = 2K(\psi, \chi)n_{mx} \\ f_{iy} = 2K(\psi, \chi)n_{my} - \frac{R}{e^{-jkR}} \\ f_{iz} = 2K(\psi, \chi)n_{mz} \end{gathered} \tag{0.17}$$

where $n_{mx}$, $n_{my}$ and $n_{mz}$ are the $x$,$y$ and $z$ components of $\hat{n}_m$. Their values in terms of ψ and χ are given in equation (0.18).

$$\begin{gathered} n_{mx} = -\cos(\chi)\sin(\psi/2) \\ n_{my} = -\sin(\chi)\sin(\psi/2) \\ n_{mz} = \cos(\psi/2) \end{gathered} \tag{0.18}$$

Inserting equation (0.18) into equation (0.17);

$$\begin{gathered} f_{ix} = -2K(\psi, \chi)\cos(\chi)\sin(\psi/2) \\ f_{iy} = -2K(\psi, \chi)\sin(\chi)\sin(\psi/2) - \frac{R}{e^{-jkR}} \\ f_{iz} = 2K(\psi, \chi)\cos(\psi/2) \end{gathered} \tag{0.19}$$

Using equations from (0.15) to (0.19);

$$\begin{aligned} K(\psi,\chi) &= f_{ix}n_{mx} + f_{iy}n_{my} + f_{iz}n_{mz} \\ K(\psi,\chi) &= -f_{ix}\cos(\chi)\sin(\psi/2) - f_{iy}\sin(\chi)\sin(\psi/2) \\ &\quad + f_{iz}\cos(\psi/2) \end{aligned} \tag{0.20}$$

Rewriting equation (0.19);

$$\begin{aligned} f_{ix} &= \big[2f_{ix}\cos(\chi)\sin(\psi/2) + 2f_{iy}\sin(\chi)\sin(\psi/2) \\ &\quad - 2f_{iz}\cos(\psi/2)\big]\cos(\chi)\sin(\psi/2) \\ f_{iy} &= \big[2f_{ix}\cos(\chi)\sin(\psi/2) + 2f_{iy}\sin(\chi)\sin(\psi/2) \\ &\quad - 2f_{iz}\cos(\psi/2)\big]\sin(\chi)\sin(\psi/2) - \frac{R}{e^{-jkR}} \\ f_{iz} &= \big[-2f_{ix}\cos(\chi)\sin(\psi/2) - 2f_{iy}\sin(\chi)\sin(\psi/2) \\ &\quad + 2f_{iz}\cos(\psi/2)\big]\cos(\psi/2) \end{aligned} \tag{0.21}$$

An expanded form of equation (0.21);

$$\begin{aligned} f_{ix} &= \big[2f_{ix}\cos^2(\chi)\sin^2(\psi/2) + 2f_{iy}\sin(\chi)\cos(\chi)\sin^2(\psi/2) \\ &\quad - 2f_{iz}\cos(\chi)\sin(\psi/2)\cos(\psi/2)\big] \\ f_{iy} &= \big[2f_{ix}\sin(\chi)\cos(\chi)\sin^2(\psi/2) + 2f_{iy}\sin^2(\chi)\sin^2(\psi/2) \\ &\quad - 2f_{iz}\sin(\chi)\sin(\psi/2)\cos(\psi/2)\big] - \frac{R}{e^{-jkR}} \\ f_{iz} &= \big[-2f_{ix}\cos(\chi)\sin(\psi/2)\cos(\psi/2) \\ &\quad - 2f_{iy}\sin(\chi)\sin(\psi/2)\cos(\psi/2) + 2f_{iz}\cos^2(\psi/2)\big] \end{aligned} \tag{0.22}$$

Simplifying (0.22);

$$\begin{aligned} 0 &= f_{ix}[2\cos^2(\chi)\sin^2(\psi/2) - 1] \\ &\quad + f_{iy}[2\sin(\chi)\cos(\chi)\sin^2(\psi/2)] \\ &\quad + f_{iz}[-2\cos(\chi)\sin(\psi/2)\cos(\psi/2)] \\ \frac{R}{e^{-jkR}} &= f_{ix}[2\sin(\chi)\cos(\chi)\sin^2(\psi/2)] \\ &\quad + f_{iy}[2\sin^2(\chi)\sin^2(\psi/2) - 1] \\ &\quad + f_{iz}[-2\sin(\chi)\sin(\psi/2)\cos(\psi/2)] \\ 0 &= f_{ix}[-2\cos(\chi)\sin(\psi/2)\cos(\psi/2)] \\ &\quad + f_{iy}[-2\sin(\chi)\sin(\psi/2)\cos(\psi/2)] \\ &\quad + f_{iz}[2\cos^2(\psi/2) - 1] \end{aligned} \tag{0.23}$$

The matrix form of (0.23);

$$\begin{bmatrix} m_{11} & m_{12} & m_{13} \\ m_{21} & m_{22} & m_{23} \\ m_{31} & m_{32} & m_{33} \end{bmatrix} \begin{bmatrix} f_{ix} \\ f_{iy} \\ f_{iz} \end{bmatrix} = \begin{bmatrix} 0 \\ \dfrac{R}{e^{-jkR}} \\ 0 \end{bmatrix} \tag{0.24}$$

The elements of matrix **M** defined in equation (0.24) can be listed as:

$$\begin{gathered} m_{11} = 2\cos^2(\chi)\sin^2(\psi/2) - 1 \\ m_{12} = 2\sin(\chi)\cos(\chi)\sin^2(\psi/2) \\ m_{13} = -2\cos(\chi)\sin(\psi/2)\cos(\psi/2) \\ m_{21} = 2\sin(\chi)\cos(\chi)\sin^2(\psi/2) \\ m_{22} = 2\sin^2(\chi)\sin^2(\psi/2) - 1 \\ m_{23} = -2\sin(\chi)\sin(\psi/2)\cos(\psi/2) \\ m_{31} = -2\cos(\chi)\sin(\psi/2)\cos(\psi/2) \\ m_{32} = -2\sin(\chi)\sin(\psi/2)\cos(\psi/2) \\ m_{33} = 2\cos^2(\psi/2) - 1 \end{gathered} \tag{0.25}$$

By taking inverse of **M**, the components of incident field required for uniform aperture field can be expressed as:

$$\begin{bmatrix} f_{ix} \\ f_{iy} \\ f_{iz} \end{bmatrix} = \begin{bmatrix} -\dfrac{R}{e^{-jkR}}\sin(2\chi)\dfrac{\cos(\psi) - 1}{2} \\ -\dfrac{R}{e^{-jkR}}\left((\cos(\psi) - 1)\sin^2(\chi) + 1\right) \\ -\dfrac{R}{e^{-jkR}}2\sin(\chi)\sin(\psi/2)\cos(\psi/2) \end{bmatrix} \tag{0.26}$$

## E. Reflection from Surface

Consider the surface in Figure 0.6.

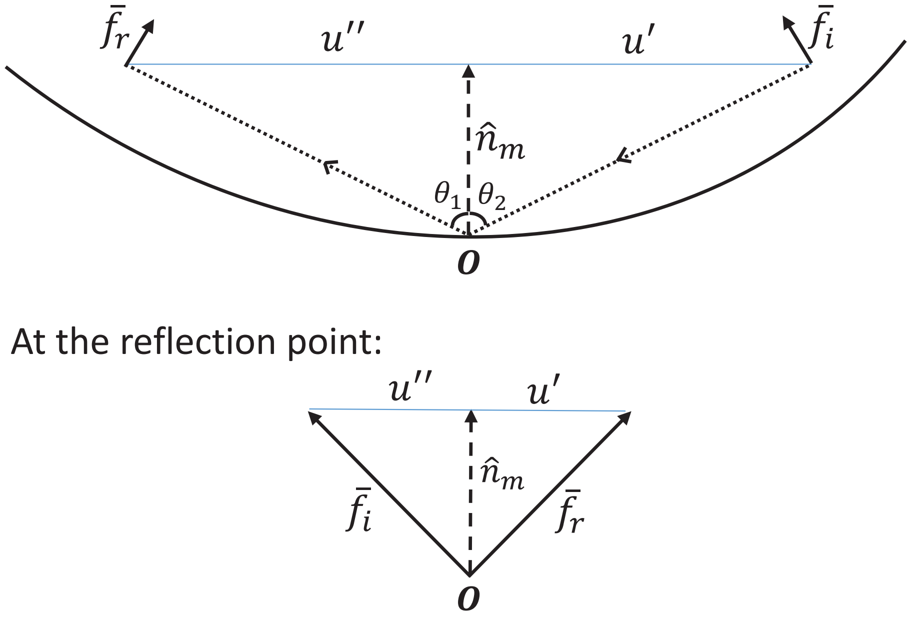

Figure 0.6. Reflection from Surface

In Figure 0.6, $\bar{f}_i$ and $\bar{f}_r$ represent the incident and reflected fields, respectively. From the law of reflection, $\theta_1 = \theta_2$. By using the vectors in Figure 0.6:

$$\bar{f}_r \cdot \hat{n}_m = \bar{f}_i \cdot \hat{n}_m \tag{0.27}$$

The symmetry in the figure provides equation (0.28).

$$u' = -u'' \tag{0.28}$$

By using the vectors in Figure 0.6 again:

$$\begin{aligned} u' &= \bar{f}_r - \hat{n}_m = \bar{f}_r - (\bar{f}_r \cdot \hat{n}_m)\,\hat{n}_m \\ u'' &= \bar{f}_i - \hat{n}_m = \bar{f}_i - (\bar{f}_i \cdot \hat{n}_m)\,\hat{n}_m \end{aligned} \tag{0.29}$$

By utilizing from equation (0.28) and equation (0.29):

$$\bar{f}_r - \left(\bar{f}_r \cdot \hat{n}_m\right)\hat{n}_m = -(\bar{f}_i - (\bar{f}_i \cdot \hat{n}_m)\,\hat{n}_m) \tag{0.30}$$

By equation (0.27):

$$\begin{aligned}
&\bar{f}_r - \left(\bar{f}_i \cdot \hat{n}_m\right)\hat{n}_m = -(\bar{f}_i - (\bar{f}_i \cdot \hat{n}_m)\,\hat{n}_m) \\
&\bar{f}_r = \left(\bar{f}_i \cdot \hat{n}_m\right)\hat{n}_m - \bar{f}_i + \left(\bar{f}_i \cdot \hat{n}_m\right)\hat{n}_m \\
&\bar{f}_r = -\bar{f}_i + 2\hat{n}_m\left(\bar{f}_i \cdot \hat{n}_m\right)
\end{aligned} \tag{0.31}$$